Chapter 1

Introduction

In the last decades, nanotechnology and nano-science have attracted lots of attention due to their unique physical properties and promising device applications. As the size of device is shrunk down to the nanometer scale, the quantum effects[1,2] start to play an important role in the behaviors of nanostructures. For example, the density of states of quantum wells (QWs), quantum wires (QWrs), and quantum dots (QDs) are significantly different from that of the normal size bulk materials[3], cf. Fig.1.1. Especially, for QWrs, the spike-like 1-D density of states can be utilized to enhance device performances in the laser application[4,5,6], such as the lower threshold current, temperature insensitive operation, and larger modulation bandwidth. Therefore, different material QWrs are fabricated and studied experimentally in this work to investigate their physical properties and the laser application.

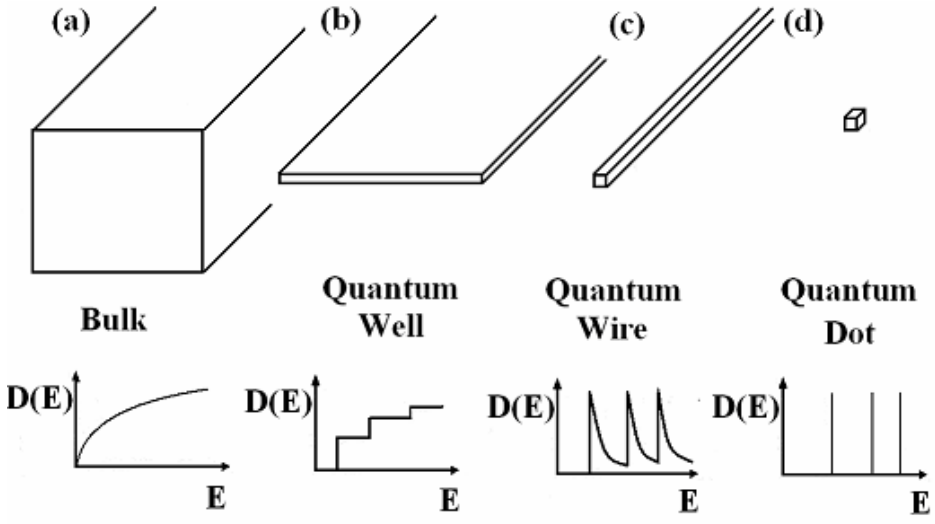

Fig.1.1: The density of states:(a) Bulk. (b)Quantum well. (c)Quantum wire. (d)Quantum dot.

The nanostructure fabrication methods can be divided into two categories: the top-down approach and the bottom-up approach. The top-down approach uses lithography and etching techniques to define and fabricate nanostructures, while the bottom-up approach utilizes atom-by-atom or molecule-by-molecule self-assembled methods to form nanostructures. In semiconductor technology, both these two techniques are used to fabricate nano-scale structures and devices. The molecular beam epitaxy (MBE) technique[7,8] and the metal organic chemical vapor deposition (MOCVD) technique[9,10] have been successfully and widely used to produce high quality semiconductor devices with directly epitaxying thin epilayers or abrupt heterojunctions. Using these approaches, QWs and 2-dimensional electron gas (2DEG) channel have been routinely grown for applications in semiconductor laser diodes[11], light emitting diodes (LED)[12], infrared photo detectors [13], and high electron mobility transistors(HEMT) [14]. These materials also provide a platform for fundamental scientific researches.

Because QWs can be easily fabricated by directly epitaxying thin films or abrupt heterojunctions, while the fabrication of 1-dimensional (1-D) and 0-dimensional (0-D) quantum structures usually needs more techniques. 1-D and 0-D quantum structures are much harder to be fabricated, compared with QWs. To obtain these quantum structures, many methods were investigated and studied. For semiconductor QWr structures, several approaches were reported: direct process of QWs into QWrs[15,16], V-groove growth[17,18], ridge-type growth[19,20], fractional layer superlattice growth[21,22], strain induced composition modulation by short period superlattices[23,24], step bunch[25,26], growth on cleaved-edge surface[27,28], corrugated high-index substrates[29,30], and the self-assembled method[31,32,33]. Direct process of QWs into QWrs, V-groove growth, ridge-type growth, and growth on the cleaved-edge surface are belonged to the top-down approach. These methods need the lithography, the etching technique, or the re-growth process to fabricate the

QWrs. However, the lithography and etching processes in the top-down approach induce the defects, which will form unwanted carrier traps or scattering centers, and deteriorate the device performance.

Among several solutions to avoid these defects caused by the top-down approach, the self-assembled growth method, one of the bottom-up approaches, stands out and has became more attractive in fabricating semiconductor nanostructures and nano-devices. Advantage of self-assembled growth method is that the 0-D and 1-D quantum structures can be easily fabricated only by directly epitaxying a thin lattice mismatched film. The self-assembled growth mode utilizes lattice mismatched film deposition with 3 different types[34], Frank-van der Merwe(FM) mode, Volmer-Weber (VW) mode, and Stranski-Krastannow (SK) mode shown in Fig.1.2(a), (b) and (c) respectively. The lattice mismatched film deposition accumulates strain energy. In order to release some strain energy, the nucleation of self-assembled structures is happened. The nucleation process is controlled by minimizing the total free energy, including substrate-film interface energy and film surface energy. The deposition film will minimize the total free energy. If the deposition film has less surface energy, it will spread across the substrate and form 2-dimensional (2-D) growth. This is called FM mode, cf. Fig.1.2(a). If the deposition film has strong surface energy, it will immediately form 3-dimensional (3-D) island growth to minimize the total free energy. This is VW growth mode shown in Fig.1.2(b). For the case of intermediate film surface energy, the growth mode is called SK mode, shown in Fig.1.3(c). This growth mode will change to 3-D growth after several monolayer deposition. The surface energy of the deposition film during MBE growth is influenced by the As beam flux, the substrate temperature, the substrate orientation, the beam flux of each group III source, the V/III ratio, As_2 or AS_4 source, etc.

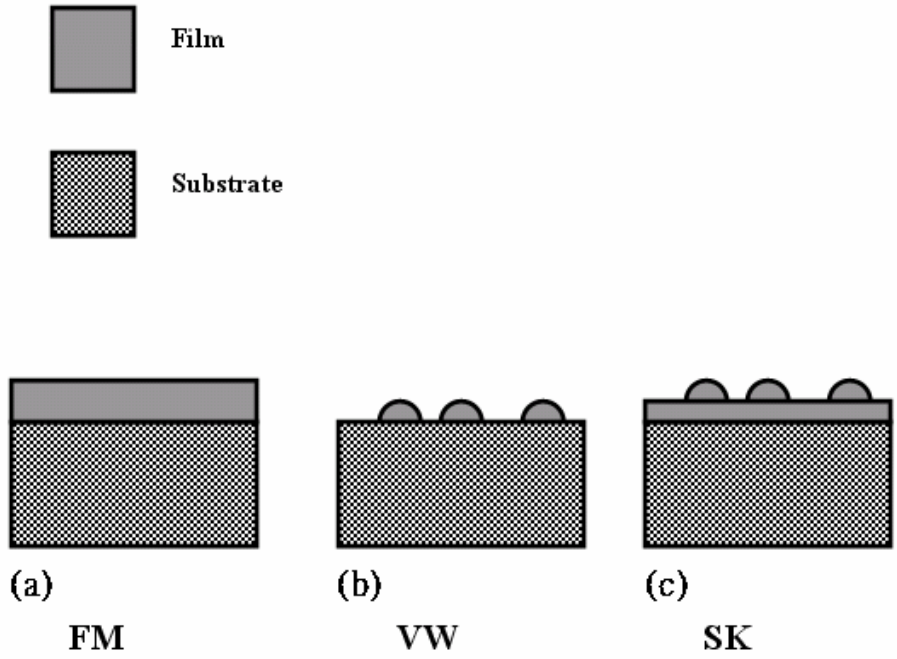

Fig.1.2: The sketches of lattice-mismatched growth modes.
(a) Frank-van der Merwe mode. (b)Volmer-Weber mode.
(c)Stranski-Krastannow mode.

VW mode is not the favorite quantum structure deposition method, because it often causes a rough and non uniform surface. At the same time, SK mode can provide a lattice matched wetting layer and more uniform nano structures. Consequently, SK mode is usually the preferable method for studying the heterostructure self-assembled quantum structures.

Based on the SK mode growth principle, there was a breakthrough in semiconductor research in the 1990s [35]: self-assembled In(Ga)As QDs were successfully grown on GaAs using MBE and MOCVD techniques. Recently, self-assembled InAs quantum structures on InP substrates have also been reported. Moreover, self-assembled GaAs nano wires in InGaAs matrix on InP substrates was also observed[36].

People found that the closely stacked of these self-assembled quantum structures have very interesting ordering behaviors. Closed stacked In(Ga)As QD system in GaAs shows

vertical alignment characteristic[37,38]. Later, the anticorrelated submolayer CdZnSe QD behavior in ZnSe[39], and the face-center-cubic (fcc) anti-correlation structure of PbSe QDs in PbEuTe[40] were also observed. Lately, some stacked and ordered behaviors of InAs QWrs on InP substrates were also reported. However, the origin of InAs QWrs in InAlAs stacking behavior is still not clear.

Based on the extensively studying of self-assembled In(Ga)As QDs on GaAs substrates, the In(Ga)As QDs in GaAs have been utilized for 1.3μm laser diodes successfully[41]. It is useful for the optical network application. Furthermore, the InAs QDs in GaAs are also successfully utilized for QD infrared photodetectors(QDIP) [42,43]. As a result, the application of self-assembled InAs QWrs on the materials latticed matched to InP substrates attracted people's attention in recent years. The InAs quantum structures in InAlGaAs materials lattice matched to InP offer the possibility for longer wavelength (1.5~2.1μm) operation, which provides the applications in medical care, gas spectroscopy, laser radar through atmospheric transmission windows, and optical communications through low-loss fluoride fibers[44]. These self-assembled InAs nanostructures on InP substrates have been investigated for laser application[45,46]. The 1550nm lasing wavelength for optical communication was demonstrated by self-assembled InAs QWrs in InGaAlAs matrix on InP substrates[47]. The wide gain bandwidth of self-assembled InAs QWrs on InP substrates attracted people for the semiconductor optical amplifier purpose. In 2002, utilizing InAs QWrs on InP substrates for the 1550 nm optical amplifiers was also demonstrated [48]. For the photodetector application, using self-assembled InAs nanostructures in InAlAs matrix lattice matched to InP substrates to fabricate the infrared photo detectors was reported[49]. Furthermore, the report of photodetection beyond 10μm for infrared photodetectors with InAs nano structure grown on InGaAlAs lattice matched to InP substrates was given in this year[50].

In the presence of these quantum structures, the carriers transport properties are certainly be affected. For QDs, like artificial atoms, may act as scattering centers or traps[51,52,53]. Carriers transport behaviors in the QWrs were investigated theoretically and experimentally [54,55,56]. The structure with InAs QWrs embedded in InP bulk was also reported an asymmetric electrical transport behavior by Walther, etc[57]. In addition to the QD and QWr structures, the anti-QDs and anti-QWrs also have fun physics behaviors. People used the lithography method to form anti-QDs[58,59] and ani-QWrs[60,61]. In these systems, some interesting physical phenomena were observed. However, these systems were obtained by lithography method and defects were introduced. Recently, Dr. S.D.Lin successfully obtained self-assembled GaAs anti-QWrs in InGaAs matrix on InP substrates. In that report, the sample, which had a 2-D electron conduction channel with GaAs anti-QWrs embedded near the InGaAs/InAlAs heterostructure, was observed significant asymmetric transport behavior in low temperature.

This thesis focuses on the growth and the application of InAs and GaAs self-assembled wire-like quantum structures in InGaAs matrix and InAlAs matrix, lattice matched to InP substrates, by the solid source MBE technique. In order to obtain well enough wire-like structures, we used the atomic force microscope(AFM) to study the influence of MBE growth parameters on nanostructure morphology. After obtaining the suitable growth window for growing well-enough wires, we investigated the physical behaviors and the application potential of these nano wires. The cross-sectional transmission electron microscope (TEM) technique was used to study the stacking behaviors and the composition modulation behaviors caused by the self-assembled InAs QWrs and GaAs anti-QWrs embedded in InGaAs matrix and InAlAs matrix on InP substrates. Polarization dependence photoluminescence(PPL) technique was implemented to study the QWr photoemission polarization behaviors. We also tried to use InAs QWrs to fabricate laser diodes and investigated their behaviors. Moreover,

anisotropic mobility property for InGaAs/InAlAs heterostructures with InAs QWrs neighboring on the 2-D channel was studied.

The quantum structures were all grown on 2” normally (100) oriented InP substrates in our experiments. The wafer orientation can be identified from the identifying flats on the wafers. The wafers, used in our experiments, have two types of identifying flat definition, one is EJ and another is US, see Fig.1.3(a). These flats are employed as reference for checking the nano structure orientation. We found that nano structures in the InGaAs matrix and InAlAs matrix, lattice matched to InP, all preferred to elongate along $[1\,\bar{1}\,0]$ direction. In this thesis, some cross-sectional TEM pictures were needed to investigate the nano structure behaviors. The orientations of these pictures and of the nanostructure in these pictures were identified by one cubic crystal lattice characteristic. For the cubic crystal lattice, such as simple cubic(s.c.), face-centered cubic(f.c.c), and body-center cubic(b.c.c.), directions and planes having the same indices are perpendicular to one another, i.e. (h,k,l)⊥[h,k,l], see Fig.1.3(b). GaAs and InP crystals are Zinc Blende structures, also regarded as an f.c.c. lattice with two atoms per lattice site. As a result, the orientation of these cross-sectional pictures and the nanostructures in these pictures can be identified.

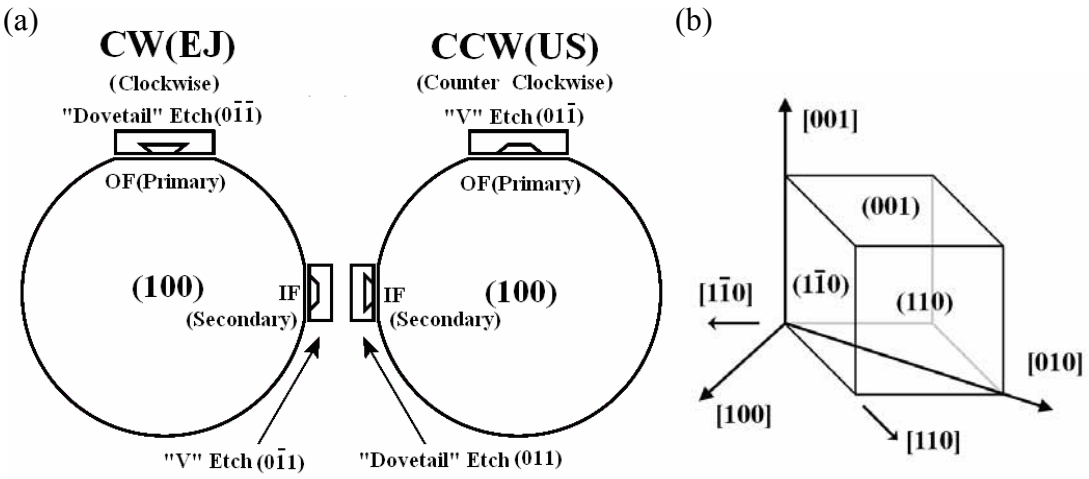

Fig.1.3: (a)Two types of the identifying flats on the 2” (100) InP wafers. (b) the diagram shows that (h,k,l)⊥[h,k,l] for the cubic crystal system.

Finally, some definitions of certain terminologies about the InAs/GaAs quantum structures are needed to clarify here. Because the bandgap of InAs is lower than those of InGaAs and InAlAs, lattice matched to InP substrates, the long and straight wire-like InAs quantum structures in InGaAs or InAlAs matrix are called “quantum wires (QWrs).” However, under improper growth conditions, the self-assembled InAs structures do not form well enough wire-like structures. They are just short, wriggled, and wide dash-like. In these conditions, these structures are just called “InAs quantum structures.” For GaAs in InGaAs matrix lattice matched to InP substrates, the GaAs has larger bandgap than InGaAs matrix has. Therefore, the straight and long self-assembled GaAs wire-like quantum structures are called “anti-QWrs” in this thesis. Similarly to the InAs case, self-assembled GaAs nano structures with unsuitable growth parameters are just like short dashes. Sometimes, their shapes are even more like elliptic dots. In these conditions, these self-assembled GaAs nano structures are just called “GaAs quantum structures”.

Chapter 2

Experimental Techniques

2.1 Introduction

The experimental techniques used in this thesis are described in this chapter. It is divided into four parts: molecular beam epitaxy(MBE), material characteristic analysis, device processes, and device measurements. All the samples studied in this work were grown with the solid source MBE system in our laboratory. After growing the devices, the properties of epitaxied wafers were characterized with the high resolution X-ray diffractometer (HRXRD), the atomic force microscope (AFM), the photoluminescence (PL) system, the Hall measurement, and the transmission electron microscope (TEM). In additions, wet etching, metallization, and package were used for device processes. Then, the devices were analyzed with the current-voltage (I-V) measurement, the light-current (L-I) measurement, and the lasing spectrum analyzer.

2.2 Molecular Beam Epitaxy

2.2.1 Introduction to Our MBE System

The MBE system in our laboratory is VARIAN GEN II solid source MBE system. It consists of two growth integral units linked by an extension chamber. Fig.2.1 shows a sketch of one integral growth unit. Each integral part can be divided into three main components: the

vacuum system, the epitaxy system, and the analysis system.

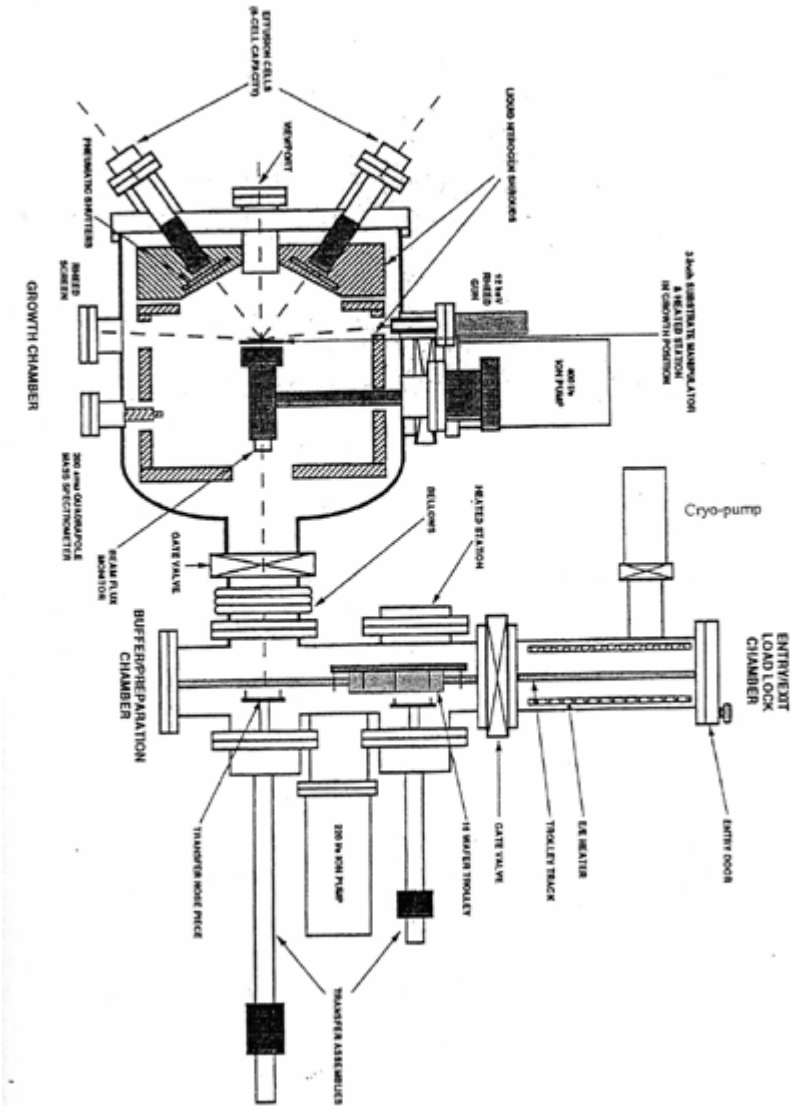

Fig.2.1: The sketch of Veeco Varian GEN II solid source MBE system

- **Vacuum System**

The MBE system consists of two growth chambers, two buffer chambers, one extension chamber, two entry/exit chambers, and one phosphorous recovery chamber. There is a gate valve between each chamber for the connection or the isolation. These chambers and gate valves construct two main growth integral units, which connect with each other by the

extension chamber.

As pump down the whole MBE system from the atmosphere pressure, in order to avoid organic contamination, the oil-free roughing pump system is needed[62]. Our MBE system has two roughing pump systems. The roughing pump system is composed of one turbo-molecular pump, one absorption pump, and one scroll pump (or a diaphragm pump). Each growth integral unit has one roughing pump system, which has parallel connections to each chamber through the pipes and isolates from each chamber by the all metal angle valves.

In order to maintain the UHV environment and the clearness condition for high quality epitaxy, oil-free pumps are also needed for MBE system. Each growth chamber is equipped with one cryo-pump, one ion pump, and one titanium sublimation pump (TSP). Each buffer chamber is installed with one ion pump and one TSP. For the entry/exit chamber, it is installed with a cryo-pump. As regards the phosphorous recovery chamber, it is equipped with a turbo-molecular pump. The cryo-shroud, additionally, is installed in the growth chamber. When growing the samples, the cryo-shroud will be cooled down by pouring the liquid nitrogen (LN_2), from the phase separator, to help to capture the unwanted impurities.

- **Epitaxy System**

The effusion cell is used to heat the source material to offer the molecular beam for epitaxy. The sources used in our laboratory can be classified into three categories: group III sources, group V sources, and doping sources. Furthermore, in our laboratory, there are three kinds of group III sources: aluminum (Al), gallium (Ga), and indium (In). Two types of the effusion cells are adopted for group III sources: the conventional Knudsen cells (K cells) and the SUMO cells. The SUMO cell is superior to the K cell, because it offers fewer defects, more uniform epitaxy, smaller source depletion effect, less shutter-related transient source

flux variation, and larger source capacity than the K cell. For group V sources, phosphorus (P), arsenic (As), and antimony (Sb) in the cracker cells are utilized in our laboratory. Except to the cracker cells, the conventional K cell is also used only for the As source. In addition to the sources mentioned above for obtaining III-V semiconductor, doping sources are also required for more ingenious applications. Silicon (Si) and beryllium (Be) are provided for n-type and p-type doping sources respectively in our laboratory, and K cells are used for these two doping sources.

The effusion cells are installed in the source ports on the growth chamber. One growth chamber has eight ports. The cells mounted on these ports are charged As, Al, Ga, In, Si, and Be sources. Another growth chamber has ten ports to install the effusion cells. The sources in this growth chamber contains P, As, Sb, Al, Ga, In, Si, and Be sources.

The beam flux of the cracker cell is controlled by a needle valve. For the K cells and the SUMO cells, their beam fluxes are controller by the cell temperature. PID control technique is used to control the effusion cell temperature. The precision of temperature control of each effusion cell is needed to be under 0.1℃ for obtaining a stable molecular beam flux. There is a shutter in front of the orifice of each effusion cell for cutting off or liberating the molecular beam. The pneumatic valve is used to control the switch of each shutter. Both of the switch on and the switch off time for all shutters are within 0.1sec in order to obtain the abrupt molecular beam flux.

The substrate is mounted on a substrate holder in the growth chamber for epitaxy. As growing samples, all the effusion cells will be heated to the required temperatures. The substrate holder will face to the effusion cells, and then be heated to the designated temperature. In order to increase the epitaxy uniformity, the substrate holder is spun.

- **Analysis System**

In order to monitor the growth chamber condition and the epitaxy situation, there are four analysis tools equipped in each growth chamber: the reflection high-energy electron diffraction (RHEED) assembly, the residue gas analyzer (RGA), the pyrometer, and the beam flux ion gauge. The RHEED is the most important tool to monitor the growth condition in situ. A high energy electron beam with a small incident glancing angle to the sample surface is diffracted by the sample surface. The surface structures and the deposited adatom kinetics can be analyzed from the diffracted RHEED patterns. RHEED is usually use to monitor the thermal desorption of the native oxide layer on the substrate, and to obtain the growth rate of each group III cell in MBE. Moreover, the RHEED pattern also provides a useful way to monitor the QD and the QWr formation. RGA is a mass spectrometer. It is used to monitor the residue gas for vacuum diagnostic in the MBE chamber. As set the RGA to monitor the helium, it will be a very sensitive tool for virtual leak identification in MBE.

The pyrometer is a non-contact, infrared radiation thermometer designed to monitor the wafer surface temperature. Through the heated view port, the infrared radiation (0.91 - 0.97μm) from the wafer surface irradiates on the infrared sensor, mounted on the pyrometer. By setting an appropriate emissivity value of each kind of wafers, the wafer surface temperature will be obtained.

The beam flux ion gauge is an ion gauge designed for monitoring the beam flux from each cell. From measuring the beam-on and beam-off pressure, the beam flux of each cell can be obtained. The relative fluxes can be calculated from the relative beam equivalent pressures (BEP) according to

$$\frac{J_x}{J_y} = \frac{P_x}{P_y} \times \frac{\eta_y}{\eta_x} \times \left(\frac{T_x M_y}{T_y M_x} \right)^{1/2} \quad \text{.....(Eq.2.1)}$$

where J_x is the beam flux of source X, P_x is its BEP, T_x is its effusion cell absolute temperature, and M_x is its molecular weight. η_x is its ionization efficiency relative to nitrogen and is given by

$$\frac{\eta}{\eta_{nitrogen}} = \left[(0.4Z/14)+0.6\right] \quad \text{……(Eq.2.2)}$$

where Z is the atomic number[62].

2.2.2 Principle of MBE Growth

After source flux elements are deposited on the sample surface, the MBE growth procedure is begun with these excess mobile adatoms on the surface. Fig.2.2 shows the schematic explanation. Firstly, the absorbed molecular source dissociated on the surface, then, these absorbed constituent atoms will migrate on the surface randomly. The random migration adatoms may meet another adatom to nucleate an "island", or they may stick on the steps or vacancies. Finally, the incorporation of the constituent atoms will contribute the crystalline growth. However, some adatoms on the sample surface may obtain enough thermal energy to escape from the surface, and cannot incorporate into the crystal lattice[63].

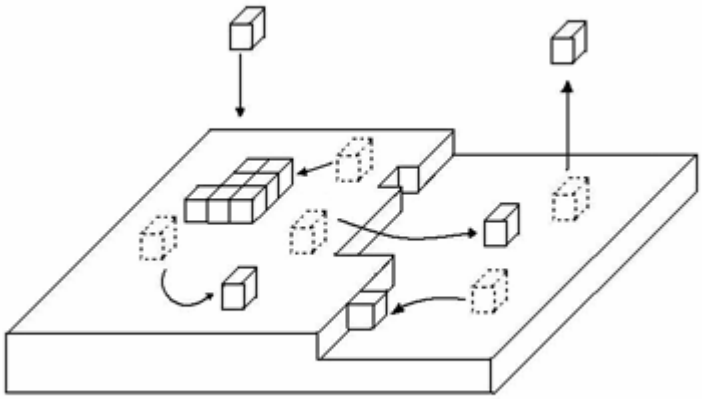

Fig.2.2: The atomic mechanism of the crystal deposition

2.2.3 Growth Rate and Doping Concentration Check

RHEED oscillation provides us a simple and direct way to observe the epitaxy behavior. As shown in Fig.2.3, for a clean epi-ready wafer, the surface is smooth, and the diffracted RHEED pattern is bright. As adatoms adhere on the wafer surface, the brightness of RHEED pattern is becoming weaker. The RHEED pattern will be weakest when half layer is deposited. Then, it will become brighter and brighter till whole one layer is deposited. As a result, the RHEED pattern brightness will oscillate during the layer by layer deposition[64,65]. Using this technique, we are able to check the growth rate of each group III cell as follows.

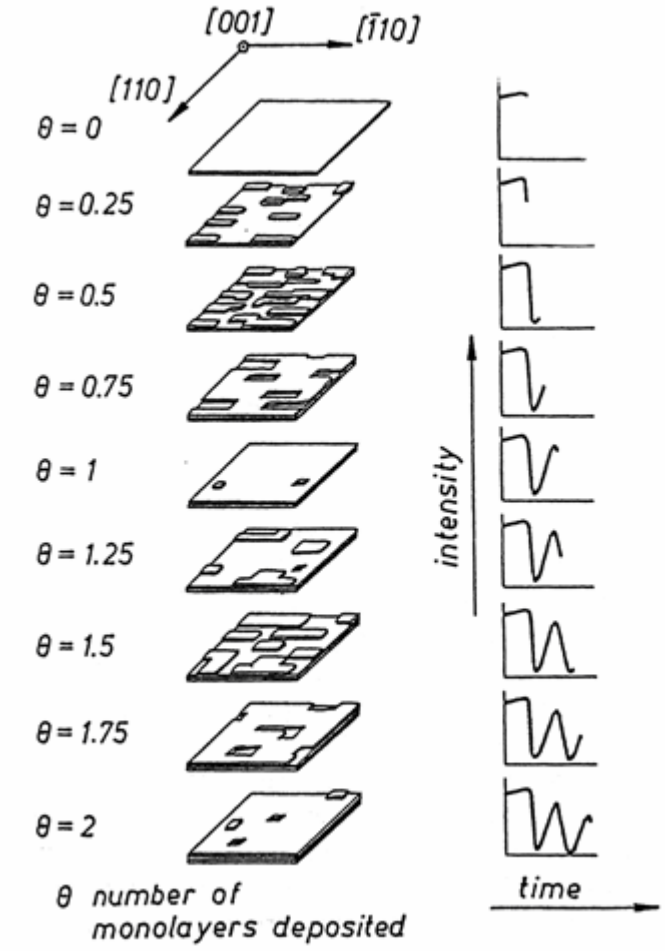

Fig.2.3: The formation of the RHEED oscillation. (Ref.65)

A well-designed cell gives a stable beam flux under a certain temperature. Before deposition, we use the beam flux ion gauge to record the BEP of each group III cell under different temperature. When the deposition of a group III cell is begun, the RHEED pattern oscillation is monitored and recorded by a Video RHEED system. Using the Video RHEED system, the RHEED oscillation is analyzed by the fast Fourier transform method to obtain the growth rate of this cell at a fixed temperature. Fig.2.4 shows the RHEED oscillation of a Ga K cell. Then, the cell temperature is changed to another designated temperature and the previous procedure is repeated. Finally, the growth rate under different BEP of each cell is obtained.

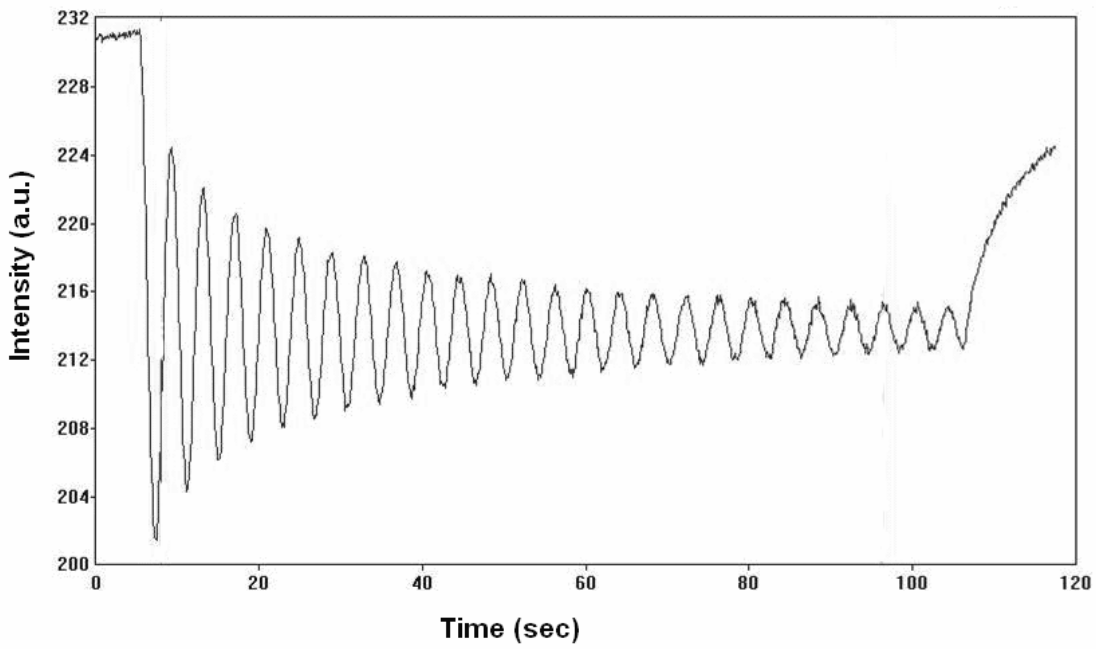

Fig.2.4: The RHEED oscillation obtained by a Ga cell

Because GaAs and AlAs are almost lattice matched to GaAs substrates, , the normally (100) oriented GaAs substrates are used to check the growth rate of Ga and Al sources. For the In cell, because of large lattice mismatch, about 7%, between GaAs and InAs, the normally (100) oriented InAs substrates are needed for In source growth rate check.

After the growth rate calibration is finished, GaAs epitaxy under 1μm/hr growth rate is carried out to calibrate the n-type and the p-type doping cells with the etching C-V measurement or Hall measurement. Because the beam flux ion gauge is unable to detect out the BEP of doping cells, we assume that the evaporation amount of atoms of doping cells under a fixed temperature will not vary between each run.

2.2.4 Growth Rate Calibration for InP

InP, GaAs, and InAs crystals have different lattice constant. Because we only calibrated the GaAs/AlAs growth rate on GaAs substrates and the InAs growth rate on InAs substrates directly from the RHEED oscillation, the InGaAs/InAlAs growth rate on InP substrates is needed to be modified for eliminating the factor of the different lattice constant. The growth rate for a given source flux on the GaAs substrates should be modified on the InP substrates as

$$R_{InP} = R_{GaAs} \times \left(\frac{a_{InP}}{a_{GaAs}} \right)^2 \quad \text{……(Eq.2.3)}$$

where R is the growth rate (ML/s), and a is the lattice constant. The modification equation of the growth rate on the InAs substrates to the growth rate on the InP substrates is similar. As a result, the mix of the flux with the growth rate, R_{GaAs}, on the GaAs substrates and the flux with the growth rate, R_{InAs}, on the InAs substrates will give the growth rate, R_{InP}, on the InP substrates as:

$$R_{InP} = R_{GaAs} \times \left(\frac{a_{InP}}{a_{GaAs}} \right)^2 + R_{InAs} \times \left(\frac{a_{InP}}{a_{InAs}} \right)^2 \quad \text{…….(Eq.2.4)}$$

and the III group element composition ratio is

$$R_{GaAs} \times \left(\frac{a_{InP}}{a_{GaAs}} \right)^2 : R_{InAs} \times \left(\frac{a_{InP}}{a_{InAs}} \right)^2 \quad \text{……(Eq.2.5)}$$

By Eq.2.5, we are convenient to find out the required In, Al, and Ga beam fluxes for growing $In_{0.53}Ga_{0.47}AsAs$ and $In_{0.52}Al_{0.48}As$ matrix on InP substrates.

2.2.5 Wafer Epitaxy

For obtaining high epitaxy quality, the cleanliness requirement of the growth chamber is extremely important. In order to enhance the growth chamber cleanliness and to avoid the contamination, before the wafer epitaxy, there are several procedures needed to do: wafer bake, growth chamber cooling down, oxide layer desorption, and so on.

The epi-ready wafer is mounted on a Mo block substrate holder with In or on an In-free spring substrate holder. Then the substrate holders will be put into the entry/exit chamber. The entry/exit chamber will be baked up to 200℃ for removing water. When the pressure of the entry/exit chamber is down to less than 1E-8torr, the substrate holders will be transferred to the buffer chamber. Each wafer is needed to be baked to 400℃ for GaAs wafers and 300℃ for InP wafers in the buffer chamber in order to remove the organic contamination and the residue water on the wafers. As the pressure in the buffer chamber is lower than 3E-9torr, the wafer is ready to be transferred into the growth chamber for growth.

Before we start the growth procedure, the growth chamber is needed to cool down by pouring liquid nitrogen into the cryoshroud before warming up all source cells. The cryoshroud, surrounding the source cells and the manipulator, has extra low temperature for absorbing the impurities in the growth chamber and the source elements that do not adhere on the wafer. Furthermore, it prevents unwanted elements absorbing on the wafer during epitaxy. After finishing cryoshroud cooling down procedure for a while, all source cells will be

warned up to required temperature for epitaxy. When starting epitaxy, the thin native oxide on the wafer surface is needed to remove first. The GaAs wafer is heated up to 620℃ and the InP wafer is heated up to 520℃ under sufficient As flux to obtain a no-contamination wafer surface. Then the wafer temperature will be varied to the required value for growing a buffer layer to recover the wafer surface. Finally, the structure epitaxy is started.

2.3 Material Characteristic Analysis

2.3.1 X-ray Diffractometer

X-ray diffraction is a non-destructive method to investigate the crystal structure information, such as lattice constant, layer composition, strain, film thickness, etc. X-ray has wavelength comparable to the lattice constant in the crystal. Thus, X-ray scattered by the atoms in the crystal will be diffracted. As the diffraction condition is under the Bragg condition, the diffraction pattern will be very intensive [66] because the Bragg condition is

$$n\lambda = 2d_{hkl}\sin\theta_B \quad \text{……(Eq.2.6)}$$

where λ is the wavelength of X-ray, n is an arbitrary integer, θ_B is the diffraction Bragg angle, and d_{hkl} is the spacing of the adjacent parallel planes of atoms with Miller indices h, k, l. The relation between d_{hkl} and the lattice constant, a, is

$$d_{hkl} = \frac{a}{\sqrt{h^2 + k^2 + l^2}} \quad \text{……(Eq.2.7)}$$

Here the $\omega - 2\theta$ rocking curve method is used to determine whether the InGaAs/InAlAs matrix is lattice matched to InP substrates or not. The rocking curve is to scan the diffraction beam intensity as a function of the diffraction angle of the sample with a fixed incident X-ray

beam. Fig.2.5 shows the sketch picture of the high resolution X-ray diffractometer (HRXRD) system. In order to obtain high angular resolution for determining the lattice constant, two silicon crystals, channel-cut crystals (CCC), are positioned in front of the X-ray source to obtain a monochromated X-ray beam with only 12" divergence[67]. Moreover, a dual channel analyzer (DCA) crystal is placed in front of the detector, for a finer angular resolution of the scattering angle, 2θ.

As examining the InGaAs or the InAlAs lattice constant, we scan the scattering angle in the neighborhood of InP (4,0,0) diffraction beam with an angular range less than 500arcsec. If the angle difference between InGaAs/InAlAs diffraction beam and InP diffraction beam is within 100arcsec, we assume InGaAs/InAlAs is lattice matched to InP substrates. Fig.2.6 shows the HRXRD rocking curve results of the InGaAs matrix and InAlAs matrix grown on the InP substrates by our MBE system.

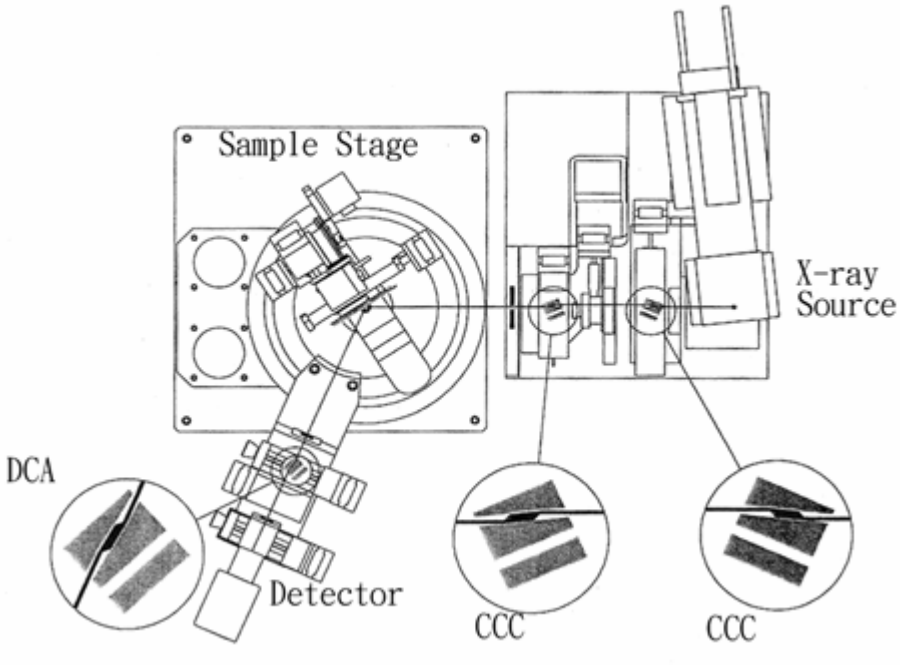

Fig.2.5: The schematic picture of the HRXRD. (Ref.67)

(a)

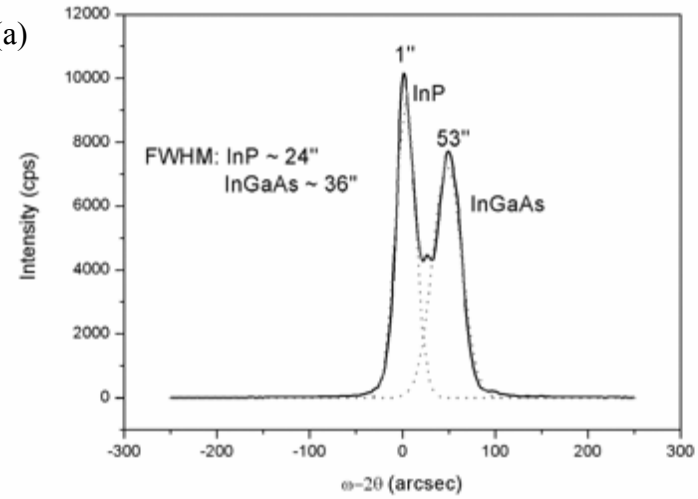

(b)

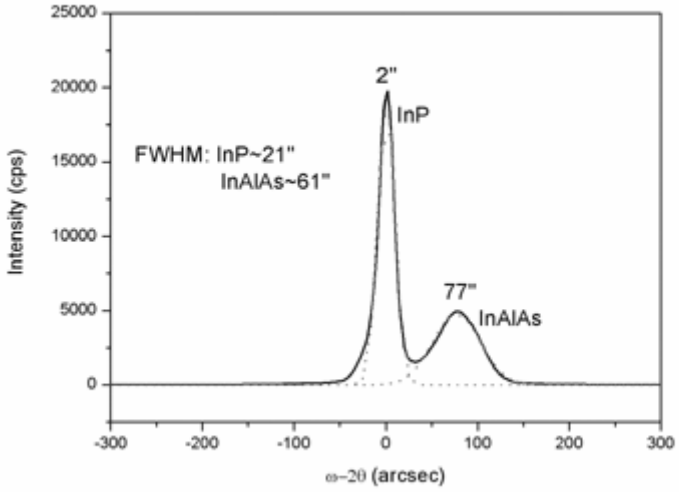

Fig.2.6: The HRXRD spectrum results for lattice matched to InP check (a)InGaAs (b)InAlAs

2.3.2 Atomic Force Microscope

In order to study the nanometer scale surface, the atomic force microscope (AFM) technique with tapping mode is used here. Basically, the AFM system consists of the optical head and the scanner[68]. The sample is mounted on the scanner, which controls the X, Y, and Z movement of the sample. The optical head consists of a laser diode, a four-quadrant positional photodetector, and a cantilever with a tip. The cantilever is vibrated under its resonant frequency by a bimorph. The optical head monitors the vibration situation of the cantilever. As the tip on the cantilever is approaching the sample, due to the force between the

sample surface and the tip, the phase of the vibration will be changed. According to the phase change, the system can image the morphology of the sample surface. Fig.2.7 shows the operation principle of the AFM technique. For QWr samples, to avoid the auto image compensation caused by the software, the scan direction should be perpendicular the wire structures.

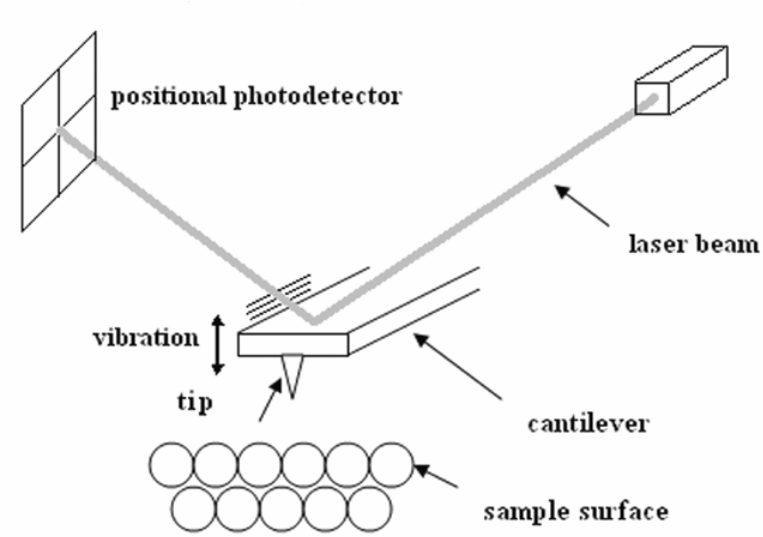

Fig.2.7: A diagram of the AFM operation principle

2.3.3 Photoluminescence

Photoluminescence (PL) is a useful non-destructive optical technique for inspecting semiconductor materials[69]. It can observe some characteristics of semiconductor materials, such as impurities, defects, bandgap, etc. The PL signal comes from the optical radiation due to the recombination of the electron/hole pair. People use a light source to pump the electrons form the valence band to the conduction band. After thermalization of the carriers in the bands, photo emission occurs from the electron/hole pair recombination.

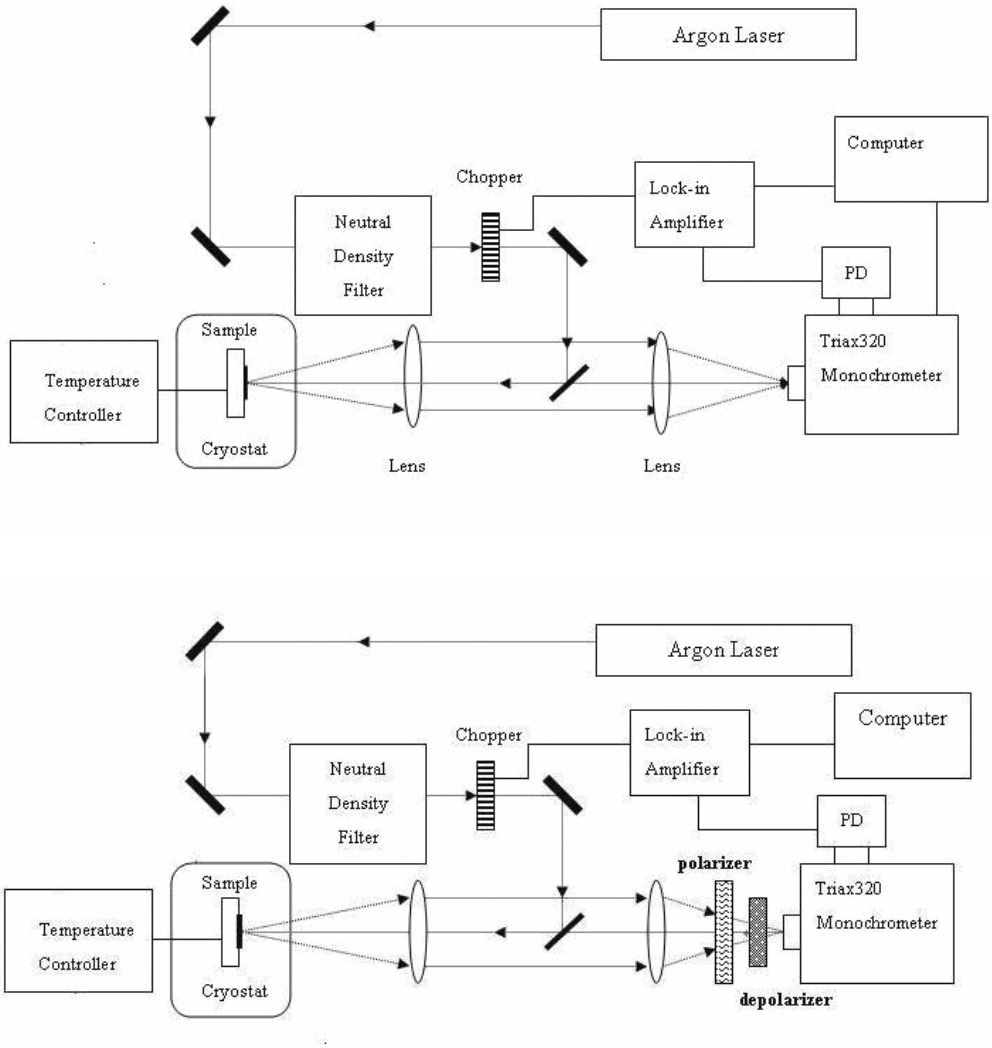

Fig.2.8: (a)The scheme of the PL measurement system. (b) The scheme of the PPL measurement system, modified from the PL system.

In our laboratory, we use an argon-ion high power CW laser to illuminate samples, sketched in Fig.2.8(a). The mode locking technique is used to obtain high signal/noise ratio results. The laser beam passes through the chopper, which chops the laser beam and gives the modulated signal to the locking amplifier, and then, is focused on the sample. The sample is mounted on a vacuumed cryostat holder. The temperature of the cryostat can be controlled from 10K to room temperature. Then the light emission from the sample is collected by lens

and focused into the input slit of the monochromator. There are three gratings in the monochromator for different spectrum demands. The detector can choose the TE cooled Si, InGaAs, InGaAsSb, or InAs solid state detector. The monochromator operation and signal collection are controlled by a computer.

The PL from QWrs has interesting characteristics. It has obvious polarization dependence behavior. In order to study the polarization dependence PL (PPL), a polarizer is needed to be posited in front of the monochromator input slit. A depolarizer is also needed to place between the polarizer and the input slit to eliminate the strong polarization dependence responsibility of the monochromator[70]. Fig.2.8(b) sketches out the modification of our PL system for PPL measurement. By rotating the polarizer, we are able to study the PPL results of the QWr samples.

2.3.4 Transmission Electron Microscope

The transmission electron microscope (TEM) technique uses the electro-optic lenses to deflect and focus the incident electron beam on the research sample, and then, generates a direct transmitted electron beam and diffract electron beams[71]. Finally, with the object electro-optic lenses, these electron beams can be transformed as the image mode (real space) or the diffraction mode (reciprocal space). If much more diffracted electron beam are collected to obtain the multiple image mode, the interference of those diffracted electron beams gives the lattice image, called the high resolution image or called the lattice image mode. This technique is called high resolution TEM (HRTEM). HRTEM images can provide lattice images, such as the interface images, the unit cell structures, the dislocations, etc. The TEM pictures usually reveal the stress field images. In order eliminate the stress images, choosing appropriate crystal orientation of the sample and select the composition sensitive

diffracted electron beams, qualitative analysis of composition distribution will be obtained[72].

2.4 Device Processes

After finishing the wafer epitaxy, wafers are processed by photo-lithography to define patterns. For the sake of easy lift-off process later, negative photo-resist is preferred. Here, AZ-5214E with an image reversal procedure provides the negative photo-resist purpose. After photo-resist spin coating, soft bake, exposure with sample orientation alignment, post-exposure bake, reversal bake, whole sample exposure, development in AZ-300, rinsing in de-ionised (D.I.) water, and dry by pure nitrogen purge, the patterns are obtained. Wet etch is used here for mesa etch and specific layer removing, Solution of H_2SO_4:H_2O_2:H_2O (1:8:80) is used to etch InAlGaAs on InP.

The E-gun system is used to form metal contacts in the device process. Before metal evaporation, the sample surface is needed cleaning for the better contacts. First, samples are mounted in the UV-ozone stripper at 100℃ for 2 min in order to remove the residual photo-resist. Then, samples are dipped in the HCl:H_2O (1:1) solution for 2~3sec in order to etch the native oxide clearly. After rinsing in the D.I. water, samples are mounted into the E-gun chamber immediately for preventing re-oxidation. As the E-gun chamber pressure is less than 2E-6torr, the metal evaporation is started. Here Ti/Pt/Au metals are used for the p-type InGaAs ohmic contact and the n-type InP ohmic contact. For the laser diode process, before the n-metal evaporation on the backside, the samples are thinned by physically polished to about 120~150μm thickness in order to be cleaved easily. After the metal evaporation, take out the samples and perform lift-off process with acetone. Finally, for

obtaining good ohmic contacts, rapid thermal annealing is performed. For the laser diode process, the laser wafers are needed to cleave to obtain the mirror facets. After cleaving the laser wafers, they are sent to Industrial Technology Research Institute for TO can package.

2.5 Device Measurements

2.5.1 Hall Measurement

There are two common sample geometries for Hall measurement: (1) square or circular Van der Pauw geometry and (2) long, narrow Hall bar geometry, cf. Fig.2.9. Although Van der Pauw method is the simpler approach to obtain the carrier concentration and Hall mobility, compared with the latter, it cannot be used to measure the carrier mobility along designated direction. Therefore, the 8-contact Hall bar method was adopted here to investigate the carrier transport behavior of our samples with InAs QWrs embedded. After measuring the longitudinal resistivity, ρ_{xx}, and the Hall resistivity, ρ_{xy}, the sheet carrier concentration, n_s, and electron Hall mobility, μ, would be obtained[73] by:

$$n_s = \frac{B}{q \times \rho_{xy}} \quad \text{……(Eq.2.8)}$$

$$\mu = \frac{1}{q \times n_s \times \rho_{xx}} = \frac{q \times \tau_m}{m} \quad \text{……(Eq.2.9)}$$

where B is the applied magnetic field, q is the carrier charge, m is the carrier effective mass, and τ_m is the momentum relaxation time of carriers.

In order to investigate the dependence of anisotropic electrical transport behavior on the InAs QWr orientation, two sets of 8-contack Hall bars, parallel to the QWrs and perpendicular to the QWrs, were fabricated for Hall measurement. The Hall measurement was carried out from 10K to 300K.

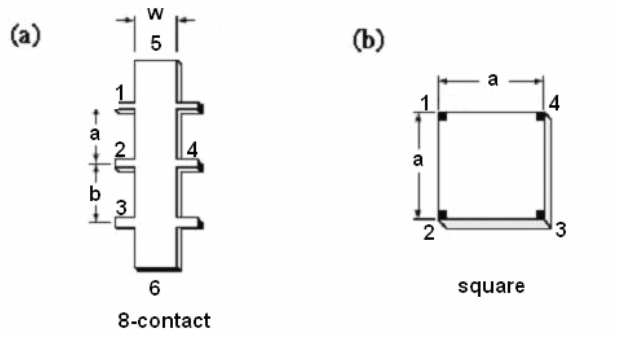

Fig.2.9: Two geometry types for Hall effect measurement: (a) long, narrow 8-contact Hall bar geometry. (b) Nearly square Van der Pauw geometry

2.5.2 Temperature Dependence for Laser Diode L-I Curve Measurement

For measuring the temperature dependence behavior of L-I curves, the system is constructed just like the sketch in Fig.2.10. The package laser diodes are mounted in the vacuumed cryostat. The cryostat temperature can be controlled from 10K to room temperature. The current source is HP-8114A. The current period is 20μs and the duty cycle is set as 5%. The detector used here is a Ge solid state detector under 3V reverse bias. An oscilloscope is used here to monitor the laser driven current, the photon current form the detector, and the trigger signal from the current source. All the signals are collected by a boxcar and then are transferred to a computer to be recorded and analyzed.

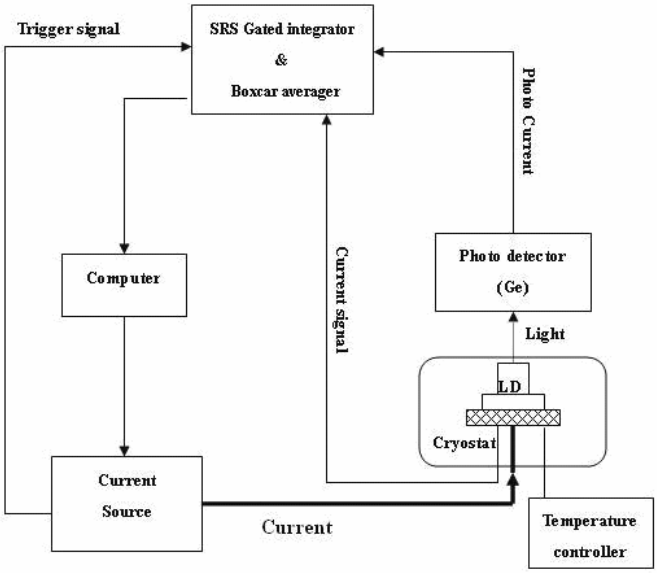

Fig.2.10: Temperature dependence for laser diode L-I curve measurement system

2.5.3 Temperature Dependence Lasing Spectrum Analyzer

On the purpose of investigating the QWr laser temperature dependence on the spectrum behaviors from 10K to room temperature, the vacuumed cryostat is needed. Fig.2.11 shows the system construction. The packaged laser diodes are mounted on the cryostat, and then are cooled down to the designated temperature. After injecting the current and lasing, the spectra are collected by Triax 320 monochromator with an InGaAsSb detector for analysis. Fig.2.12 shows the longitudinal mode spectrum result of the QWr laser diode, with 1mm cavity length, measured by this system. The mode spacing is about 4Å. By the equation,

$$\Delta\lambda = \frac{\lambda^2}{2n_r \times L} \quad \text{……(Eq.2.10)}$$

where L is the laser cavity length, n is the refractive index of the active region in the laser diode, and λ is the lasing wavelength. Substitute n_r =3.4 for InGaAs, L=1mm, and λ=1707nm, we obtain $\Delta\lambda \approx 4$ Å. It coincides with the measurement result.

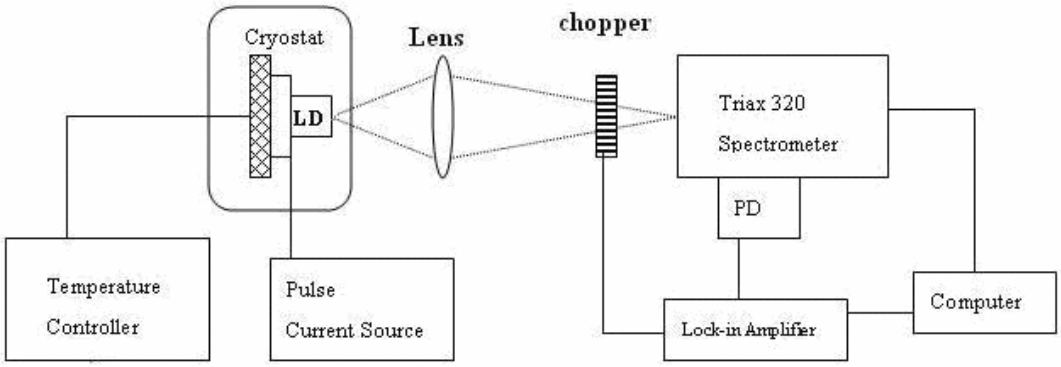

Fig.2.11: The Temperature Dependence Spectrum analyzer for laser diodes

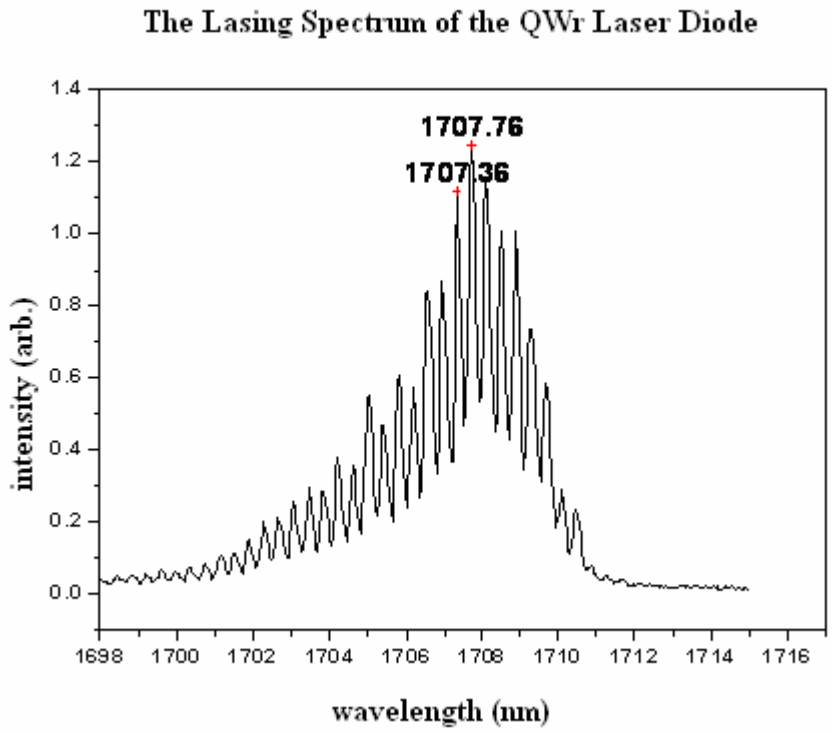

Fig.2.12: The longitudinal mode spectrum of a QWr laser diode measured by the spectrum analyzer in Fig.2.11

Chapter 3

InAs/GaAs Quantum Structure Growth in InGaAs Matrix on InP Substrates

3.1 Introduction

Recently, the self-assembled nano structures were attracted much attention because of their unique physical properties and potential device applications. Moreover, the self-assembled method avoids the nanostructures having additional defects, which are induced from the lithography and the regrowth processes. In the last decade, considerable efforts for self-assembled In(Ga)As QDs on GaAs substrate has been demonstrated[3] ,and have been successful applied to QD lasers[41] and QD infrared photodetectors[74,75]. Moreover, self-assembled InAs quantum structures grown on InP substrates were reported recently[32,76,77]. InAs quantum structure easily form wire-like structures elongated along $[1\bar{1}0]$ direction in InGaAs matrix, lattice matched to InP substrates. The wire formation should be due to the different adatom diffusion coefficient and the different step edge reactivities along $[110]$ and $[1\bar{1}0]$ directions[78,79]. The anisotropic stress relaxation may also play a decisive role for wire formation[80]. People found that the growth condition InAs wires on InP substrates is sensitive to the MBE growth parameters[77]. Recently, GaAs anti-QWrs in InGaAs matrix lattice matched to InP substrates has also been observed[36].

In this chapter, we study the growth condition of the self-assembled InAs and GaAs quantum structures in InGaAs matrix lattice matched to normally (100) oriented InP

substrates. The tapping mode AFM technique was used to investigate the influence of the MBE growth parameters on InAs and GaAs quantum structure morphology in InGaAs matrix. We found that the self-assembled quantum structures all elongate along $[1\bar{1}0]$ direction on InP substrates. In a suitable growth condition, several monolayers of InAs or GaAs can form the nano-scale wire-like structures. The investigation is divided into two parts: InAs quantum structures in InGaAs matrix on InP substrates, and GaAs quantum structures in InGaAs matrix on InP substrates.

Before providing the details, we would like to note that our MBE system has two growth units, and their code names are Rn and Lm. Because Rn unit is a new chamber and Lm unit is an old one, there is pyrometer reading difference between these two growth units. From the GaAs de-oxide temperature and the QD growth condition, the pyrometer reading should have about 15~20℃ difference between these two growth units. This means that if the pyrometer reading in Rn unit is 500℃, the same growth temperature in Lm unit is about 515~520℃. This temperature difference is needed to be cared in the following discussion.

3.2 InAs Quantum Structure Growth in InGaAs Matrix on InP Substrates

In this section, we investigated the influence of the MBE growth condition on the InAs quantum structure morphology from several parameters: the InAs monolayer number, the substrate temperature, the As_2 beam equivalent pressure (BEP), and the In deposition rate. All samples were grown on normally (100) oriented InP substrates. From these systematical experiments, the suitable growth condition for InAs QWrs is obtained. Table 3.1 is the list for

InAs quantum structure growth condition.

	Monolayer (ML)	Substrate Temperature (℃)	In source G.R. (μm/hr)	Interruption time between each ML (sec)	As2 BEP (torr)
Lm4009	2	525	0.625	10	1.5E-6
Lm4237	3	525	0.5	18	1.5E-6
Lm4249	4	525	0.5	18	1.5E-6
Lm4250	5	525	0.5	18	1.5E-6
Lm4264	6	525	0.5	18	1.5E-6
Lm4265	8	525	0.5	18	1.5E-6
Lm4283	4	515	0.5	19	1.5E-6
Lm4330	4	520	0.5	19	1.5E-6
Lm4547	4	510	0.41	19	1.5E-6
Rn0072	4	495	0.056	10	2.5E-6
Rn0073	4	495	0.55	No	2.5E-6
Rn0084	4	495	0.056	10	1.5E-6

Table 3.1: List of InAs quantum structure growth condition

3.2.1 InAs Monolayer Number

Fig.3.1 shows the AFM results of (a) 2ML(Lm4009), (b) 3ML(Lm4237), (c) 4ML(Lm4249), (d) 5ML(Lm4250), (e) 6ML(Lm4264), and (f) 8ML(Lm4265). These InAs nano structures were grown under about 525℃. The As_2 BEP was about 1.5E-6torr. The In deposition rate was roughly about 0.5μm/hr. Except Lm4009, which only had 10sec interruption between each InAs monolayer deposition, the others had 18sec interruption.

As shown in Fig.3.1(a), the 2ML InAs deposition forms irregular, thin, long cake-like structures elongated along $[1\bar{1}0]$ direction. Their thickness and the width varies from 1nm to

3nm and from 80~100nm respectively.

The AFM result in Fig.3.1(b) shows that the structures formed by 3ML InAs deposition are also similar to the structures shown in Fig.3.1(a). However, the thickness of these structures is more uniform, and is about 1~2nm. Structures in Fig.3.1(b) are also generally straighter, longer, and more regular than those in Fig.3.1(a).

The structures in Fig.3.1(c) are the result of 4ML InAs deposition. The structures are almost wire-like. The wires are about 1.5~2.5nm in thickness, 40~60nm in width and at most 0.75μm in length.

Fig.3.1(d) shows the results of 5ML InAs deposition. The structures are also wire-like, but with dot-like structures on some wires. The wire dimension is 1.5~3nm in thickness and 40~60nm in width. However, the dot-like structures on the wires have about 4.5~5.5nm in thickness.

Fig.3.1(e) is the AFM result of 6ML InAs deposition. The structures are also similar to those in Fig.3.1(d), but the thickness is larger, about 2~3nm. More dot-like structures are formed on each wire. The dimension of these dot-like structures is similar to that in Fig.3.1(d).

The picture in Fig.3.1(f) is the 8ML InAs deposition result. The wires are much thicker, about 3~5nm. The wire width in Fig.3.1(f) is about 40~60nm in width, similar to that in Fig.3.1 (c), (d), and (e), and the length is also about 0.75μm. However, larger dot like structures, with thickness above 10nm, are formed on the substrate.

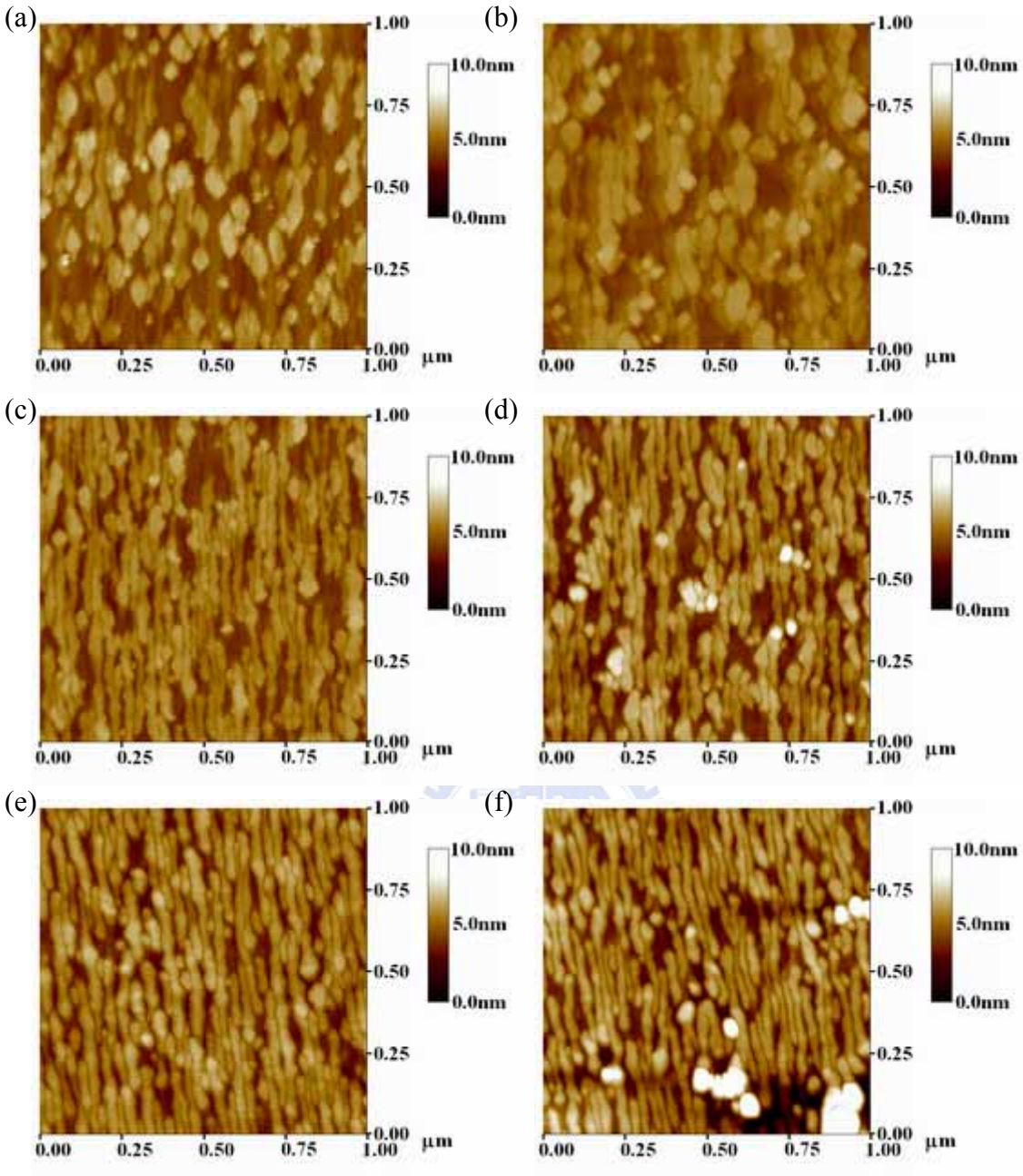

Fig.3.1: InAs quantum structure dependence on the InAs monolayer number:
(a) 2ML(Lm4009). (b) 3ML(Lm4237). (c) 4ML(Lm4249). (d)
5ML(Lm4250). (e) 6ML(Lm4264). (f) 8ML(Lm4265).

These sample discussed in this subsection all had interruption between each monolayer growth. Irregular, thin, long cake-like structures elongated along $[1\,\bar{1}\,0]$ direction are formed at 2ML deposition. Wire-like structures start to form about at 3ML InAs deposition. In order

to minimize the free energy in [110] direction, the structure width maintains at 40~60nm, even up to 8ML InAs deposition. The migration preference along [1 $\bar{1}$ 0] direction of In atoms makes the InAs quantum structures to be dash-like or wire-like structures. 2ML InAs, even 3ML InAs, does not supply sufficient In atoms to form long enough wires. Moreover, in these two cases, the stress along [110] direction is not large. Therefore, 2ML and 3ML cases have wider and shorter dash-like structures. However, the too large InAs monolayer number does not make the wires longer. This is because the In atoms just have finite migration free path. As a result, deposition with too many In atoms makes the In atoms nucleate at some regions on the wires to form the lumps.

3.2.2 Substrate Temperature

The pictures in Fig.3.2 show the AFM images for (a) 525℃(Lm4249), (b) 515℃(Lm4283), (c) 520℃(Lm4330), and (d) 510℃(Lm4547). All of them are the results of 4ML InAs deposition. The As_2 BEP was about 1.5E-6torr. The In deposition rate was about 0.5μm/hr. All samples had 18~19sec interruption between each InAs monolayer deposition.

In Fig.3.2(a), the structures formed under 525℃ are almost wire-like. However, the wires have some wriggles and lumps. The wires are about 1.5~2.5nm in thickness, 40~60nm in width, and at most 0.75μm in length .

Fig.3.2(b) presents the result of 515℃ growth temperature. The wires are smooth. The dimension is about 1.5~2nm by 40~70nm. The wire length can be found over 1μm.

The image in Fig.3.2(c) is the result grown under about 520℃. This result is very similar to (a). Each wire wriggles and has lumps.

The picture in Fig.3.2(d) is the result to grow InAs wires under 510℃ growth

temperature. It is similar to the result shown in Fig.3.2(b). However, the wires are smoother and straighter. Many wires have length above 1μm. The wire dimension is about 2.5~3nm by 40~70nm.

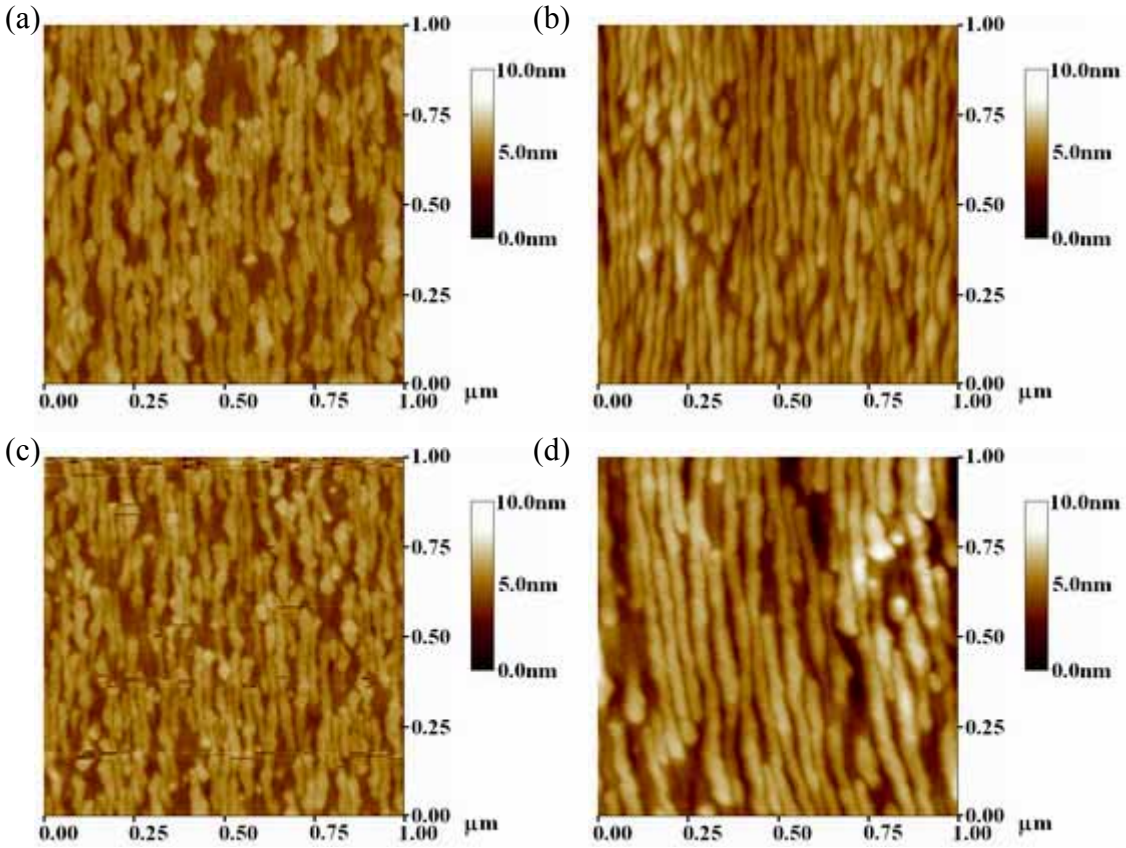

Fig.3.2: InAs quantum structure dependence on the substrate temperature: (a) 525°C(Lm4249). (b) 515°C(Lm4283). (c) 520°C(Lm4330). and (d) 510°C (Lm4547).

From the above four AFM results, we obtain that the 510°C substrate temperature is the most suitable temperature for the 4ML InAs wire-like structure formation in this study. It should be the In diffusion coefficient ratio of $[1\bar{1}0]$ direction to $[110]$ direction is larger at about 510°C, and the ratio is decreased with increasing temperature. As a result, the wires are the most smooth and longest at 510°C. At about 520~525°C, some lumps and wriggles are formed on these wires.

3.2.3 As_2 BEP

Fig.3.3 (a) and (b) show the AFM results for 2.5E-6torr (Rn0072) and 1.5E-6torr (Rn0084), respectively. They are all 4ML InAs nano structures. The In deposition rate was about 0.056μm/hr. Both samples had 10sec interruption between each InAs monolayer deposition.

It is obvious that the structures in Fig.3.3(b), with the lower As_2 BEP, have the longer and straighter wires. The wires shown in Fig.3.3(b) can be longer than 1μm while the wires shown in Fig.3.3(a) with the higher As_2 BEP wriggle and are shorter. This contrast between Fig.3.3 (a) and (b) is due to that the As atoms obstruct the In atoms to migrate on the surface.

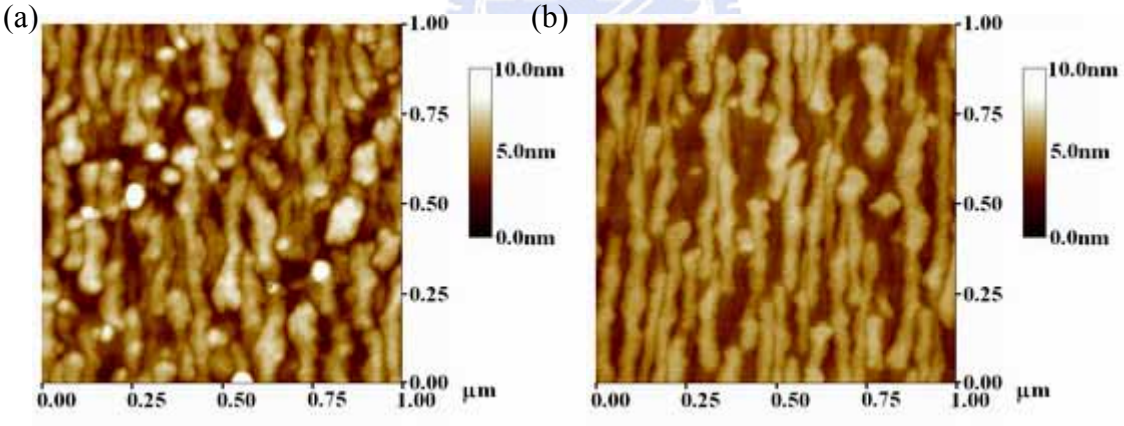

Fig.3.3: InAs quantum structure dependence on As_2 BEP: (a) 2.5E-6torr (Rn0072). (b) 1.5E-6torr (Rn0084).

3.2.4 In Growth Rate and Interruption Time

Fig.3.4 (a) and (b) show the AFM results for 0.056μm/hr with 10sec interruption (Rn0072) and 0.55μm/hr without interruption (Rn0073) respectively. All of them were 4ML InAs nano structures and were grown at 495℃ under the As BEP with about 2.5E-6torr.

Apparently, the picture in (a) shows longer and straighter structures than the picture in (b) shows. It is attributed to that In atoms in Rn0073 have not enough time to migrate along $[1\bar{1}0]$ direction.

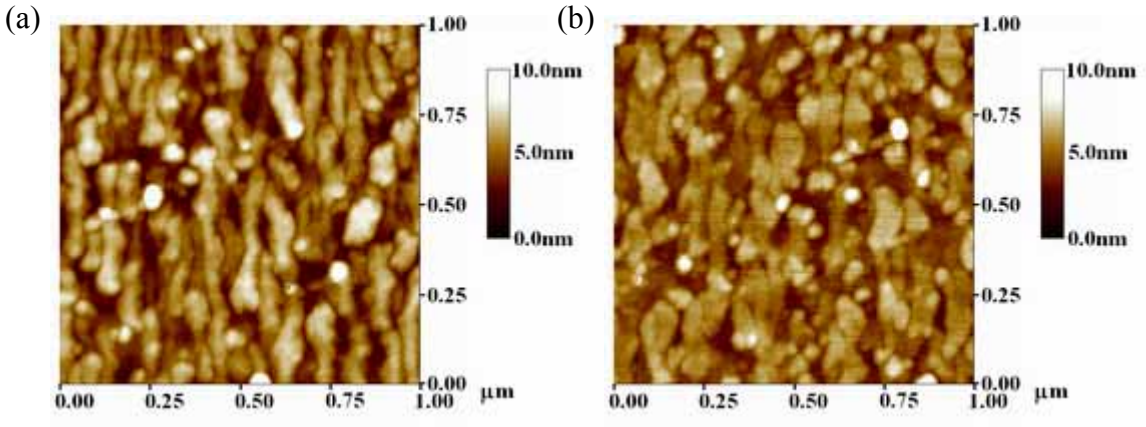

Fig.3.4: InAs quantum structure dependence on the In growth rate and the interruption time: (a) 0.056 μm/hr with 10sec interruption (Rn0072). (b) 0.55 μm/hr without interruption (Rn0073).

3.2.5 Discussion

The influence of the MBE growth condition on InAs quantum structure morphology is systematically investigated with several parameters: the InAs monolayer number, the substrate temperature, the As_2 BEP, and the In deposition rate. The suitable and stable growth condition for good InAs QWrs is obtained. The InAs wire formation should be due to the different adatom diffusion coefficient. The interruption between each InAs monolayer deposition is needed for giving enough time to In atoms to migrate along $[1\bar{1}0]$ direction. Monolayer number around 4~5 should be the best for obtaining the well-enough wires. Few InAs monolayers cannot supply enough stress along $[110]$ to form narrow wires. Moreover, few InAs monolayers cannot supply enough material to obtain long wires. However, too many InAs monolayers may introduce dislocation in the wire structures for releasing too large strain energy. Furthermore, the lumps on wires are also formed. When growing InAs QWrs, the

substrate temperature should be lower than 515℃. 510℃ is better. The long and straight InAs QWrs are obtained at this temperature. As_2 BEP should not be too high, or they will obstruct the In atoms to migrate on the surface to form wires. In this study, 1~2E-6 torr should be suitable for 0.4~0.6μm/hr In deposition rate.

3.3 GaAs Quantum Structure Growth in InGaAs matrix on InP Substrates

Recently, GaAs anti-QWrs were observed in InGaAs matrix by Dr S.D Lin[36]. GaAs anti-QWrs in InGaAs matrix lattice matched to (100) InP substrates were also elongated along $[1\bar{1}0]$ direction. The different adatom migration coefficient and different step edge reactivities along $[110]$ and $[1\bar{1}0]$ directions of Ga adatoms may make GaAs quantum structure elongate along $[1\bar{1}0]$ direction. The anisotropic stress relaxation may also play a decisive role for GaAs wire formation.

Due to that the well enough GaAs nano wires may provide a template for interesting epitaxy applications, the investigation of the influence of MBE parameters on GaAs quantum structure growth was carried out. We found that the GaAs anti-QWr growth condition in InGaAs matrix is extremely sensitive to the MBE parameters. With systematical exploration, a narrow growth window to grow the GaAs anti-QWrs was obtained.

In this section, we will study the influence of the MBE growth condition on GaAs quantum structure morphology with consideration of the several parameters: the GaAs monolayer number, the substrate temperature, the As_2 BEP, and the interruption time between each monolayer deposition. All samples were grown on normally (100) oriented InP

substrates. From these systematical experiments, an interesting wire formation behavior, different form the InAs QWr case, was observed. We found that the interruption does not help the GaAs wire structure formation. This is different from the InAs QWr formation behavior. Based on the short Ga adatom migration length (compare with the In adatom) and the experiment, an explanation is proposed. Table 3.2 is the list of growth condition for GaAs quantum structures.

	Monolayer (ML)	Substrate Temperature (℃)	Interruption between each ML (sec)	As2 pressure (torr)
Lm3795	2	510	No	1E-6
Lm3796	3	510	No	1E-6
Lm3797	4	510	No	1E-6
Lm4071	3	525	No	1E-6
Lm4095	3.5	525	No	1E-6
Lm4096	2.5	525	No	1E-6
Lm4101	3	510	No	1E-6
Lm4102	3	500	No	1E-6
Lm4108	3	515	No	1E-6
Lm4109	3	505	No	1E-6
Lm4122	3	510	No	1E-6
Lm4142	3	510	60	1E-6
Lm4145	3	510	No	1E-6
Lm4376	3	510	No	2E-6

Table 3.2: List of GaAs quantum structure growth condition

3.3.1 GaAs Monolayers

Fig.3.5 (a), (b), and (c) present the AFM images of Lm3795 (2ML), Lm3796 (3ML), and Lm3797 (4ML) at 510℃ growth temperature respectively. From these three AFM images, 3ML GaAs shows straight wire-like structures, i.e. anti-QWrs. They elongate along $[1\bar{1}0]$

direction. The dimension of these anti-QWrs is about 1.5~2nm in height and 20~30 in width. The short dash-like structures along [$1\bar{1}0$] direction are shown in Fig.3.5 (a) and (c). The height of 2ML GaAs quantum structures is about 0.5~1nm and the width of 2ML GaAs dash-like structures is similar to 3ML anti-QWrs. Compared with the 2ML GaAs dash-like structures, the 4ML GaAs dash-like structures are shorter. Their dimension is 1~2nm in height, 50~150nm in length, and 20~40 in width.

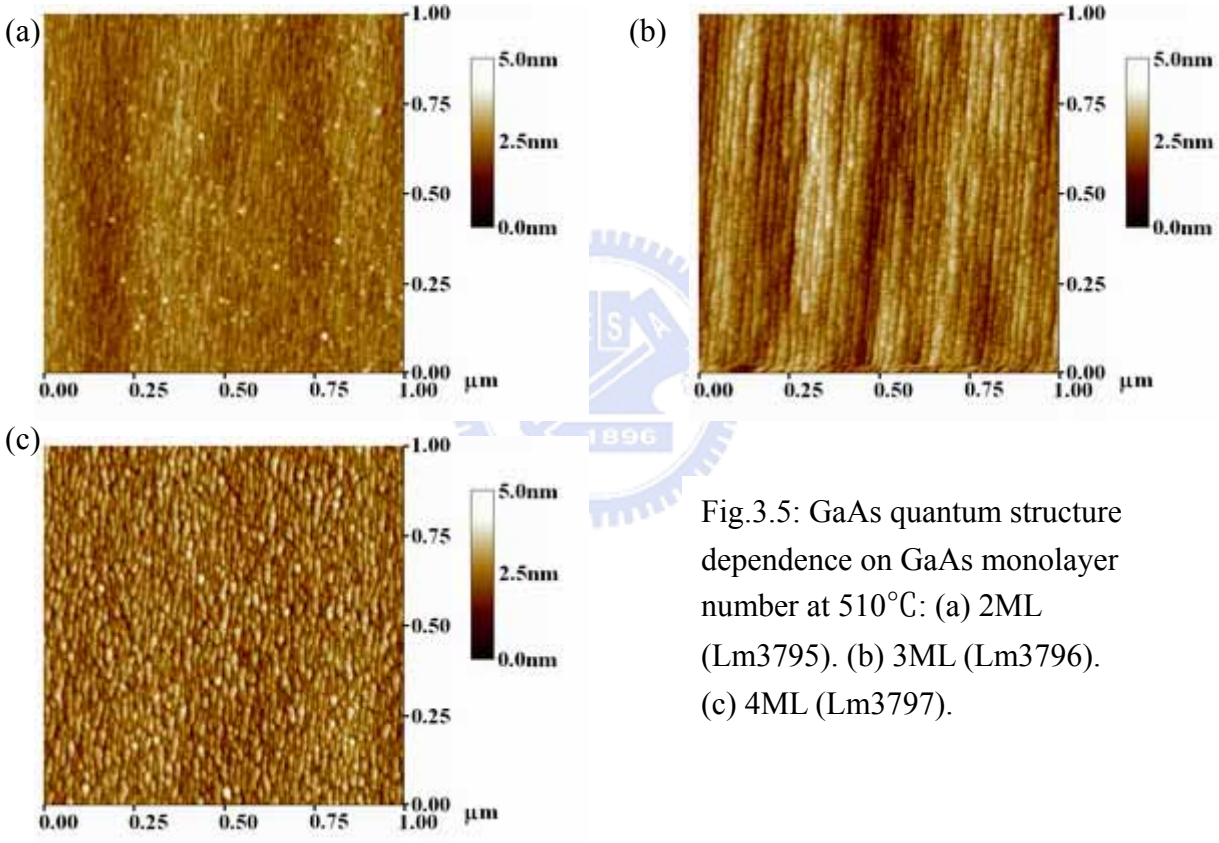

Fig.3.5: GaAs quantum structure dependence on GaAs monolayer number at 510℃: (a) 2ML (Lm3795). (b) 3ML (Lm3796). (c) 4ML (Lm3797).

The AFM images in Fig.3.6 are the results of (a)Lm4071 (3ML), (b)Lm4095 (2.5ML), and (c)Lm4096 (3.5ML) at 525℃ growth temperature. In this growth temperature, these three samples all formed dash-like structures. From the comparison among these three images, the dash-like structures formed by 3ML GaAs shown in Fig.3.6(a) are longer than the other two

cases shown in Fig.3.6 (b) and (c). Therefore, 3ML GaAs is the best monolayer number for GaAs wire-like quantum structure growth. However, the structures in Fig.3.6(a) is only dash-like, but the structure in Fig3.5(a) is wire-like. Thus, the growth temperature at about 510℃ is more suitable than at 525℃.

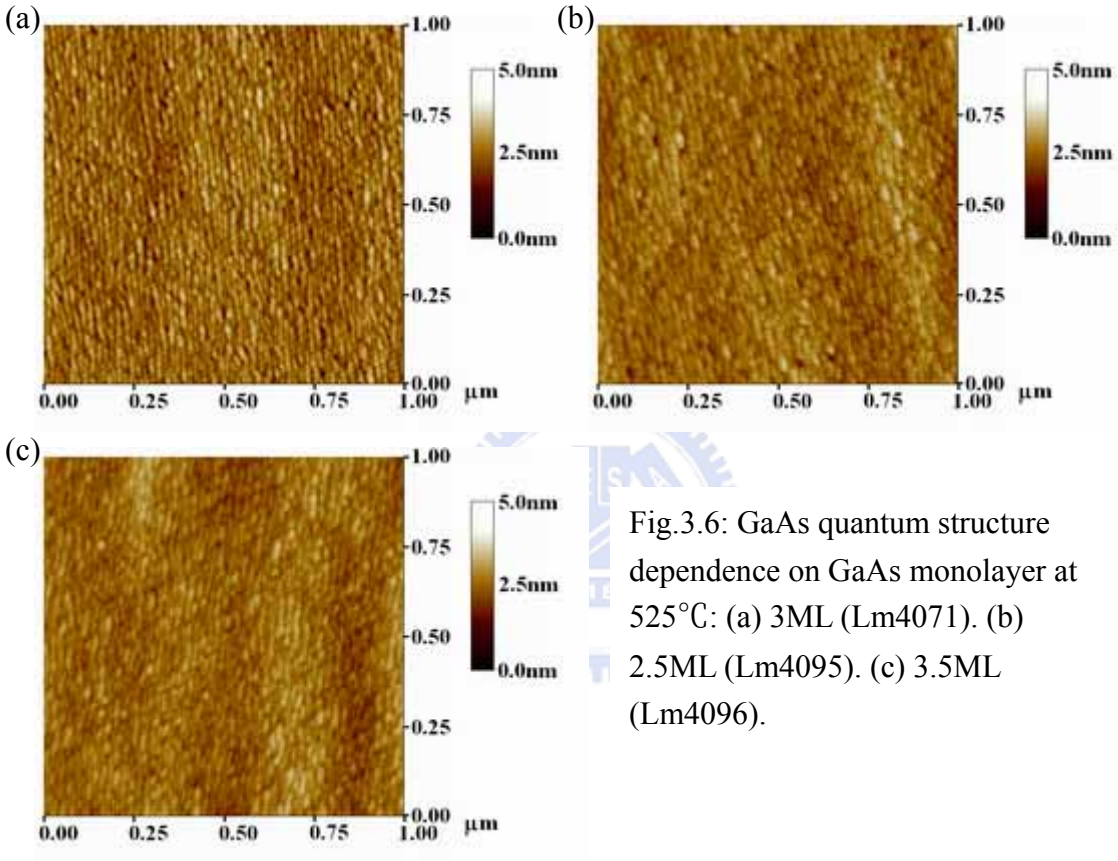

Fig.3.6: GaAs quantum structure dependence on GaAs monolayer at 525℃: (a) 3ML (Lm4071). (b) 2.5ML (Lm4095). (c) 3.5ML (Lm4096).

3.3.2 Substrate Temperature

The Images in Fig.3.7 are the AFM results of (a)Lm4071 (525℃), (b)Lm4101 (510℃), (c)Lm4102 (500℃), (d)Lm4108 (515℃), (e)Lm4109 (505℃), and (f)Lm4122 (510℃). Lm4101 and Lm4122 have the same growth parameters as Lm3796 does. From the comparison among these six images in Fig.3.7, Lm4101 and Lm4122 show well enough wire-like structures.

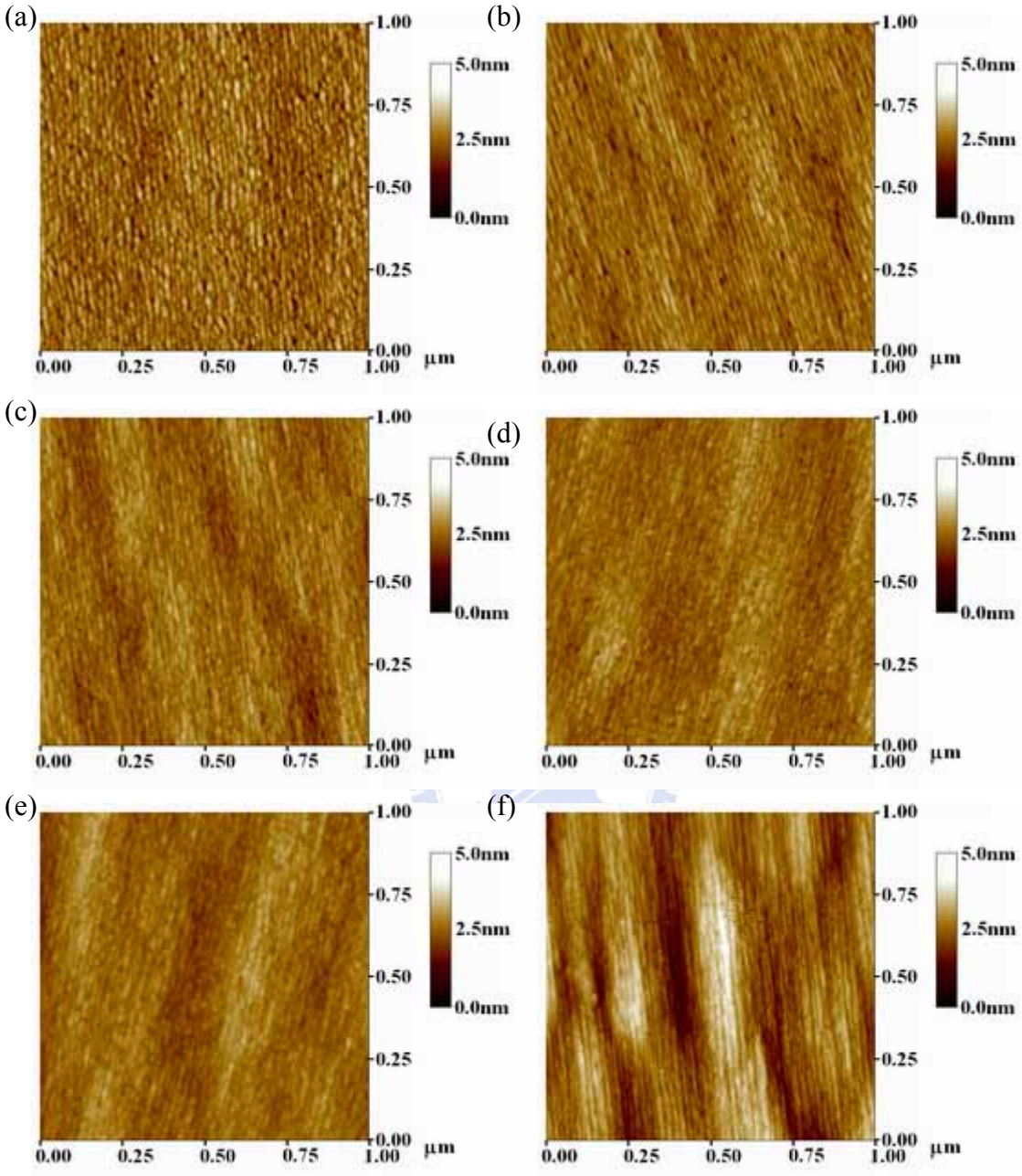

Fig.3.7: GaAs quantum structure dependence on substrate temperature: (a) 525℃ (Lm4071). (b) 510℃(Lm4101). (c) 500℃(Lm4102). (d) 515℃(Lm4108). (e) 505℃ (Lm4109). (f) 510℃(Lm4122).

Therefore, 510℃ growth temperature is the most suitable temperature for the GaAs anti-QWr growth. Lm4102 was grown at 500℃, but the dash is much shorter, similar to the Lm4071. Lm4108 and Lm4109 also have not long enough wire-like structures. However, the dash-like structures in the AFM picture of Lm4108, grown at 515℃, seem longer and aligned straighter in $[1\bar{1}0]$ direction. As a result, the growth temperature at 510℃ is the most proper temperature to obtain the GaAs anti-QWrs. Although the anti-QWrs in Lm4101 and Lm4122 are not as good as those in Lm3796 are, these results are similar and repeatable.

3.3.3 As_2 BEP

Fig.3.8 are the AFM results of (a)Lm4145 (As_2 BEP~1E-6torr) and (b)Lm4376 (As_2 BEP~2E-6torr). Lm4145 has all the same condition for Lm4101 and Lm4122. The AFM results of Lm4145, Lm4101, and Lm4122 show that their structures all form anti-QWrs.

However, under higher As_2 BEP, i.e. Lm4376, the AFM image shows short dash-like structures and these structures roughly aligns along $[1\bar{1}0]$ direction. This result means that 2E-6torr As_2 BEP is too high for 3ML GaAs to form anti-QWrs.

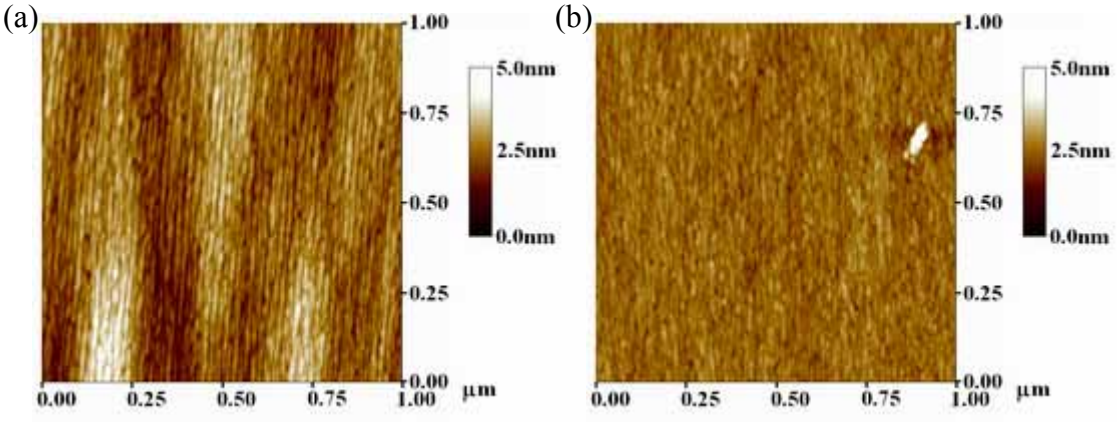

Fig.3.8: GaAs quantum structure dependence on As_2 BEP: (a) As_2 BEP~1E-6torr (Lm4145). (b) As_2 BEP~2E-6torr (Lm4376).

3.3.4 Interruption

Lm4142 was used to test an idea: add more time for Ga adatoms to migrate along [$1\,\bar{1}\,0$] direction for obtaining well-enough wires. There was 60sec interruption between each monolayer deposition, see Table 3.2. The comparison of Lm4122 and Lm4142 is shown in Fig.3.9. It is surprised that the interruption does not add the wire formation. The AFM image of Lm4142 shows that the 3ML GaAs forms the short dashes along [$1\,\bar{1}\,0$] direction, and these short dashes roughly align along [$1\,\bar{1}\,0$] direction. The dimension of these short dashes is 0.5~1.5nm by 10~30nm.

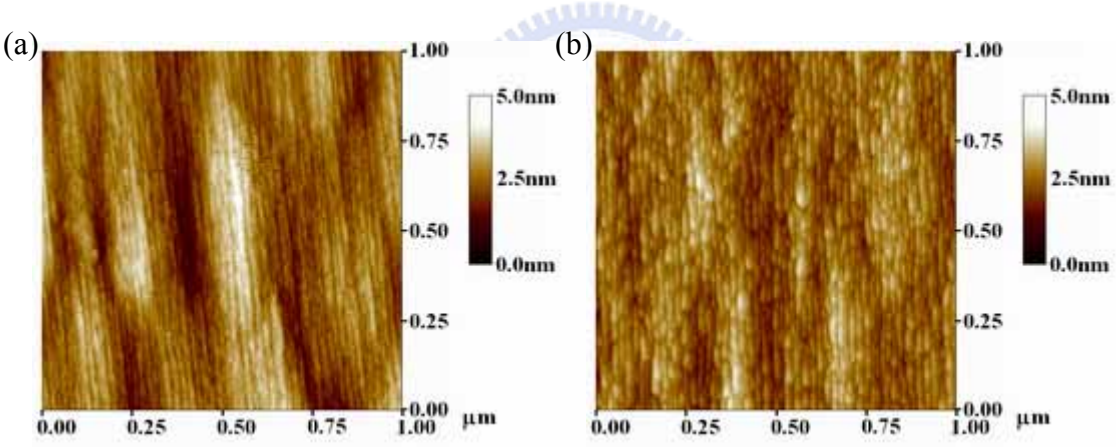

Fig.3.9: GaAs quantum structure dependence on the interruption time: (a) Without interruption (Lm4122). (b) 60sec interruption between monolayer (Lm4142).

3.3.5 Discussion

In this section, the growth condition is systematically investigated and the appropriate approach is found for GaAs anti-QWr formation. There is an interesting difference between InAs QWr and GaAs anti-QWr formation. Interruption helps InAs to form QWrs, but

obstructs GaAs to form anti-QWrs. Moreover, migration length of Ga adatoms is shorter than that of In adatoms. According to this difference and the short migration length of Ga adatoms, the anisotropic stress relaxation should be the decisive role for GaAs wire formation. As a result, an explanation is proposed.

The Ga atom in InGaAs has different adatom migration coefficient and different step edge reactivities along [110] and [$1\bar{1}0$] directions. These effects make the self-assembled GaAs quantum structures prefer to formed dash-like structures. Furthermore, it is well-known that there are many growth parameters influence the total free energy of the deposition film. The free energy is a very important factor for the deposition film to form self-assembled quantum structures. Due to the substrate-film interface energy along [110] and [$1\bar{1}0$] directions is different. The stress relaxation for GaAs wire formation is anisotropic, which makes the 3D formation speed along [110] is quicker than along [$1\bar{1}0$]. We propose that under proper growth parameters, the stress of the GaAs deposition film along [110] direction is much strong, but is much weak in [$1\bar{1}0$] direction. As a result, 3D formation process in [110] direction is much quick, but in [$1\bar{1}0$] direction is much slow. In our experiments, the proper growth parameters are found to be 510℃ growth temperature, 0.1μm/hr Ga growth rate under about 1E-6 BEP of As_2 beam flux, and the surface of InGaAs matrix lattice matched to normally (100) oriented InP substrates.

As 3D formation is started, parts of Ga atoms are needed for the quick 3D growth in [110] direction to release the strong stress, wire-like structures start to from. With 3D growth proceeding in [110] direction, Ga atoms quickly move to the tops of the wires to relax the strain energy. Because Ga atoms have shorter migration length than In atoms have on the surface. The Ga atoms on the tops of each wire are almost supplied form the neighbor two trenches. If the deposition GaAs is fewer than 2.5 ML, The amount Ga atoms, from the neighbor two trenches, migrating to the wire peaks is not enough to relax the strain energy to

minimize the total free energy. As a result, this forces Ga atoms in the lower regions in each wire to migrate up to the higher regions for continuously releasing the strain energy and the wires are cut off to form dash-like structures. This is why 2ML and 2.5ML GaAs both form short dash-like structures and are roughly aligned along $[1\,\bar{1}\,0]$ direction.

However, if the supply of Ga atoms is sufficient, the 3-D formation in $[110]$ direction makes the strain energy in $[110]$ direction have enough release to minimize the system total free energy. Furthermore, the 3D formation in $[1\,\bar{1}\,0]$ direction is much slow under the proper growth condition. As a result, the wires will not be cut off. This is why 3ML GaAs forms anti-QWrs in the proper growth condition.

However, if too many Ga atoms is supplied, the stress in the deposition film will become larger, even in $[1\,\bar{1}\,0]$ direction. As a result, the speed of the 3D formation in $[1\,\bar{1}\,0]$ direction becomes quick, too. Therefore, when GaAs monolayer number is above 3.5, the larger stress makes the GaAs film form short dash-like structures.

For Lm4142 sample, there is a long time interruption between each monolayer deposition. Although the 3D formation speed in the $[1\,\bar{1}\,0]$ direction is slow under the proper growth condition, it is still proceeding. As a result, the long wire-like structures become short dash structures.

If the growth parameters are not to achieve the proper growth condition, there is not large enough stress ratio of $[110]$ direction to $[1\,\bar{1}\,0]$ direction. Thus, the difference of the 3D formation speed between $[110]$ direction and $[1\,\bar{1}\,0]$ direction is not large enough. As a result, the 3ML GaAs will not form anti-QWrs, and just form dash-like structures.

3.4 Summary

The growth parameters of InAs quantum structures in InGaAs matrix on (100) InP substrates are systematically investigated. The mechanisms of InAs QWr growth are discussed. The different In adatom diffusion coefficient along $[110]$ and $[1\bar{1}0]$ should be the main factor for InAs wire formation. The proper growth window to obtain well enough InAs QWr is explored. In a suitable growth condition, smooth and straight InAs QWrs with length above 1μm can be obtained.

An investigation for GaAs quantum structure is carried out. A narrow growth window for growing GaAs anti-QWrs is also acquired. Unlike the InAs QWr case, the application of interruption between each monolayer deposition cannot help to generate well enough wires. Most samples show that the GaAs nano structures form short dashes, which are elongated along $[1\bar{1}0]$ direction. According to these experiment results and the short migration length of Ga adatoms, large stress ratio of $[110]$ direction to $[1\bar{1}0]$ direction should be the significant reason of GaAs wire formation. Basing on the anisotropic stress effect, we propose an explanation for the formation of GaAs quantum structures.

Chapter 4

Ordering of Stacked InAs/GaAs Nano Wires in InGaAs/InAlAs Matrix on (100) InP Substrates

4.1 Introduction

The self-assembled In(Ga)As QDs grown on GaAs has been widely investigated since early 1990s[3]. Recently, self-assembled InAs quantum structures grown on InP substrates [32,76,77], and GaAs anti-QWrs in InGaAs matrix lattice matched to InP substrates also were reported[36]. These quantum structures, when closely stacked, often have interesting ordering behaviors. Vertical alignment behavior of In(Ga)As QDs in GaAs[37,38] drew lots of attentions at the intital stage. Later on, other self-asssembled QD systmes showed more interesting stacked behaviors, such as the anticorrelated submolayer CdZnSe QDs in ZnSe[39] and the face-center-cubic (f.c.c.) anti-correlation structure of PbSe QDs in PbEuTe[40]. Stacked InAs quantum structures in the materials lattice matched on InP substrates were also reported[31,33,81] lately. Stacked InAs quantum structures show verticaly alignment in $In_{0.53}Ga_{0.47}As$ and $In_{0.53}Ga_{0.37}Al_{0.1}As$ matrix, but show staggered alignment in $In_{0.52}Al_{0.48}As$ matrix. However, the mechanism for the strange stacking behavior of InAs QWrs in InAlAs matrix is still not clear.

In this chapter, the stacked InAs/GaAs quantum structures in InGaAs/InAlAs matrix on (100) InP substrates by MBE were investigated by the TEM technique. Cross-sectional TEM images demonstarte that several monolayers of InAs and GaAs formed nano wires in these

InGaAs and InAlAs matrices, and that stacked InAs QWrs and GaAs anti-QWrs in InGaAs matrix are vertically aligned to form rectangular lattices. In InAlAs matrix, however, the stacked InAs QWrs are staggered alignment, similar to a body-centered-cubic (b.c.c.) lattice. We found that the stacking behaviors of InAs wires in InGaAs matrix and in InAlAs matrix have the agreements on the previous reports[31,33,81], and reported that the stacking behavior of GaAs anti-QWrs in InGaAs matrix, which was the first time to be studied.

Moreover, from the TEM pictures, the composition modulation is clearly observed in the post grown InGaAs and InAlAs matrices on the InAs or GaAs nano wires. Interestingly, the behavior of the composition modulation distribution in InGaAs matrix and in InAlAs matrix is different. The composition modulation distribution develops vertically in InGaAs matrix, but obliquely in InAlAs matrix. The formation of composition modulation in InGaAs and InAlAs matrices is discussed and explained. Based on the composition modulation, we explain the stacking behavior of the wire-like structures.

4.2 Epitaxy Structures

The samples were grown on normally (001) oriented InP substrates with a Varian Gen II solid source MBE system. Three kinds of wire-like quantum structures, including GaAs anti-QWrs in InGaAs matrix, InAs QWrs in InGaAs matrix, and InAs QWrs in InAlAs matrix were grown on top of a 0.5μm InGaAs or InAlAs buffer layer, lattice matched to InP substrate. In these stacked structures, each period consisted of several monolayers of InAs or GaAs for self-assembled nano wire growth and a 6nm matrix material as the spacer. Fig.4.1 is the skectch of the epitaxy structure.

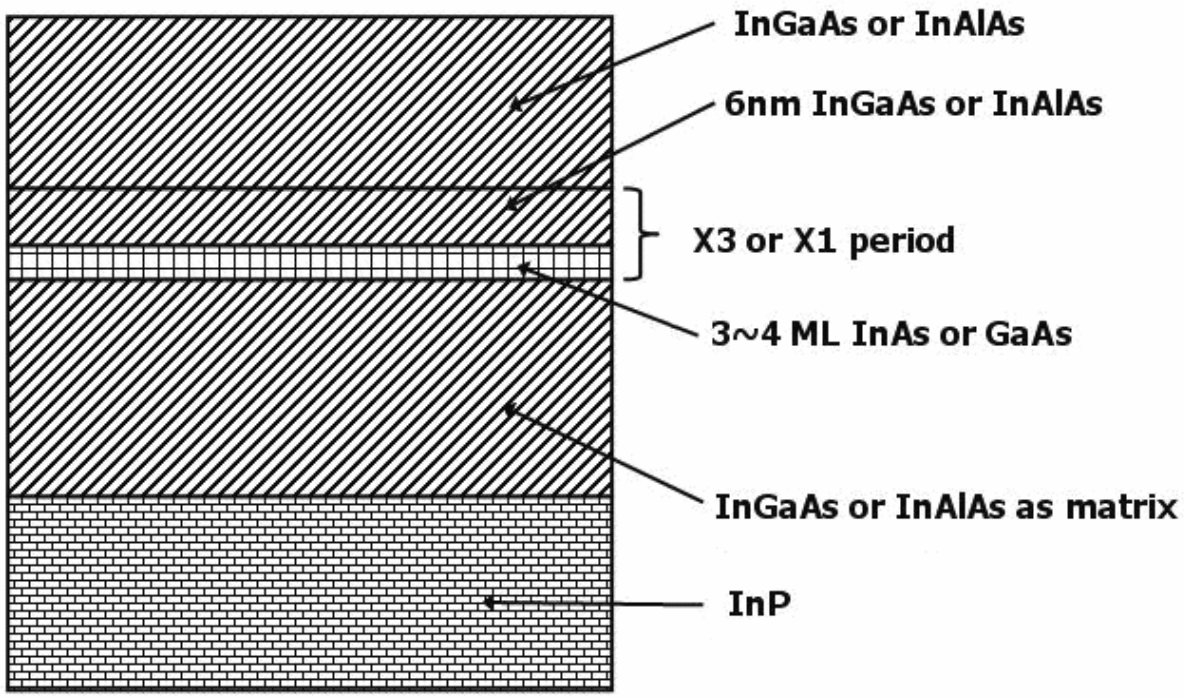

Fig.4.1: The sketch of the epitaxy structure

4.3 Transmission Electron Microscope Results

A JEOL electron microscope, JEM2010, with a beam energy of 200kV was used to take the TEM pictures. The cross-sectional, bright field TEM pictures of three different kinds of nano wires were taken. The cross-sectional pictures were taken in $(1\bar{1}0)$ planes, which were perpendicular to the wire orinetation, and in (110) planes, which were parallel to the wire orientation. Moreove, the high resolution TEM (HRTEM) pictures of $(1\bar{1}0)$ planes were also taken for these samples.

Fig.4.2 (a) and (b) is the cross-sectional TEM pictures of GaAs anti-QWrs in InGaAs matrix of $(1\bar{1}0)$ and (110) planes, respectively. The cross-sectional TEM pictures of InAs QWrs in InGaAs matrix of $(1\bar{1}0)$ and (110) planes are both shown in Fig.4.3. For InAs

QWrs in InAlAs matrix case, the cross-sectional TEM pictures of $(1\bar{1}0)$ and (110) planes are shown in Fig.4.4.

In these corss-sectional TEM pictures, each sample contained three layers of nano wires. Because the light atoms scatter the incident electron beam lightly and the heavy atoms scatter the incident electron beam heavily, the light atoms give bright images and the heavy atoms give dark images in the TEM pictures. As a result, GaAs regions are brighter in Fig.4.2, but InAs regions are darker in Fig.4.3 and Fig.4.4.

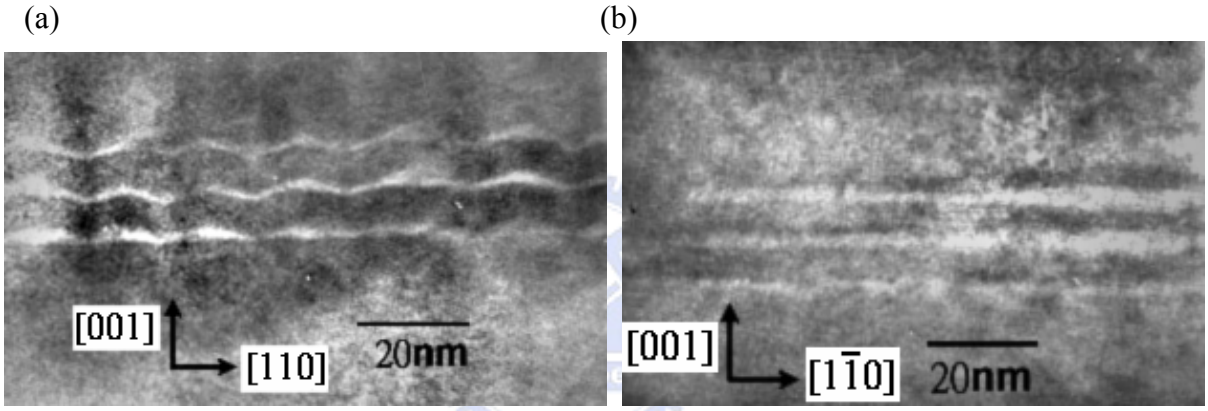

Fig.4.2: Cross-sectional TEM pictures of 3ML GaAs in InGaAs matrix: (a) $(1\bar{1}0)$ plane. (b) (110) plane.

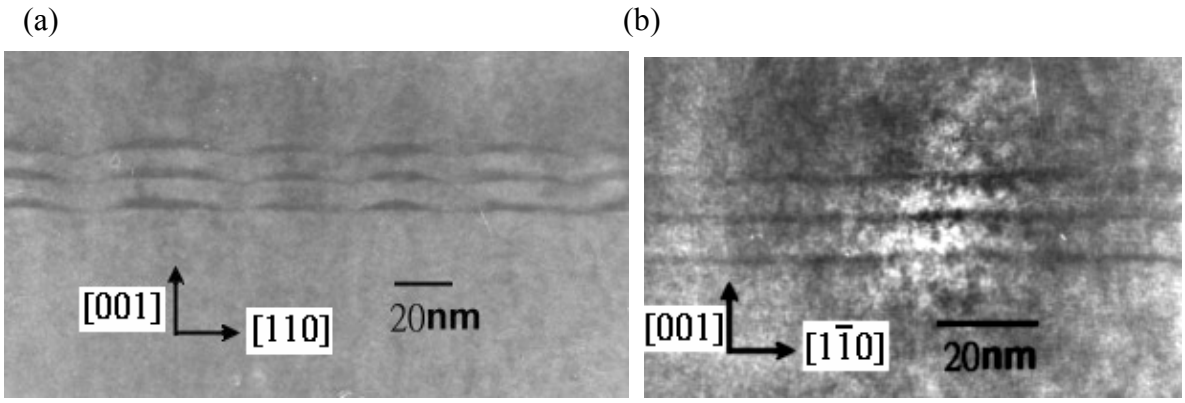

Fig.4.3: Cross-sectional TEM pictures of 3ML InAs in InGaAs matrix: (a) $(1\bar{1}0)$ plane. (b) (110) plane.

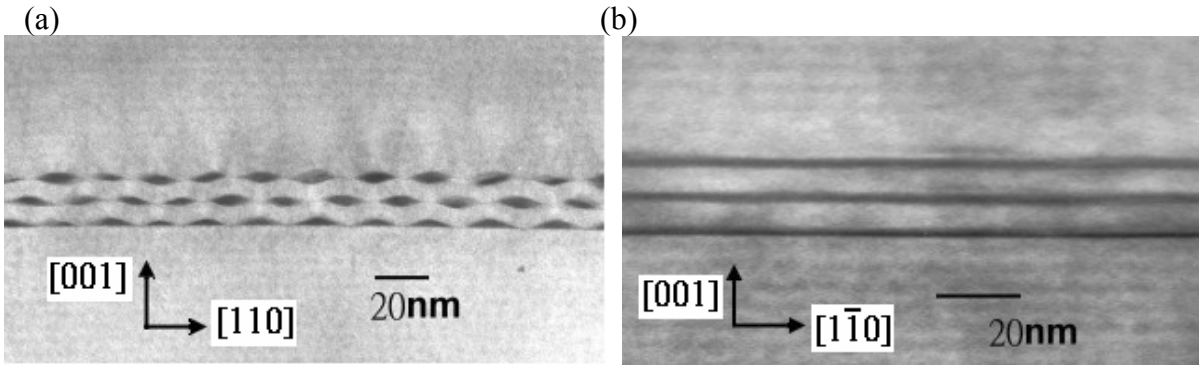

Fig.4.4: Cross-sectional TEM pictures of 3.75ML in InAlAs matrix: (a) $(1\,\bar{1}\,0)$ plane. (b) (110) plane.

Fig.4.2(a), Fig.4.3(a), and Fig.4.4(a) are the the cross-sectional TEM pictures taken in $(1\,\bar{1}\,0)$ planes, perpendicular to the $[1\,\bar{1}\,0]$ direction. All of these firues show nano dot-like or short dash-like patterns. However, Fig.4.2(b), Fig.4.3(b), and Fig.4.4(b), these cross-sectional TEM pictures taken in (110) planes, reveal the apparent straight wire-like patterns with 3 lines in the pictures. The (110) plane is parallel to the $[1\,\bar{1}\,0]$ direction. Therefore, these cross-sectional TEM picutres show the evidences that several monolayers InAs and GaAs all form nano wire structures, elongated along the $[1\,\bar{1}\,0]$ direction, in InGaAs matrix and in InAlAs matrix experimentally. It demonstrate that 3ML GaAs, 3ML InAs, and 3.75ML InAs forms anti-QWrs in InGaAs matrix, QWrs in InGaAs matrix, and forms QWrs in InAlAs matrix, respectively. The results, that InAs forms QWrs and GaAs forms anti-QWrs in InGaAs matrix, are consist with the wire-like structures in the AFM pictures discussed in Chapter.3. In Chapter3, we found self-assembled quantum structures of InAs and GaAs are QWrs and anti-QWrs respectively, which both elongate along the $[1\,\bar{1}\,0]$ direction, in InGaAs matrix under suitable growth condition.

As shown in Fig.4.2 and Fig.4.3, both stacked GaAs anti-QWrs and stacked InAs QWrs are arranged in a rectangular lattice in InGaAs matrix. Different layers of wires are aligned vertically. The GaAs anti-QWrs shown in Fig.4.2(a) has a lateral lattice constant around 15nm, and dimensions of 12-20nm in width and 1.5-3nm in height. The InAs QWrs in Fig.4.3(a) has a larger lattice. The lateral periodicity is about 30nm. The cross-sectional dimensions of the wires are about 25~40nm by 2~4nm. The arrangement of the InAs QWrs in InAlAs shown in Fig.4.4(a) is different from the wire-like quantum structures grown in InGaAs matrix. Different layers indicate in a checker board pattern to from a b.c.c. like lattice. Their lateral lattices constant is around 20nm, and the wires cross-section areas are about 16~22nm by 2~4nm.

However, by focusing on the shapes of the wires in Fig.4.2(a), Fig.4.3(a), and Fig.4.4(a), the wire cross-sectional shape in Fig.4.4(a) is apperantly different from that in Fig.4.2(a) and Fig.4.3(a). The first layer of wires in each case always shows a dome-like shape, but the subsequent layers are different. For nano wires in InGaAs matrix in Fig.4.2(a) and Fig.4.3(a), the wires in the upper layers have crescent-like shape. It is quite clear that they are riding above a ripple surface created by the layer underneath, and form on the peaks of the ripple surface. In Fig.4.4(a), showing InAs QWrs in InAlAs matrix, we can see a very different situation. The QWrs on the upper layers form in the valleys of the ripple, and their shape are more like a flying saucer.

Fig.4.5 (a), (b), and (c) show the cross-sectional HRTEM pictures in $(1\bar{1}0)$ planes for staked GaAs anti-QWrs in InGaAs matrix, InAs QWrs in InGaAs matrix, and InAs QWrs in InAlAs matrix respectively. In these three pictures, no dislocation is found. Therefore, these wire-like quantum structures in this study were all under coherent epitaxy.

(a)

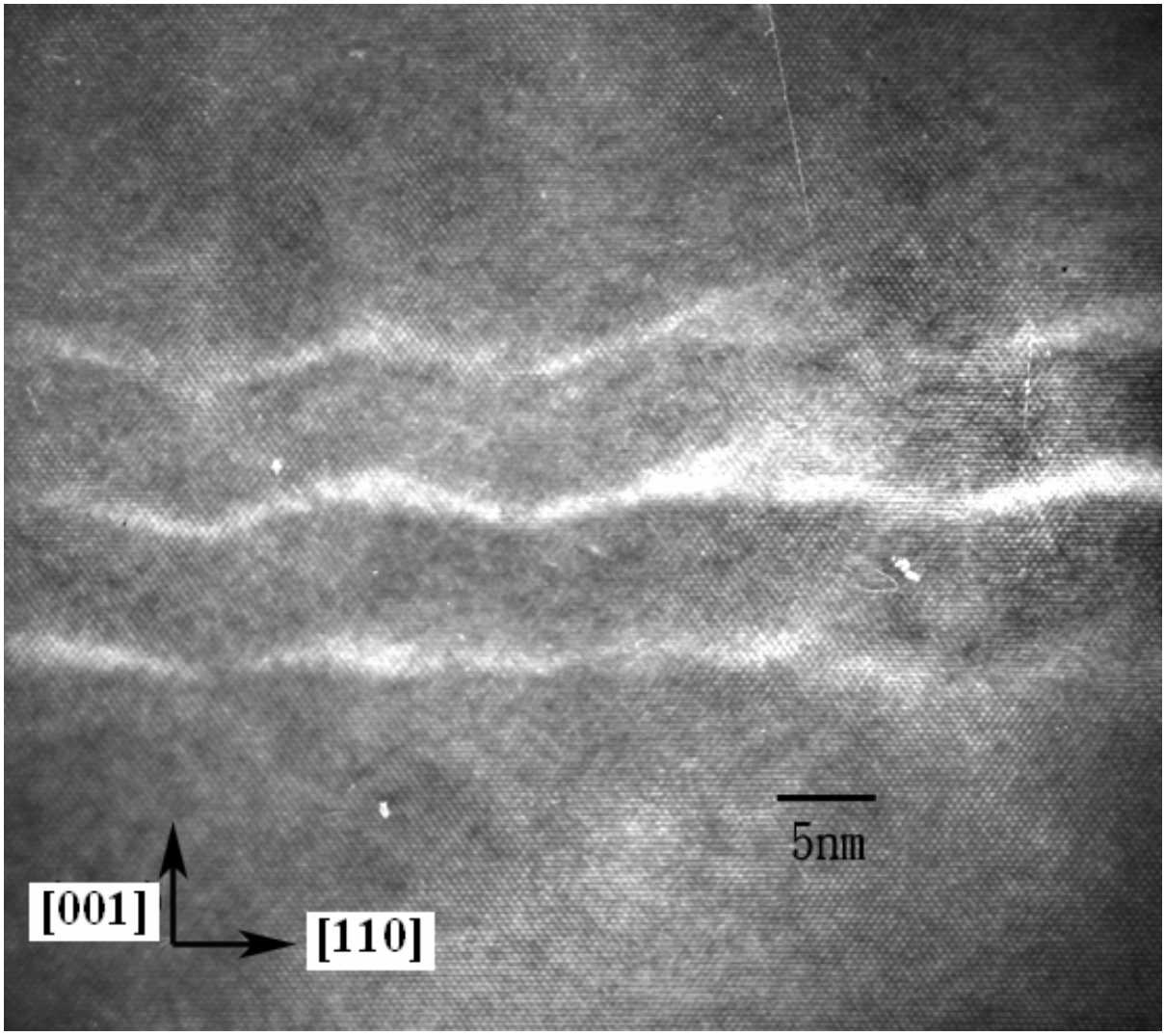

Fig.4.5(a): The cross-sectional HRTEM picture taken in the $(1\bar{1}0)$ plane of staked 3ML GaAs anti-QWrs in InGaAs matrix

(b)

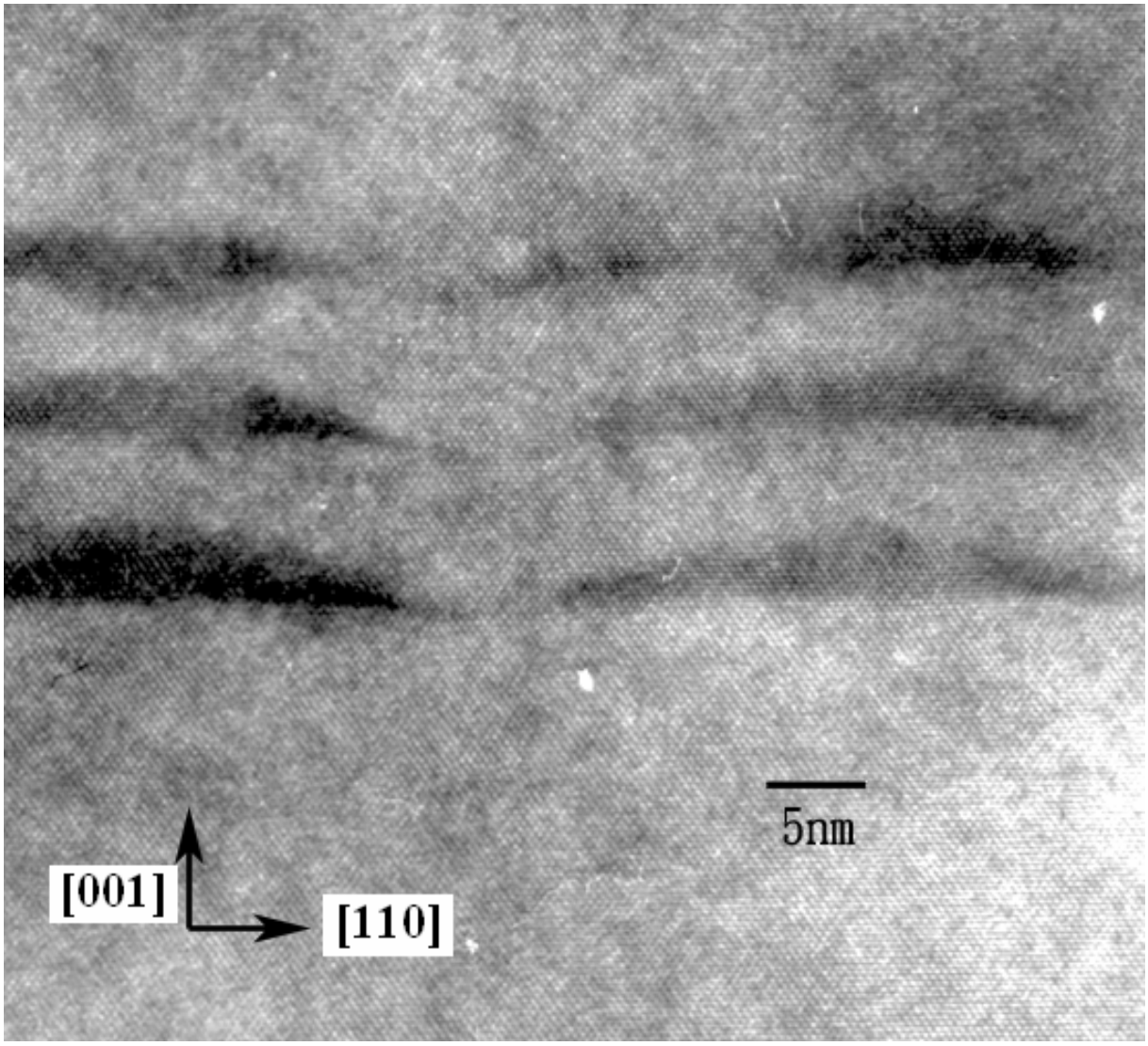

Fig.4.5(b): The cross-sectional HRTEM picture taken in the $(1\bar{1}0)$ plane of staked 3ML InAs QWrs in InGaAs matrix

(c)

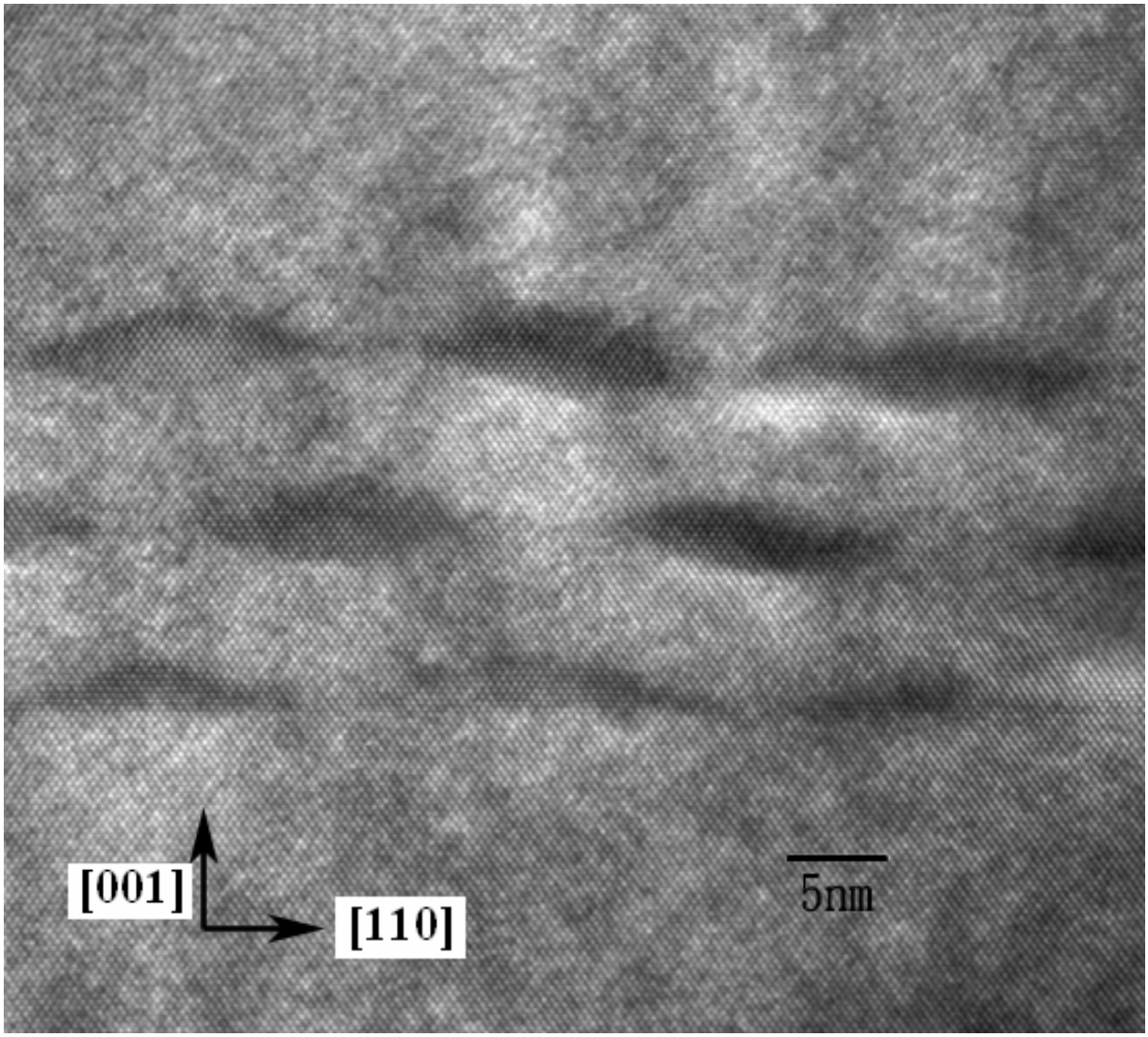

Fig.4.5(c): The cross-sectional HRTEM picture taken in the $(1\bar{1}0)$ plane of staked 3.75ML InAs QWrs in InAlAs matrix

To obtain the composition information in these quantum structures, a tilting procedure was used to enhance compositional contrast during TEM imaging[82]. Fig.4.6 shows the results of these samples in the $(1\bar{1}0)$ plane.

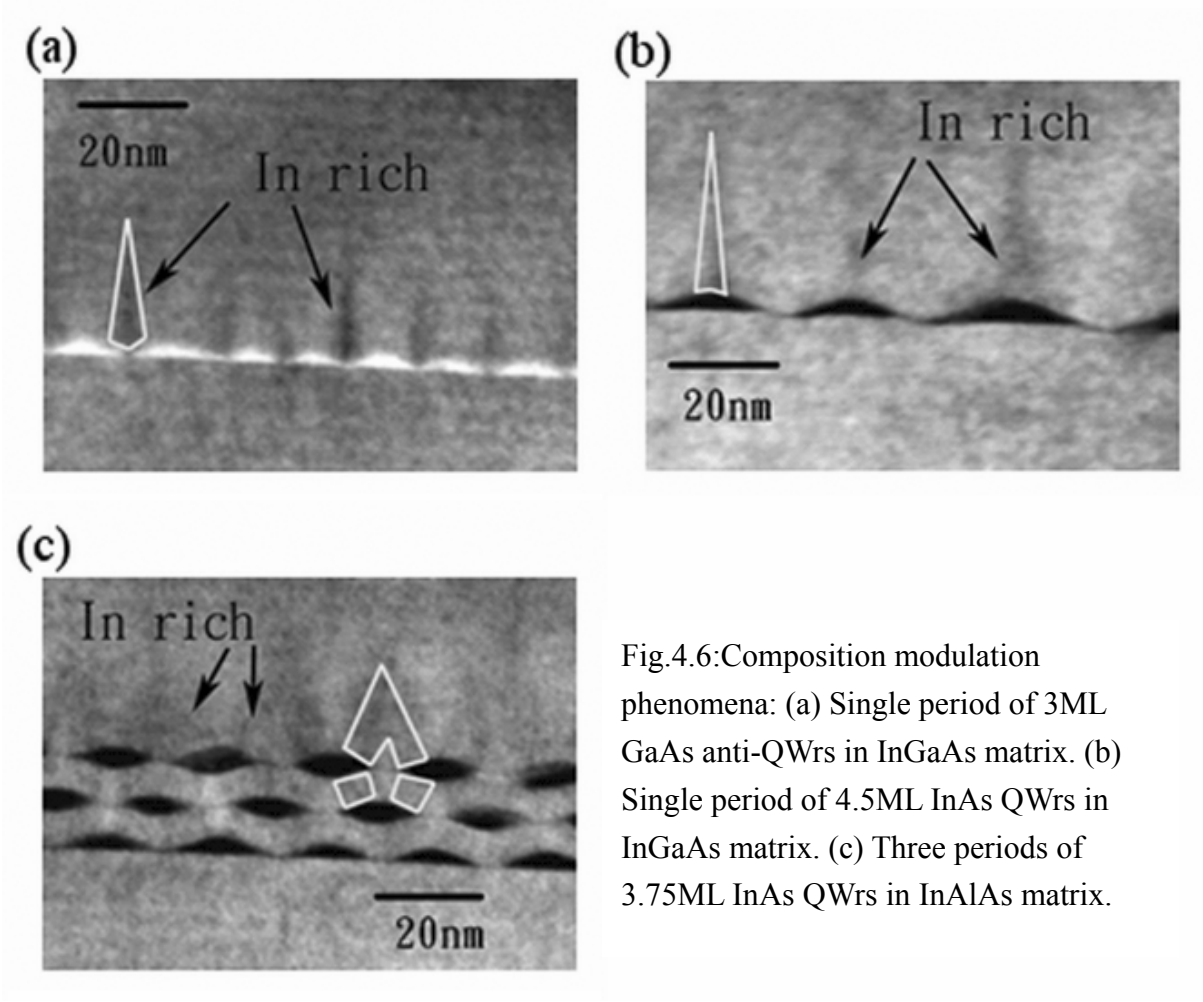

Fig.4.6:Composition modulation phenomena: (a) Single period of 3ML GaAs anti-QWrs in InGaAs matrix. (b) Single period of 4.5ML InAs QWrs in InGaAs matrix. (c) Three periods of 3.75ML InAs QWrs in InAlAs matrix.

With careful examination in the matrix regions adjacent to the nano wires in these figures, slightly darker or brighter stripes can be seen in the vicinity of these wires. The darker stripes indicated by the arrows in Fig.4.6 are believed to be In-rich. The brighter stripes are believed to be either Ga-rich or Al-rich depending on InGaAs or InAlAs matrix. In Fig.4.6(a), the darker stripes are above the valleys of GaAs anti-QWrs. This is a redistribution of In atoms in the InGaAs layers, and the In rich regions are originated from the valleys of the GaAs anti-QWrs. For InAs QWrs in InGaAs shown in Fig.4.6(b), we can find that the In-rich

regions develope above the peaks of InAs QWrs. It is very interesting that, for InAs QWrs in InAlAs matrix shown in Fig.4.6(c), the In-rich regions (darker area) develope obliquely from the upper sidewalls of each QWrs and terminate at the nearest QWrs in next layer.

4.4 Explanation for Stacking Behaviors of Wire-like Quantum Structures

Fig.4.7 (a), (b), and (c) sketch the composition modulation and the formation of oredered GaAs anti-QWrs in InGaAs matrix, InAs QWrs in InGaAs matrix, and InAs QWrs in InAlAs matrix respectively.

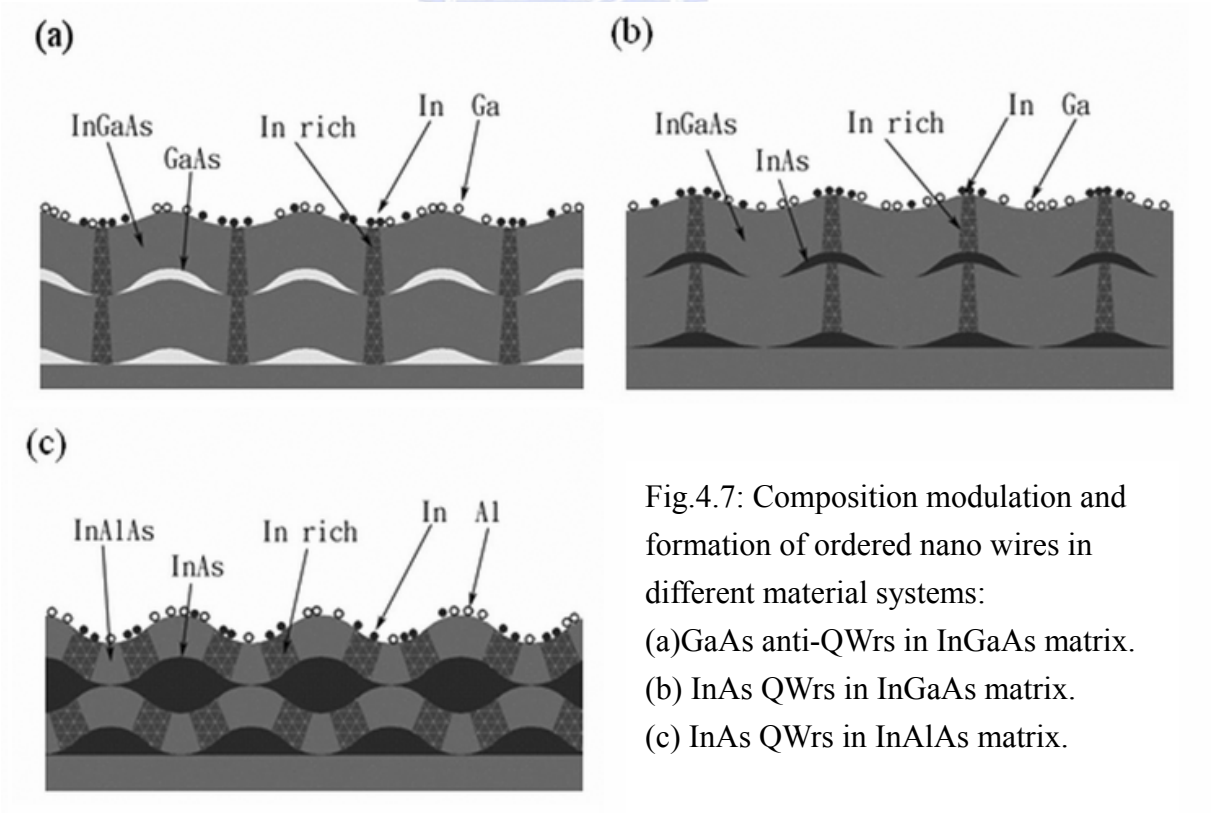

Fig.4.7: Composition modulation and formation of ordered nano wires in different material systems:
(a)GaAs anti-QWrs in InGaAs matrix.
(b) InAs QWrs in InGaAs matrix.
(c) InAs QWrs in InAlAs matrix.

The composition modulation developed in the post-grown matrix around the wire-like quantum structures can be understood as follows. During the growth of InGaAs matrix or InAlAs matrix after the wire-like quantum structures are formed, adatoms prefer to migrate to less strained regions to reduce strain energy caused by the nano wires beneath. However, there are some differences among these three cases. We will disucuss the composition modulation phenomena and the interesting stacking behaviors of these three cases in the following three paragraphs one by one.

The sketch in Fig.4.7(a) depictes the case of GaAs anti-QWrs in InGaAs matrix. Due to the existence of the wires, the strain distribution in the InGaAs layer on top the wires is not uniform. The regions directly above the anti-QWrs are more compressively strained because of the thicker GaAs underneath. Since In atoms are larger than Ga atoms, they tend to move to regions that are not so compressively strained to reduce the strain energy. Hence, the composition of InGaAs is modulated periodically in the lateral direction perpendicular to the GaAs anti-QWrs, i.e. along [110] direction. Directly above each GaAs anti-QWrs, the InGaAs layer is more Ga rich, while above the valleys (between the GaAs anti-QWrs), it is In rich. As a result, dark stripes are observed between the GaAs anti-QWrs. The thin InGaAs spacer layer above each layer of GaAs anti-QWrs roughly maintains the ripple-like morphology of the GaAs anti-QWrs underneath. For the growth of the second layer of GaAs anti-QWrs, they will prefer the Ga rich regions to minimize the strain energy due to the composition modulation in the InGaAs matrix layer underneath. As a result, the stacked GaAs anti-QWrs are aligned vertically. Because the Ga rich regions are in the peaks of the ripple, the wires formed on top become crescent like.

The situation is similar for the case of InAs QWrs in InGaAs matrix (see the sketch in Fig.4.7(b)). The thin InGaAs spacer layer above the first InAs QWrs follows the ripple morphology of the QWrs, and has composition modulation because of the InAs QWrs

underneath. As growing the InGaAs layer, the In atoms will migrate to peaks and the Ga atoms will migrate to valleys in order to reduce the tensile strain caused by the InAs QWrs layer underneath. For the same reason shown in the previous paragraph, the subsequent InAs QWrs grow on the top of In-rich regions, the peaks of the ripple. As a result, the stacked InAs QWrs in InGaAs matrix are also aligned vertically, and the InAs QWrs in the upper layers have crescent shape.

The situation for InAs QWrs in InAlAs matrix, however, is more complicated. Al adatoms are much harder to migrate on the surface at the growth temperature used here[83]. The growth of the InAlAs layer and its atomic distribution are subjected to two competing forces. Because the thin InAlAs spacer layer grown on the InAs QWrs follows the ripple-like morphology, the In atoms, which are more mobile, tend to migrate toward the valleys of the ripple to smooth out the surface[84]. On the other hand, the strain distribution caused by the InAs QWrs underneath tends to drive the In atoms to the tops of the ripple. Thus, compromising these two factors, In-rich regions happen on the upper sidewalls of the InAs QWrs, and then develope obliquely to minimize the total energy. Fig.4.7(c) illustrates how the In rich regions are developed in the InAlAs matrix. The two In rich stripes from adjacent InAs QWrs converge directly above the valley of the ripple. Therefore, when the next layer of InAs QWrs are deposited, they are grown directly above the valleys between the previous InAs QWrs. In this way, a staggered b.c.c. like lattice is formed. Because the following InAs QWrs are grown on the valleys of the ripple, the shape of the InAs QWrs in the top layers is like a flying saucer.

4.5 Summary

In this work, we studied the stacking behaviors of InAs and GaAs quantum structures in InGaAs/InAlAs matrix on (100) InP substrates with the TEM technique. The cross-sectional TEM pictures verify that InAs and GaAs from nano wire structrues, elongated along $[1\bar{1}0]$ direction. These TEM pictures also show that different layers of wires are strongly and correlately to form lattice-like periodic structures. The GaAs anti-QWrs and InAs QWrs in InGaAs matrix are vertically aligned to from a rectangular lattice. However, the InAs QWrs in InAlAs formed a b.c.c. like lattice. From the cross-sectional HRTEM pictures, these nano wires were all under coherent epitaxy. The compositionally modulation in these samples are observed clearly. We propose a growth kinetics viewpoint to account the composition modulation in InGaAs matrix and InAlAs matrix. Then, based on the composition modulation phenomena, we explain the subsequent fascinating ordered arrangement of these closed stacked GaAs anti-QWrs in InGaAs matrix, InAs QWrs in InGaAs matrix, and InAs QWrs in InAlAs matrix on InP substrates.

Chapter 5

Self-Assembled InAs Quantum Wire Lasers

5.1 Introduction

Due to the one dimensional property, the density of states (DOS) of QWrs has spike-like shape[85], and this unique spike-like DOS provides QWr laser diodes the following advantages: low threshold current, higher characteristic temperature, and wider modulation bandwidth[2]. In this chapter, the utilization of these self-assembled InAs QWrs in InGaAs matrix on InP substrate as the active region for the application of the lasers was demonstrated. The wavelength of the lasers is around about 1.6~1.8 μm. In this wavelength range, the light can be applied to medical care, gas spectroscopy, laser radar through atmospheric transmission windows, and optical communications through low-loss fluoride fibers[44].

Because the carriers in QWrs are confined in two dimensions, the polarization dependence behavior of QWr light emission is obvious[86,87]. The polarization dependence PL (PPL) results show the polarization dependence. The PL intensity with electric field parallel to the wires is larger than the PL intensity with electric field perpendicular to the wires.

Due to that InAs QWrs are elongated along $[1\bar{1}0]$ direction, two laser resonant cavity orientations, along $[110]$ direction and $[1\bar{1}0]$ direction, were both fabricated to investigate the QWr orientation influence on laser behaviors. The laser behaviors of lasing spectra and L-I curves with two different cavity orientations are studied. Based on our experimental

results, the dependence on the cavity orientation relative to the wire orientation can be clearly observed from these lasing spectra and L-I curves. Moreover, from the lasing spectra results, the laser diodes with the cavity perpendicular to QWrs showed the ground state lasing to the excited lasing transition behavior at certain temperature range. Simultaneous two-state lasing has also been observed in this temperature range.

We defined resonant cavity along $[1\bar{1}0]$ direction as parallel to QWrs, and defined resonant cavity along $[110]$ direction as perpendicular to QWrs. For the simple description purpose, we write "parallel to QWrs" as "// QWrs" and "perpendicular to QWrs" as "⊥ QWrs" in the following sections in this chapter.

5.2 Theories of Quantum Wires

The 1-D structure has fascinating polarization optical characteristics. The polarization behavior is due to that the carriers in QWrs are confined in two dimensions and are free in only one dimension. Thus, the band structures in QWrs will tell us the polarization behaviors. Many reports of the band structures of QWrs were reported[86,87,88]. In this section, we deal with an ideal rectangular QWrs. The optical behaviors of the interband transition are analyzed from the electron and hole states in a rectangular wire surrounded by an infinite barrier, as shown in Fig.5.1. This figure is the sketch of a rectangular QWr which is quantum confined in x and z direction and is free in y direction. Here, we suppose that the conduction band and the valence band are decoupled and the split-off band can be neglected[89]. Thus, the electron states in conduction band can be obtained directly, and the hole states in the valence band is dealt with the 4×4 Luttinger-Kohn model Hamiltonian.

The electron eigen wave function, $\psi_{\sigma,k}^{(m,n)}(\vec{r})$, and its eigen-energy, $E_c^{(m,n)}(k)$, in the conduction band are:

$$\psi_{\sigma,k}^{(m,n)}(\vec{r}) = \frac{2}{\sqrt{L_x L_z}} \sin\left(\frac{\pi m x}{L_x}\right) \sin\left(\frac{\pi n z}{L_z}\right) \exp(-iky) u_\sigma^c \quad \text{……(Eq.5.1)}$$

$$E_c^{(m,n)}(k) = \frac{\hbar^2}{2m_e^*} \left\{ \left(\frac{\pi \cdot m}{L_x}\right)^2 + \left(\frac{\pi \cdot n}{L_z}\right)^2 + k^2 \right\} \quad \text{……(Eq.5.2)}$$

where L_z is the height of the wire, L_x is the width of the wire, k is the wave vector, m_e^* is the effective mass of electrons, $\hbar$ is the Planck constant over 2π, m and n are the quantum numbers, and u_σ^c is the spin state ($\sigma = \pm ½$). The spin state is expressed as:

$$u_{+½}^c = i\left|s\uparrow\right\rangle \quad \text{……(Eq.5.3(a))}$$

$$u_{-½}^c = i\left|s\downarrow\right\rangle \quad \text{……(Eq.5.3(b))}$$

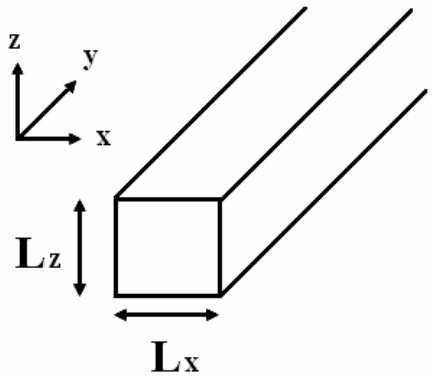

Fig.5.1: The rectangular quantum wire

For the valence band, the heavy hole and light hole band are bases. The Bloch functions of these bases are:

$$u^{v}_{+3/2} = \frac{1}{\sqrt{2}}\left|(x+iy)\uparrow\right\rangle \ldots\ldots \text{(Eq.5.4(a))}$$

$$u^{v}_{+1/2} = \frac{1}{\sqrt{6}}\left|(x+iy)\downarrow\right\rangle - \sqrt{\frac{2}{3}}\left|z\uparrow\right\rangle \ldots\ldots \text{(Eq.5.4(b))}$$

$$u^{v}_{-1/2} = -\frac{1}{\sqrt{6}}\left|(x-iy)\uparrow\right\rangle - \sqrt{\frac{2}{3}}\left|z\downarrow\right\rangle \ldots\ldots \text{(Eq.5.4(c))}$$

$$u^{v}_{-3/2} = -\frac{1}{\sqrt{2}}\left|(x-iy)\downarrow\right\rangle \ldots\ldots \text{(Eq.5.4(d))}$$

Thus, the hole eigen wave function, $\psi^{l}_{k}(\vec{r})$, in the valence band can be expressed as:

$$\psi^{l}_{k}(\vec{r}) = \frac{2}{\sqrt{L_x L_z}} \sum_{mn} \sum_{j} J^{lmn}_{jk} \sin(\frac{\pi m x}{L_x}) \sin(\frac{\pi n z}{L_z}) \exp(-iky) u^{v}_{j} \ \ldots\ldots \text{(Eq.5.5)}$$

where k is the wave vector, m and n are the quantized number, j is the index of the bases, and J^{lmn}_{jk} is the coefficient. The Hamiltonian of the valence band is:

$$H^{v} = \begin{bmatrix} H_{hh} & c & b & 0 \\ c^{+} & H_{lh} & 0 & -b \\ b^{+} & 0 & H_{lh} & c \\ 0 & -b^{+} & c^{+} & H_{hh} \end{bmatrix} \begin{bmatrix} +\frac{3}{2} \\ -\frac{1}{2} \\ +\frac{1}{2} \\ -\frac{3}{2} \end{bmatrix} \ldots\ldots \text{(Eq.5.6)}$$

where b, c, H_{hh}, and H_{lh} are defined as:

$$b = \frac{\sqrt{3}\hbar^2}{2m_0}\left(\partial_x + k_y\right)\left(\gamma_3 \partial_z + \partial_z \gamma_3\right) \ldots\ldots \text{(Eq.5.7(a))}$$

$$c = -\frac{\sqrt{3}\hbar^2}{2m_0}\left(\frac{\gamma_2 + \gamma_3}{2}\right)\left(\partial_x + k_y\right)^2 \ldots\ldots \text{(Eq.5.7(b))}$$

$$H_{hh} = \frac{\hbar^2}{m_0}\left[(\gamma_1 + \gamma_2)\left(\partial_x^2 - k_y^2\right) + \partial_z(\gamma_1 - 2\gamma_2)\partial_z\right] \ldots\ldots \text{(Eq.5.7(c))}$$

$$H_{lh} = \frac{\hbar^2}{m_0}\left[(\gamma_1 - \gamma_2)\left(\partial_x^2 - k_y^2\right) + \partial_z(\gamma_1 + 2\gamma_2)\partial_z\right] \ldots\ldots \text{(Eq.5.7(d))}$$

where m_0 is the electron rest mass, and γ_1, γ_2, γ_3 are Luttinger parameters. Now, the hole eigen wave function, $\psi_k^l(\vec{r})$, in the valence band and its eigen-energy, $E_v^l(K)$, can be solved by:

$$[H^v - E_v^l(k)]\psi_k^l(\vec{r}) = 0 \quad \text{……(Eq.5.8)}$$

From the above equations, the energy of the transition between the conduction band and the valence band is:

$$E_{c,v}^{l-(m,n)}(k) = E_c^{m,n}(k) - E_v^l(k) + E_{gap} \quad \text{……(Eq.5.9)}$$

where E_{gap} is the bandgap. Furthermore, as we obtain the electron eigen wave function, $\psi_{\sigma,k}^{(m,n)}(\vec{r})$, in the conduction band and the hole eigen wave function, $\psi_k^l(\vec{r})$, in the valence band, the optical transition rate can be obtained by the Fermi Golden rule. The transition matrix element is:

$$\left\langle \psi_{\sigma,k}^{(m,n)} \middle| \vec{\varepsilon} \cdot \vec{p} \middle| \psi_k^l \right\rangle = \sum_j J_{jk}^{lmn} \left\langle u_\sigma^c \middle| \vec{\varepsilon} \cdot \vec{p} \middle| u_j^v \right\rangle \quad \text{……(Eq.5.10)}$$

where $\vec{\varepsilon}$ is the polarization vector of the light, and $\vec{p}$ is the momentum operator. Thus, the transition rate is proportion to:

$$\left| M_k^{l-(m,n)} \right|^2 = \sum_\sigma \left| \left\langle \psi_{\sigma,k}^{(m,n)} \middle| \vec{\varepsilon} \cdot \vec{p} \middle| \psi_k^l \right\rangle \right|^2 = K_k^{l-(m,n)} \left| \left\langle c \middle| \vec{p} \middle| v \right\rangle \right|^2 \quad \text{……(Eq.5.11)}$$

where the value of $K_k^{l-(m,n)}$ is expressed as:

$$K_k^{l-(m,n)} = \frac{1}{2}\left(\left| J_{3/2,k}^{lmn} \right|^2 + \left| J_{-3/2,k}^{lmn} \right|^2 \right) + \frac{1}{6}\left(\left| J_{1/2,k}^{lmn} \right|^2 + \left| J_{-1/2,k}^{lmn} \right|^2 \right) + \frac{1}{\sqrt{3}}\left(J_{3/2,k}^{lmn} J_{-1/2,k}^{lmn} + J_{1/2,k}^{lmn} J_{-3/2,k}^{lmn} \right) \quad , \quad when \quad \vec{\varepsilon} \,//\, \hat{y} \quad \text{……(Eq.5.12(a))}$$

$$K_k^{l-(m,n)} = \frac{1}{2}\left(\left|J^{lmn}_{3/2,k}\right|^2 + \left|J^{lmn}_{-3/2,k}\right|^2\right) + \frac{1}{6}\left(\left|J^{lmn}_{1/2,k}\right|^2 + \left|J^{lmn}_{-1/2,k}\right|^2\right) - \frac{1}{\sqrt{3}}\left(J^{lmn}_{3/2,k}J^{lmn}_{-1/2,k} + J^{lmn}_{1/2,k}J^{lmn}_{-3/2,k}\right) \quad , \quad when \quad \vec{\varepsilon} // \hat{x} \qquad \text{……(Eq.5.12(b))}$$

In Eq.5.11, $\langle c|\vec{p}|v\rangle$ is the momentum matrix element of a bulk semiconductor. From the third term of the expression in Eq.5.12(a) and (b), we can find that the value of $K_k^{l-(m,n)}$ depends on the polarization direction of the light, i.e. the electrical field orientation of the light. As a result, the polarization of the optical absorption and the emission of the QWrs have dependence on the orientation of QWrs.

5.3 The Epitaxy Structure and Processes of Quantum Wire Laser Diodes

Fig.5.2 shows the epitaxy structure of the InAs QWr laser. The laser samples were grown on normally (100) oriented InP substrates. The p-InAlAs and n-InAlAs layers were for the current and optical confinement. The 3 periods of 4 ML InAs were grown with 18 nm InGaAs spacers. Finally, there were 4 ML InAs grown on the top of the epitaxy structure for the AFM measurement.

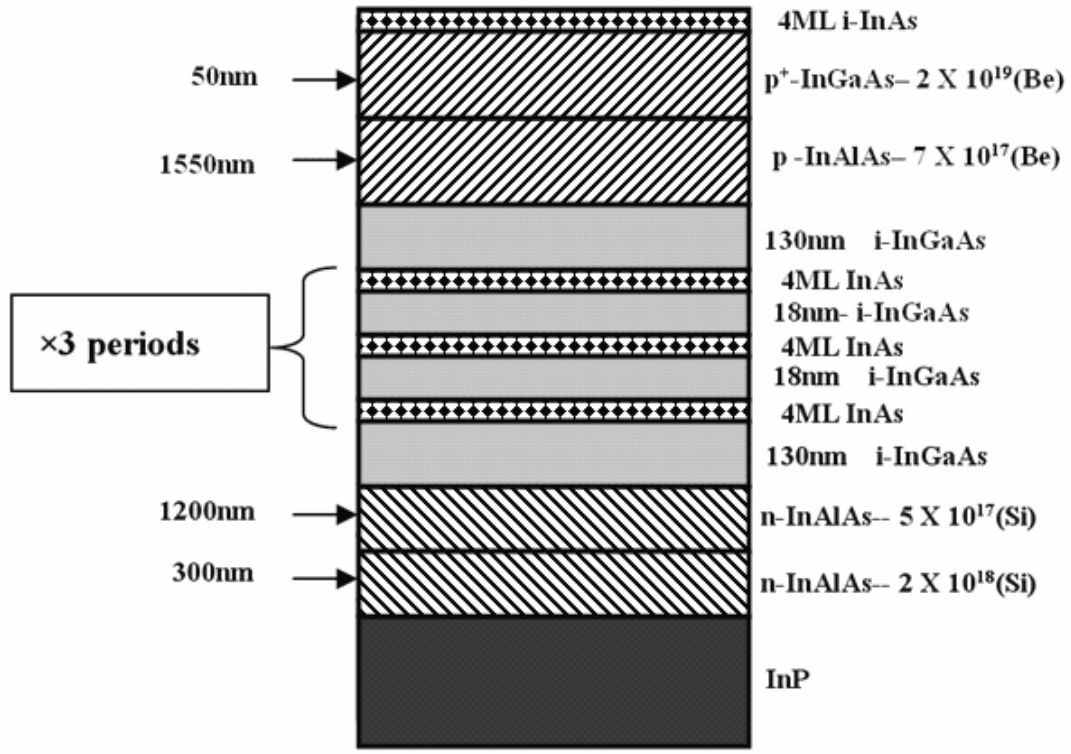

Fig.5.2: The epitaxy structure of the QWr laser

Fig.5.3 presents the sketch of the process flow. The processes detail can be referred to Chapter 2.4. The laser diode structure was the mesa-stripe type, with a stripe width of 20 μm, obtained by wet chemical etching. The etching stopped at 200nm above the active layer. For the p-side down TO can package, a Si_3N_4 thin film was needed as the current blocking layer. After finishing the process, the samples were cleaved to form the laser cavities. The cavity length was 1㎜. Finally, all the laser diodes were sent to Industrial Technology Research Institute for TO can package.

In order to investigate the QWr polarization dependence effects, two sets of laser diodes were fabricated with different cavity orientations. One was // QWrs, while the another was ⊥ QWrs.

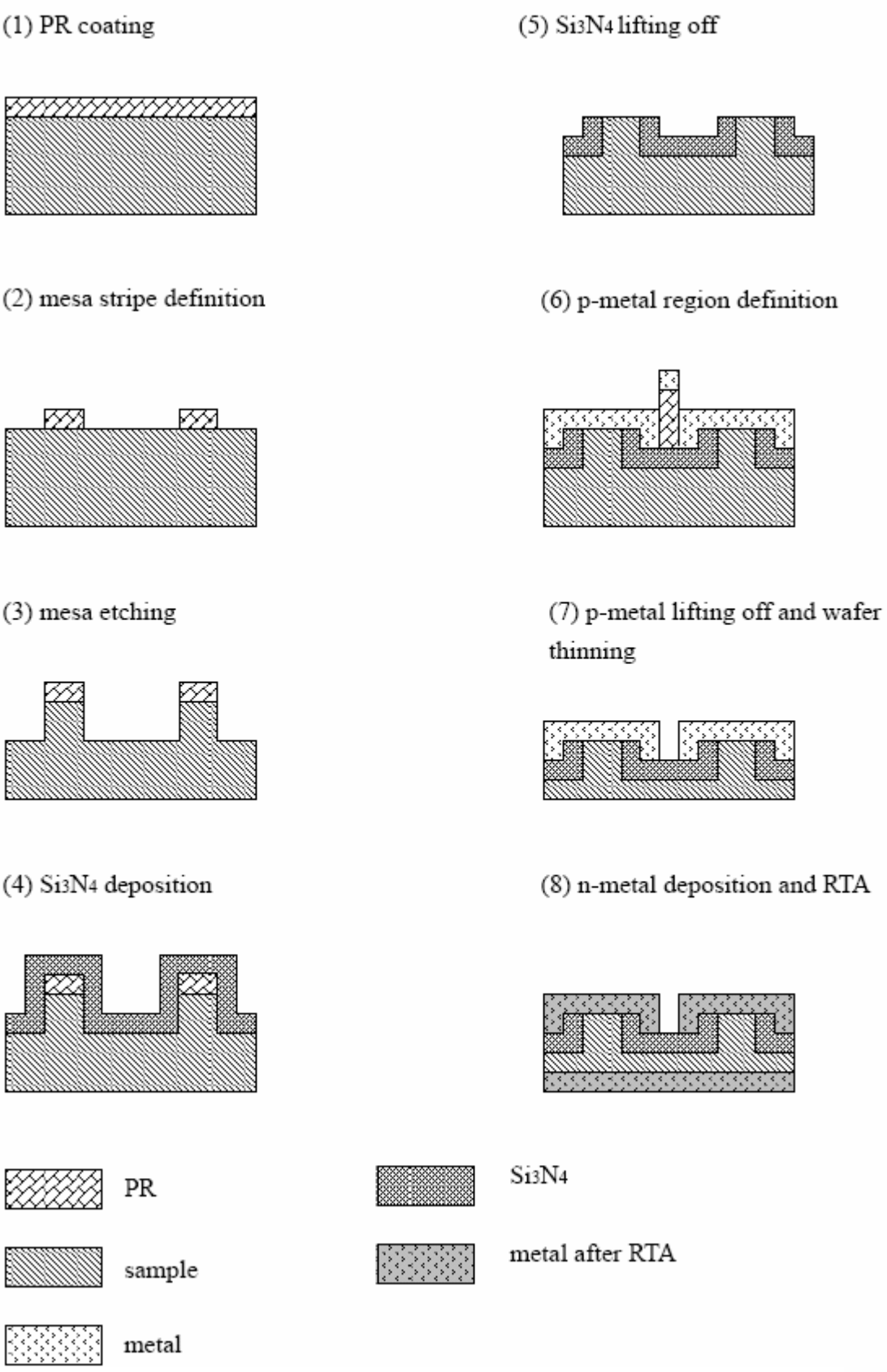

Fig.5.3: The process flow of QWr laser diodes

5.4 Polarization Dependent Photoluminescence

Because the carriers in QWrs are only free in one dimension, the QWr PL should have polarization dependence. By the polarization dependence PL (PPL) measurement system, depicted in Chapter 2.3.3, the quantity of PPL, polarity, is obtained. Here, the polarity is defined as:

$$\frac{P_{//} - P_{\perp}}{P_{//} + P_{\perp}} \quad \text{……(Eq.5.13)}$$

where $P_{//}$ is the PL intensity with polarization // QWrs, and $P_{\perp}$ is the PL intensity with polarization $\perp$ QWrs.

The measurement was carried out from 20k to 240K. The results are shown in Fig.5.4. The InAs QWr PL signal is the longer wavelength peak, and the InGaAs PL signal is the shorter one. The InGaAs PL signal has no polarization dependence while the InAs QWr signal has obvious polarization dependence. The PL intensity of the polarization // QWrs is stronger than that of the polarization $\perp$ QWrs. The PPL behaviors, parallel and perpendicular to the QWrs, agree with polarization preference of the optical transitions in 1-D quantum structures[89]. The plots in Fig.5.4, moreover, show an interesting phenomenon. As temperature increases, the intensity of the InGaAs PL signal increases. When the temperature reaches 240K, the intensity of the InGaAs PPL signal and of the InAs QWr PPL signal are the same. This means that the carriers become harder to be confined in the InAs QWrs with increasing temperature.

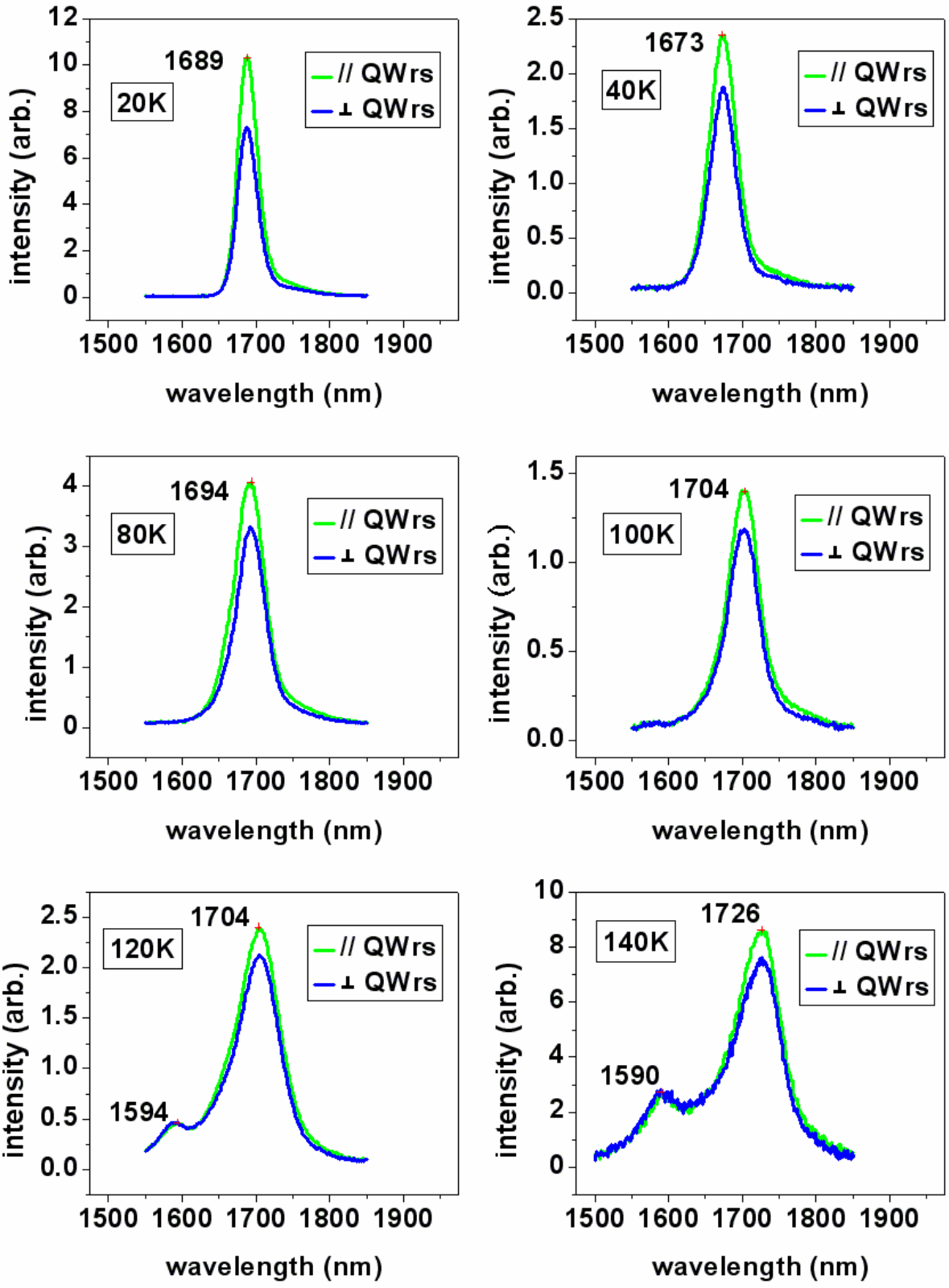

Fig.5.4: PPL results: (a)20K. (b)40K. (c)80K. (d)100K. (e)120K. (f)140K.

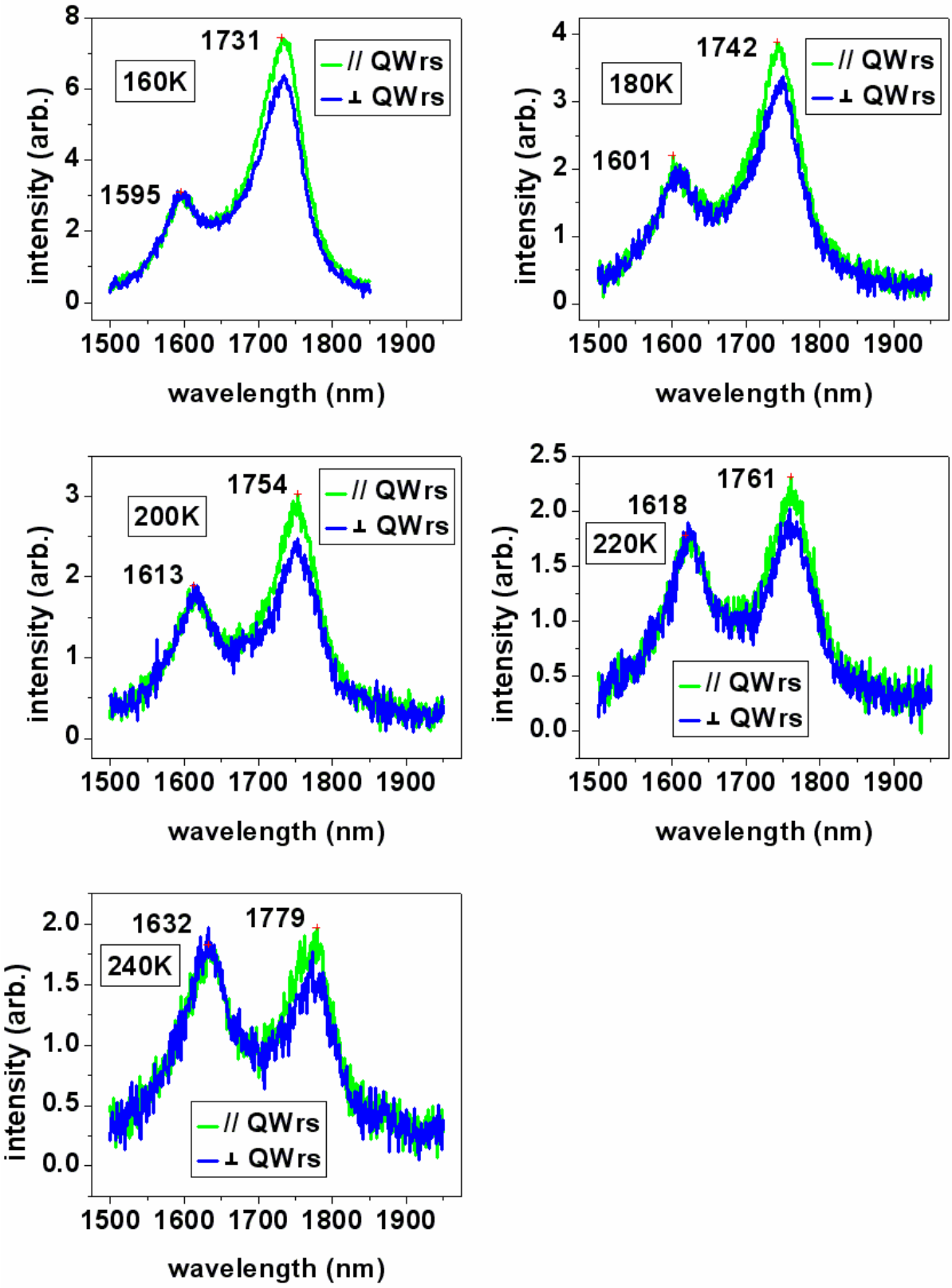

Fig.5.4: PPL results: (g)160K. (h)180K. (i)200K. (j)220K. (k)240K.

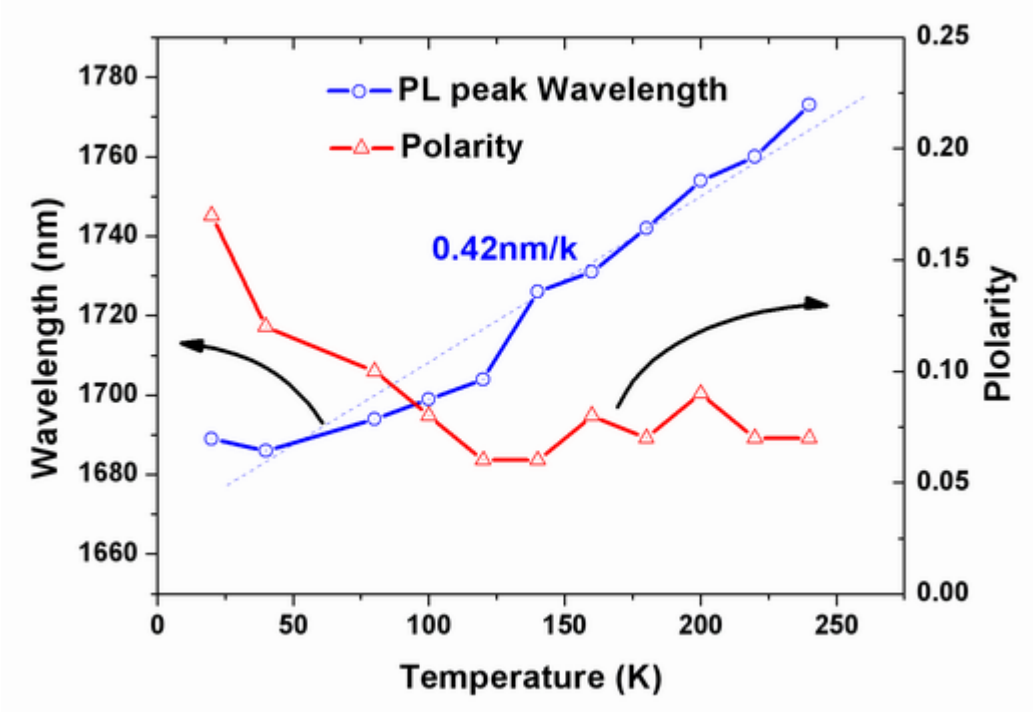

Fig.5.5: The PL peak wavelength and the polarity at different temperatures of the InAs QWrs

In addition to orientation effects, the temperature dependence is studied as well. The polarity and the InAs QWr PL peak wavelength under different temperature are shown in Fig.5.5. The PL peak wavelength linearly increases with raising the measurement temperature. The ramping rate of the PL peak wavelength vs. the temperature is about 0.42nm/K. This is because that the InAs QWr bandgap shrinks with raising the temperature. From this figure, we found that polarity decreases with increasing temperature. The behavior of significant polarity decrease with increasing temperature may be due to the QWr size inhomogeneity. Some QWrs are thick and some are thin. The thick wires have deep quantized states while the thin wires have shallow quantized states. Thus, in low temperature, most carriers stay in the deep states, i.e. in the thicker wires. With increasing temperature, more and more carriers stay in the shallow states, i.e. in the thin wires. Previous reports have shown that the thick QWrs have larger polarity than the thin QWrs have [90,91]. As a result, the polarity decreases with increasing temperature.

5.5 Lasing Spectra

When we measured the InAs QWr lasing spectra under different temperature, we observed interesting lasing spectrum behaviors for the laser diodes with the cavity ⊥ QWrs at 140~160K. One interesting phenomenon between 140K and 160K is the abrupt decrease of lasing wavelength. Fig.5.6 shows the lasing wavelength at the threshold condition vs. the temperature for the laser cavity ⊥ QWrs. The lasing wavelength decreases from 1735nm at 140K to 1676nm at 160K. In this section, we will try to investigate the details of the lasing spectra in this interesting temperature range and divide the discussion into two subsections: temperature between 20K and 120K, and temperature between 140K and 200K.

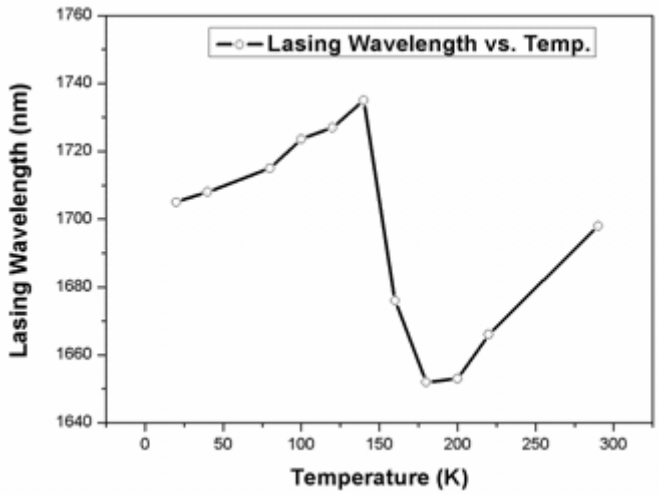

Fig.5.6: Lasing wavelength vs. temp. for QWr lasers with the cavity ⊥ QWrs

5.5.1 Lasing Spectra between 20K and 120K

Fig.5.7 shows the PL results and the lasing spectra of two cavity orientations. In these figures, we find out that the lasing wavelength of the cavity ⊥ QWrs is always longer than that of the cavity // QWrs. The wavelength spacing is about 60~130nm. This means that the

polarization dependence of QWrs has strong influence on the lasing spectra of QWr laser diodes. Comparing with the PL spectra, the laser diode with its cavity // QWrs is the excited state lasing, and the laser diode with its cavity ⊥ QWrs is the ground state lasing.

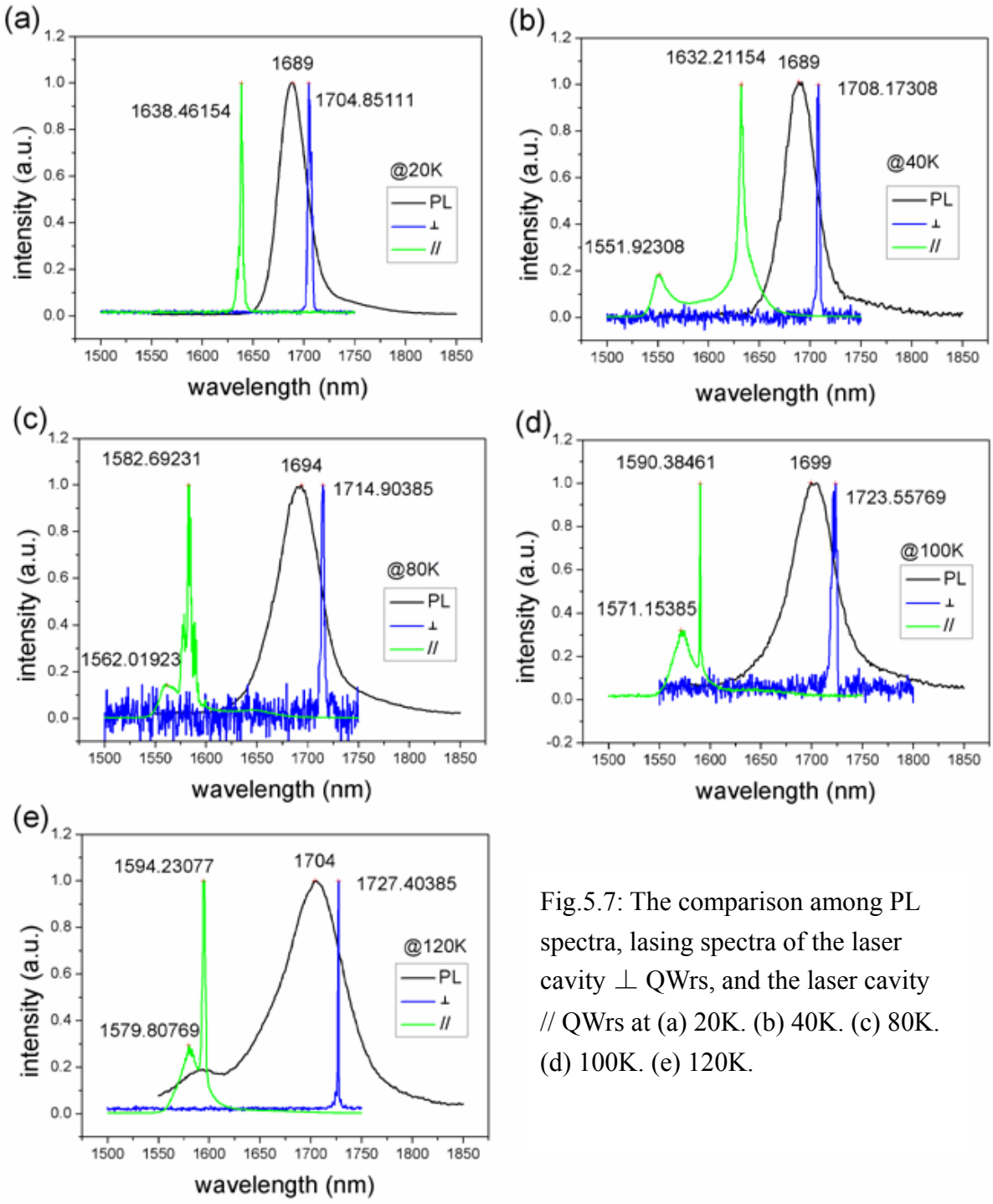

Fig.5.7: The comparison among PL spectra, lasing spectra of the laser cavity ⊥ QWrs, and the laser cavity // QWrs at (a) 20K. (b) 40K. (c) 80K. (d) 100K. (e) 120K.

In this temperature range, the lasing wavelength of the laser diode with the cavity ⊥

QWrs increases with raising the operation temperature. This is because the material bandgap shrinks with increasing the temperature. The ramping rate of the lasing wavelength vs. the temperature is about 0.23nm/K.

The wavelength of the ground state lasing of the laser diode with its cavity ⊥ QWrs is longer than that of PL peak. This is due to that the cryostat mounts for PL samples and for laser diodes are different. The PL samples are attached to the copper mount at the end of the cryostat refrigerator head with thermal grease directly. However, the laser diodes are mounted on the acrylic board and then the acrylic board is fastened on the copper mount at the end of the cryostat refrigerator head by screws. The mount method for PL samples is to obtain good thermal conductivity between the PL samples and the refrigerator head, whereas the mount method for laser diodes is to avoid the electrical conductivity between laser diode and the refrigerator head. As a result, the thermal conductivity of the cryostat mount for laser diodes is bad, and the real operation temperature of laser diodes is much higher than the reading of the temperature controller of the cryostat. Therefore, the wavelength of the ground state lasing of the laser diode with its cavity ⊥ QWrs is longer than that of PL peak.

5.5.2 Lasing Spectra between 140K and 200K

In order to explore the fascinating behaviors of the abrupt decrease of lasing wavelength at threshold condition shown in Fig.5.6, a careful investigation of the lasing spectra between 140K and 200K was carried out. Fig.5.8, Fig.5.9, Fig.5.10, and Fig.5.11 were the lasing spectra at different injected currents under 140K, 160K, 180K, and 200K respectively for laser diodes with the cavity ⊥ QWrs. These lasing spectrum behaviors between 140K and 200K are described first, and are discussed finally in the following paragraphs.

At 140K, the lasing wavelength peak at the threshold condition is at 1735nm. With

increasing the injected current to $2.6I_{th}$, a shorter lasing wavelength peak at 1696nm starts to emerge, cf. Fig.5.8(a). Comparing with PPL results in Fig.5.4, the long lasing wavelength peak is the ground state lasing, and the short lasing wavelength peak is the excited state lasing. As the injected current is continuously increased, the intensity of the shorter lasing peak increases, cf. Fig.5.8(b) and (c). When the injected current is increased to $I=6I_{th}$, the intensity of 1695nm wavelength peak is much larger than that of 1735nm wavelength peak.

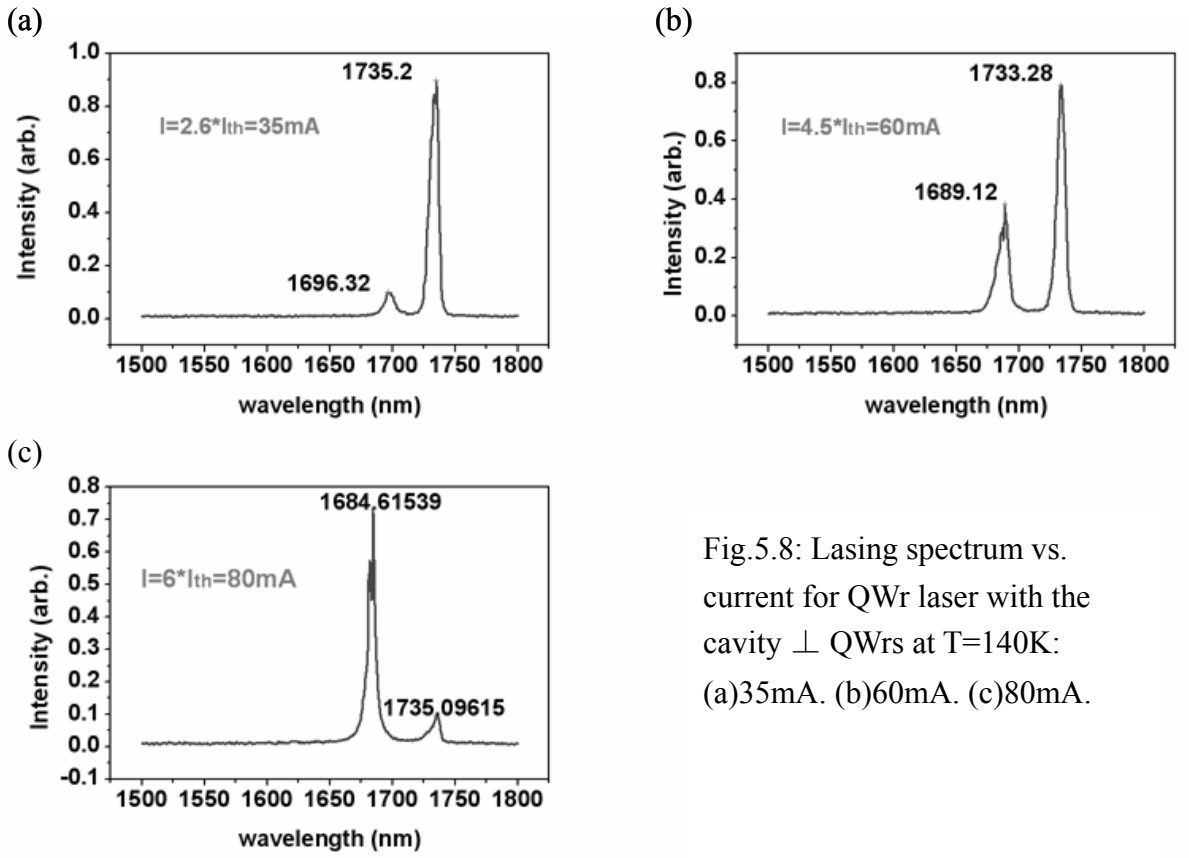

Fig.5.8: Lasing spectrum vs. current for QWr laser with the cavity ⊥ QWrs at T=140K: (a)35mA. (b)60mA. (c)80mA.

At 160K, the peak gain of excited state takes over to meet the threshold condition and the excited state lases at threshold condition, cf. Fig.5.9(a). The lasing wavelength is 1676nm. In Fig.5.9(b), as the injection current is increased to 100mA , a signal at 1741nm emerges. This signal should be from the ground state emission. When the injection current reaches

230mA, both the ground state and the excited state lase at the same time.

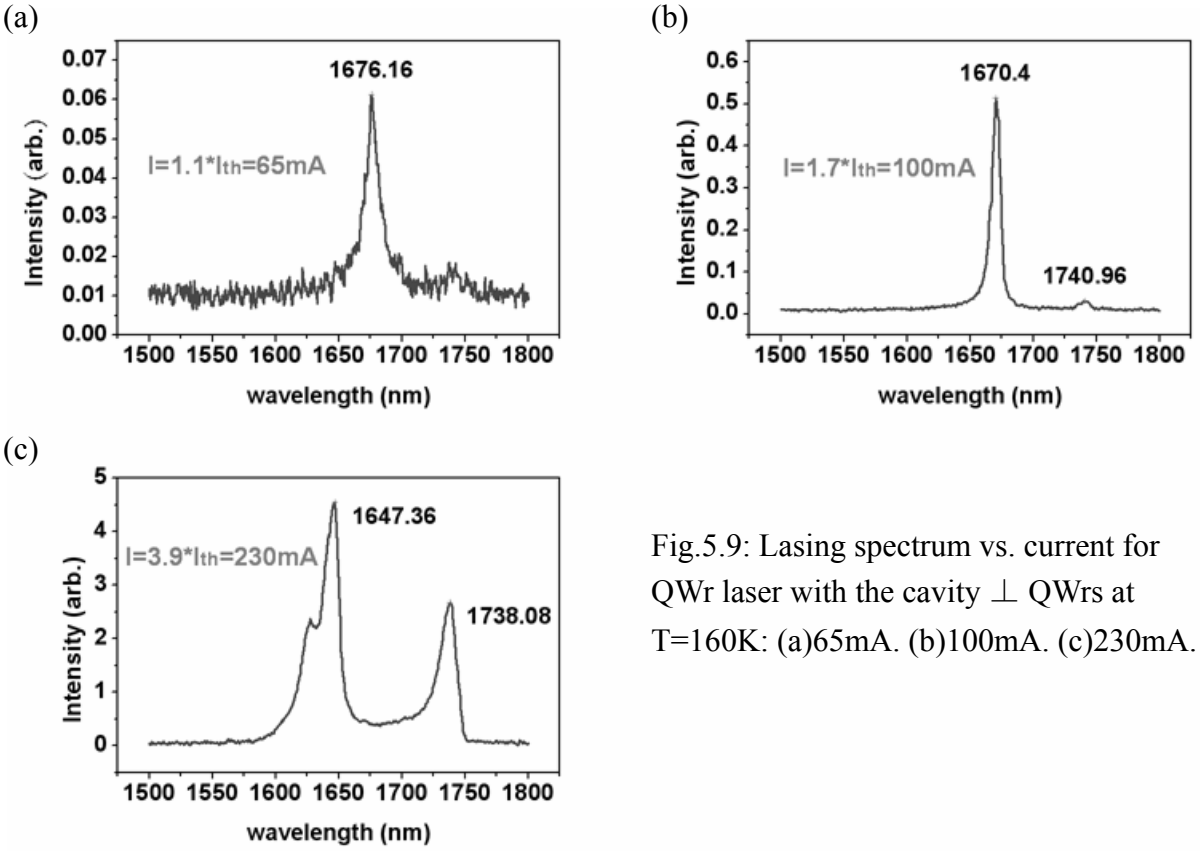

Fig.5.9: Lasing spectrum vs. current for QWr laser with the cavity ⊥ QWrs at T=160K: (a)65mA. (b)100mA. (c)230mA.

At 180K, excited state lasing at 1645nm is observed just above the threshold condition, cf. Fig.5.10(a). As the injected current is increased to 2.4 I_{th}, cf. Fig.5.10(c), the 1743nm signal emerges. This little signal is the emission from the ground state.

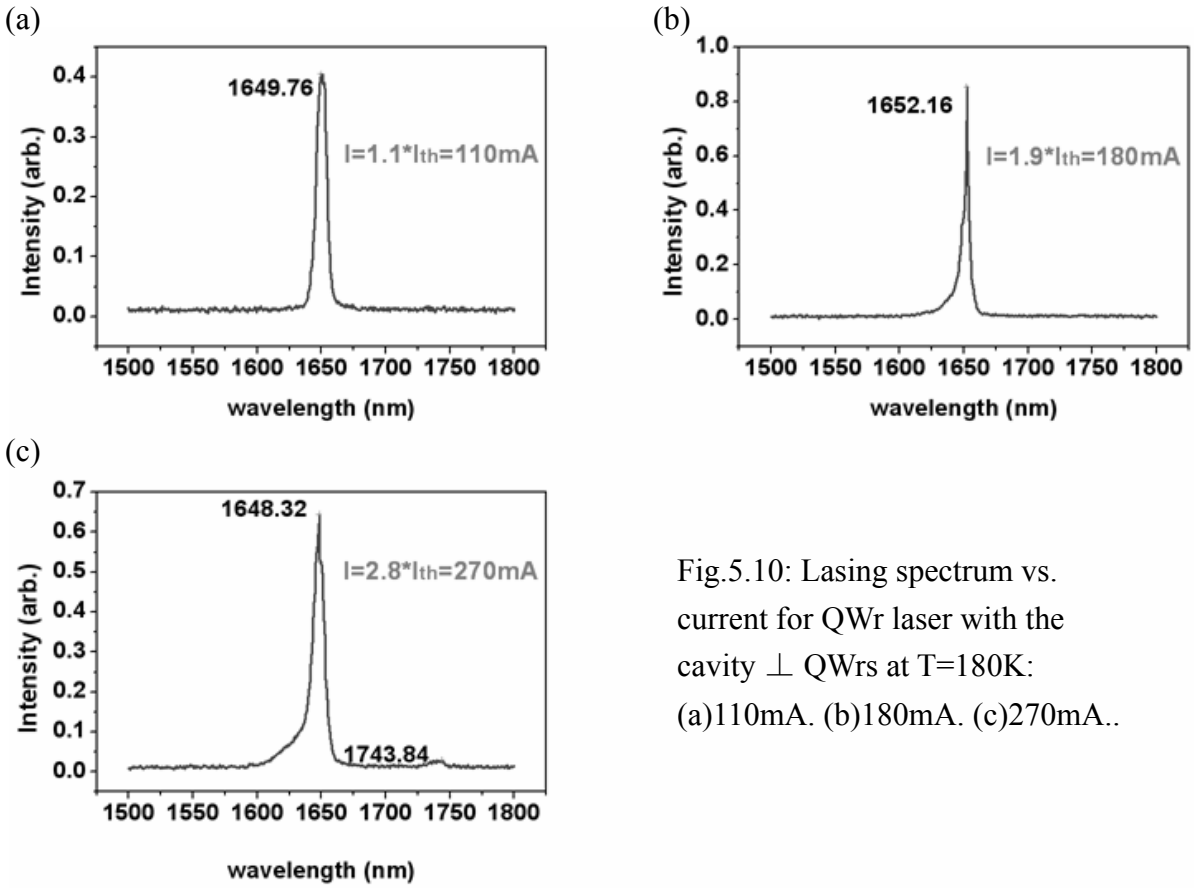

Fig.5.10: Lasing spectrum vs. current for QWr laser with the cavity ⊥ QWrs at T=180K: (a)110mA. (b)180mA. (c)270mA..

At 200K, only the signal with wavelength about 1655nm is found through our experiment, cf. Fig.5.11. This signal is excited state lasing. The fact that the ground state signal is not observed means that the light emission from the ground state is too weak to be detected even under large injected current.

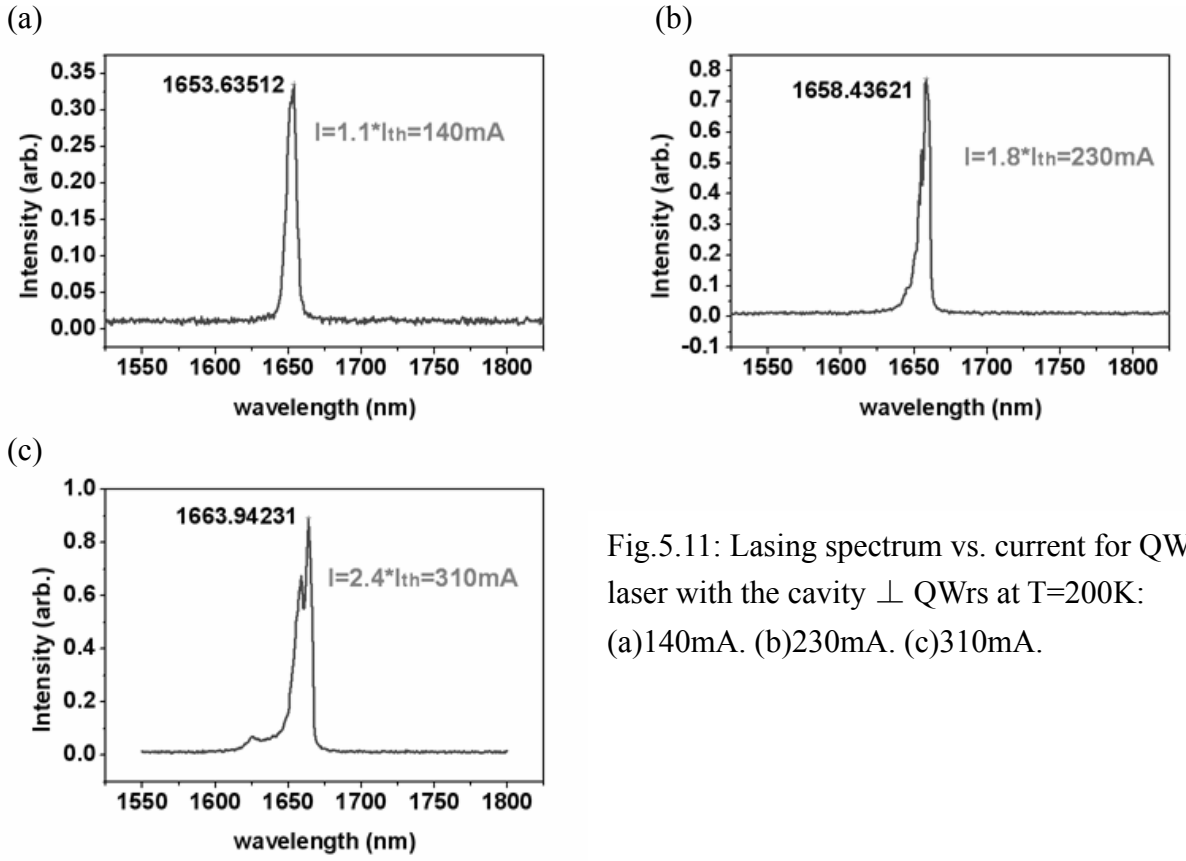

Fig.5.11: Lasing spectrum vs. current for QWr laser with the cavity ⊥ QWrs at T=200K: (a)140mA. (b)230mA. (c)310mA.

In order to elucidate the fascinating lasing spectrum phenomena in the previous content in this section, Fig.5.12 outlines the physical explanation of the QWr lasers behaviors. The threshold gain, g_{th}, the dash line plotted in Fig.5.12 is given by:

$$g_{th} = \alpha_i + \frac{1}{2L} \times \ln(\frac{1}{R_1 R_2}) \quad \text{.....(Eq.5.14)}$$

where L is the laser cavity length, R_1 and R_2 are the reflectivities of the two mirrors of the resonant cavity, and α_i is the internal loss coming from the absorption loss in the diodes and the scattering loss by the rough interfaces or the non-uniform epitaxy layers. $\frac{1}{2L} \times \ln(\frac{1}{R_1 R_2})$ in Eq.5.14 is the mirror loss. Therefore, $\alpha_i + \frac{1}{2L} \times \ln(\frac{1}{R_1 R_2})$ is the total optical loss of a laser diode.

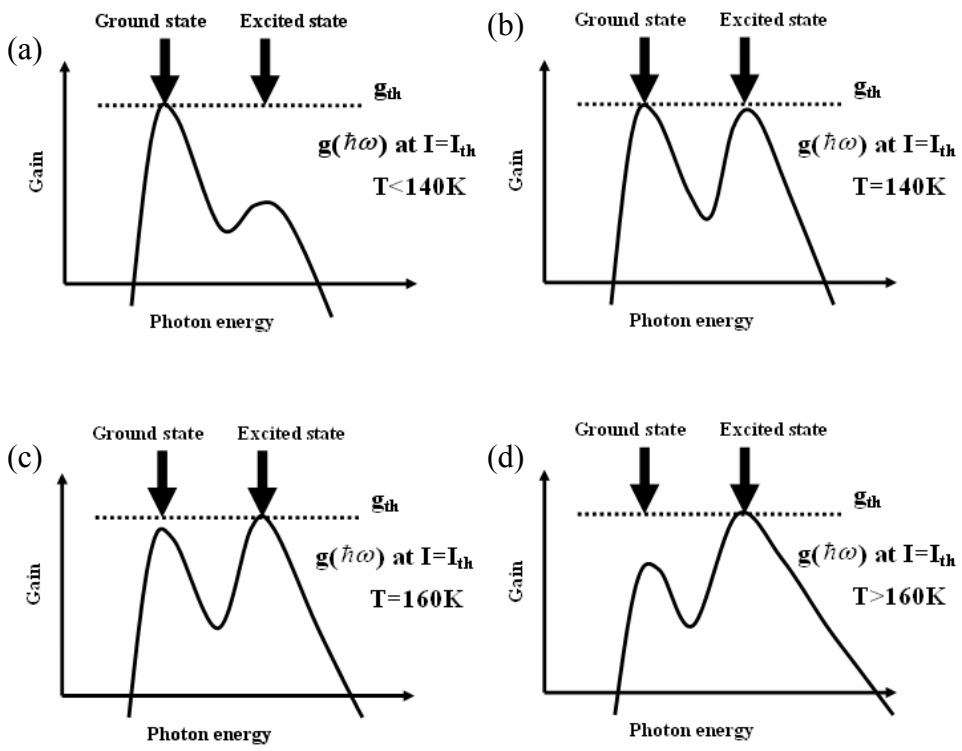

Fig.5.12: Outlines of the explanation for the ground state lasing to the exciting state lasing transition: (a)T<140K.(b)T=140K.(c)T=160K.(d)T>160K.

Fig.5.12 also sketches the optical gain spectrum, $g(\hbar\omega)$, of QWrs at different temperatures. The formula of $g(\hbar\omega)$ contains Fermi-Dirac distribution terms[92]. Due to the temperature factor in the Fermi-Dirac distribution, higher temperature makes the optical gain spectrum be less under same carrier population. When the operation temperature is lower than 140K, the peak gain of the ground state is able to meet the threshold gain with enough injected carriers and InAs QWr laser generates ground state lasing, cf. Fig.5.12(a). As the temperature is increased, more carriers are needed to populate the QWrs to make the peak gain of the ground state to retain the threshold condition. This makes more carriers populate in the excited state. Due to the large degeneracy of the excited state, the carrier population in the excited state increases faster than the ground state. Thus, the peak gain of the excited state intensifies more quickly than that of the ground state. When the temperature is higher than

160K, even the peak gain of the excited state equals to that of ground state, the peak gain of the ground state cannot reach the threshold gain. As a result, the excited state takes over to have a higher gain with increasing injected current and then meet the threshold gain, cf. Fig.5.12(d). Therefore, the InAs QWr laser is excited state lasing at high temperatures.

When the temperature is between 140K and 160K, the peak gain of the ground state is about the same with that of the excited state when the laser diode lases. At 140K, the ground state lasing happens first, and the carrier population in the ground state is clamped. At this moment, the difference between the threshold gain and the peak gain of the excited state is little, cf. Fig.5.12(b). With increasing the injected current, more carriers populate the excited state, and then the peak gain of the excited state meets the threshold condition. As a result, the excited state starts to lase at 140K, too. As the temperature is raised to 160K, the excited state takes over to have a higher gain and lases first, cf. Fig.5.12(c). The carrier population in the excited state is clamped. Now, the peak gain of the ground state is just a little bellow the threshold gain. With continuously increasing the injected current, some carriers are captured in the ground state and finally the peak gain of the ground state meets the threshold gain. Consequently, the ground state also lases at 160K. Therefore, as temperature is between 140K and 160K, we obtain conclusions that two-state lasing happens under larger driving current and the lasing transition from the ground state lasing to the excited state lasing occurs.

5.6 L-I Curves

The L-I curves of InAs QWr laser diodes with different cavity orientations were measured under different temperature. Orientation dependence was observed. The measurement results are shown in Fig.5.13., and shows that the laser diodes with the cavity

⊥ QWrs are easier to lase.

Based on the macroscopic picture, carriers are confined in two dimensions, and are only free to transfer in one direction in the QWrs. When the electrical field of the lasing light in the laser diode is // QWrs, the interaction between the electrical field of the lasing light and the carriers in the QWrs is strong. In contrast, as the electrical field of the lasing light in the laser diode is ⊥ QWrs, the interaction between the electrical field of the lasing light and the carriers in the QWrs is weak. As a result, the laser diodes with the cavity ⊥ QWrs are easier to lase and have much smaller threshold currents as shown in our experiment results, cf. Fig.5.13. Because the laser diodes with the cavity // QWrs did not lase as the temperature was higher than 180K, the L-I curves of two different orientations are only plotted from 20K to 180K.

The L-I curves in Fig.5.13(a) are the results of the laser diodes with the cavity ⊥ QWrs, and the kinks can be observed in the L-I curves operated at 120K, 140K, and 160K in this plot. By the discussion in Chapter 5.5, this behavior is attributed to the two-state lasing. The laser diodes are one state lasing as the injected currents are just above the threshold current in 120K, 140K, and 160K (ground state lasing in 120K and 140K, and excited state lasing in 160K). Thus the L-I curves perform like a straight line. However, with increasing the injected current, another state starts to lase (excite state lasing in 120K and 140K, ground state lasing in 160K). As a result, the kinks are occurred.

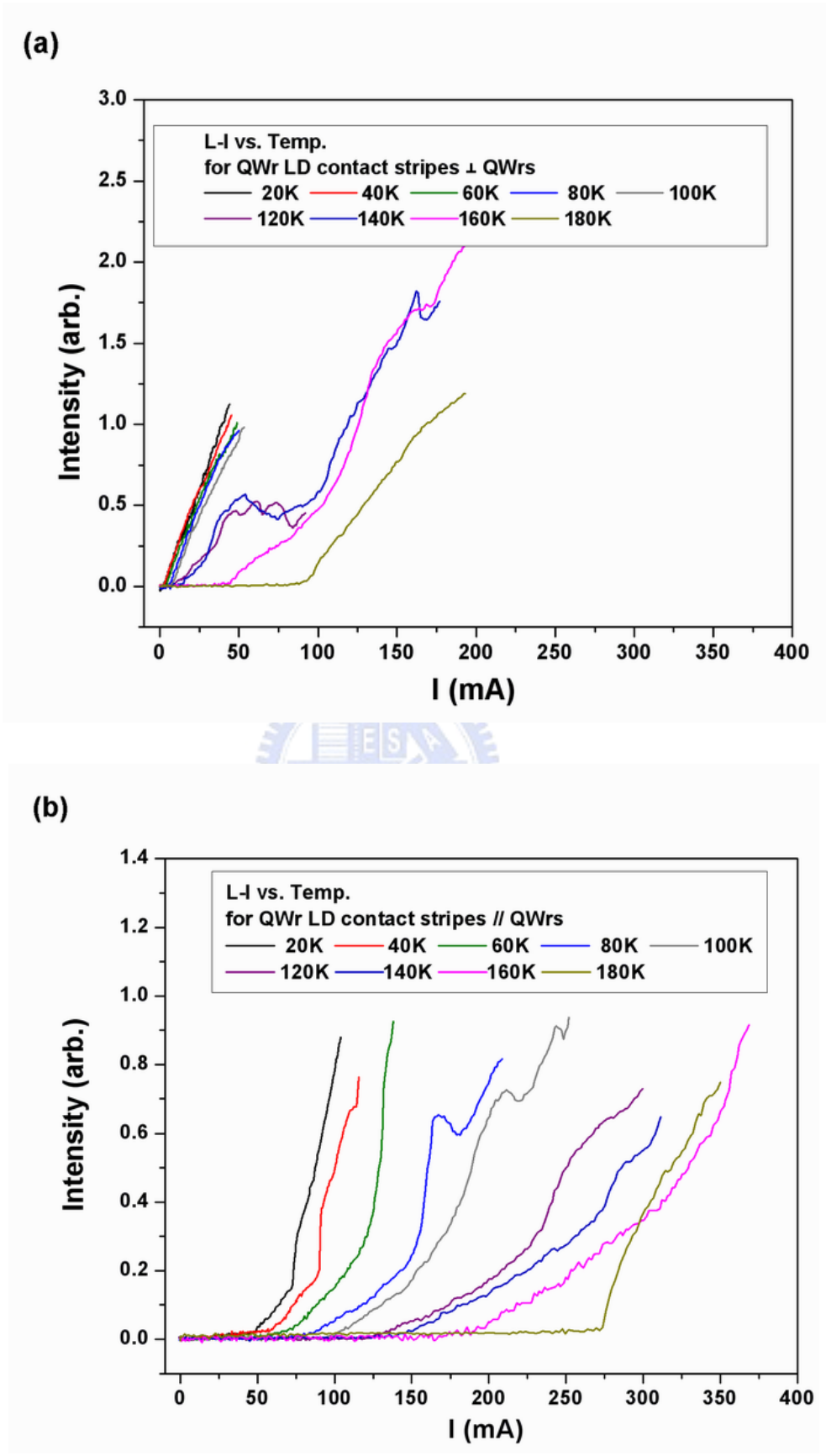

Fig.5.13: L-I curves at different temperatures: (a)the laser cavity ⊥ QWrs. (b)the laser cavity // QWrs.

The characteristic temperature, T_0, is used for estimate of the temperature dependence of laser diodes. It is empirically expressed for the threshold current as:

$$I_{th}(T) = I_{th}(T_i) \times \exp(\frac{T - T_i}{T_0}) \quad \text{……(Eq.5.15)}$$

$I_{th}(T)$ and $I_{th}(T_i)$ are the threshold currents at temperature T and T_i. By plotting the logarithm of $I_{th}(T)$ vs. temperature, the characteristic temperature, T_0, is obtained from the slop in the plot. The threshold current vs. temperature for two cavity orientations are shown in Fig.5.14. For the laser diode cavity // QWrs, the characteristic temperature is 98.3K. However, the characteristic temperature for the cavity $\perp$ QWrs is very interesting between 140K and 180K. The characteristic temperature is 68.9K and 65.4K for the temperature lower than 140K and higher than 180K respectively while the characteristic temperature is only 20.8K between 140K and 180K. The T_0 variation of laser diodes with the cavity $\perp$ QWrs is due to the transition of the ground state lasing to the excited state lasing. When the temperature is lower than 140K, T_0 is the characteristic temperature of the ground state lasing; when the temperature is higher than 160K, T_0 is the characteristic temperature of the excited state lasing. The $I_{th\perp}$ vs. temperature curve between 140K and 180K just meets the transition of the ground state lasing to the excited state lasing. Therefore, T_0 is only 20.8K between 140K and 180K.

In addition to this interesting behaviors, the other fun behavior shows in the threshold currents ratio of these two orientations, $I_{th//}/I_{th\perp}$, under different temperatures, cf. Fig.5.14. We found that when temperature is lower than 140K, the ratio is about 10~20. However, as temperature is raised higher than 140K, the ratio decreases abruptly to 2~5. For the I_{th} ratio of the cavity // QWrs to the cavity $\perp$ QWrs when the temperature is lower than 140K, the threshold current of laser diode with the cavity $\perp$ QWrs is the ground lasing. However, as

temperature is higher than 160K, this threshold condition change from ground state lasing to the excited state lasing. Moreover, the laser diodes with the cavity // QWrs are always the excited state lasing through our experiment. As a result, as temperature is lower than 140K, the I_{th} ratio is about 10~20. However, as temperature is raised higher than 140K, the ratio drops dramatically to 2~5

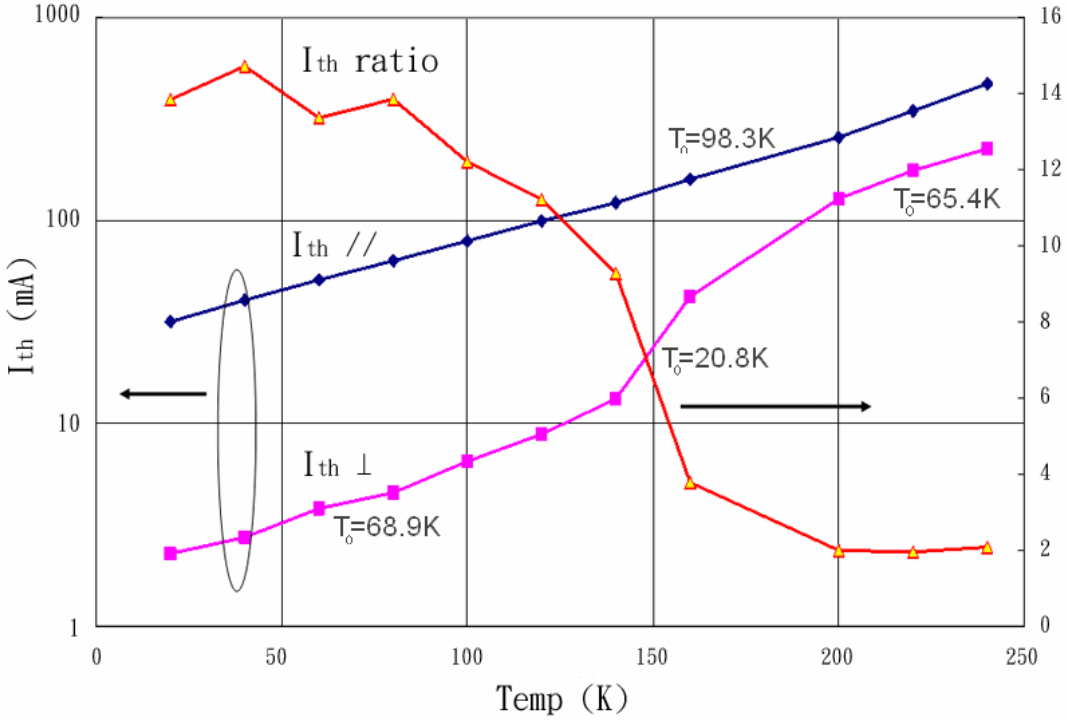

Fig.5.14: I_{th} vs. temp. for the laser cavity // QWrs and for the laser cavity ⊥ QWrs. The I_{th} ratio vs. temp. is also plotted

5.7 Summary

We have successfully demonstrated QWr lasers lasing in the 1.6~1.8 μm range using self-assembled InAs QWrs on InP substrates. PPL results of the QWrs show the apparent

polarization dependence. The PL intensity with the polarization // QWrs is stronger than that with the polarization ⊥ QWrs. Obvious dependence on the laser diode cavity orientation, relative to the QWr orientation, is observed in the lasing behaviors, such as lasing spectra and L-I curves. The difference in lasing behaviors for different lasers orientations, parallel and perpendicular to the QWrs, agrees with polarization preference of the optical transitions in 1-D quantum structures. The transition of the ground lasing to the exciting lasing in about 140K for laser cavity ⊥ QWrs is observed and is used to explain some interesting lasing behaviors successfully. Moreover, simultaneous two-state lasing is observed for the laser cavity ⊥ QWrs between 140~160K.

Chapter 6

Mobility Asymmetry in InGaAs/InAlAs Heterostructures with InAs Quantum Wires

6.1 Introduction

Utilizing the self-assembled method, the deposition material, with its lattice constant different from that of the host material, will form various kinds of quantum structures. InAs QDs grown on GaAs substrates are the most widely studied structures[3]. Other attractive structures were the InAs quantum structures formed on materials latticed matched to InP substrates[32,76,77]. In the presence of such quantum structures such as QDs and QWrs, the electron transport properties should certainly be affected. For examples, QDs, like artificial atoms, act as scattering centers or traps, while QWrs, the one-dimensional quantum structures, should give an orientation dependent transport characteristics. Our laboratory has reported an asymmetric transport behavior in an InGaAs/InAlAs two-dimensional electron channel when GaAs anti-QWrs were embedded nearby[36]. The observation of the asymmetric electrical transport behavior for InAs QWrs embedded in InP bulk material was also reported[57].

The 1 μm long InAs QWrs along $[1\bar{1}0]$ direction can be stably fabricated in InGaAs matrix, lattice matched to InP substrates, in our laboratory. Moreover, the electron mobility in InAs is larger than that in $In_{0.53}Ga_{0.47}As$[93,94]. The influence of InAs QWrs embedded near the InGaAs/InAlAs heterointerface on the electron transport behavior of the 2-D channel attracts our interests. For comparison, an InGaAs/InAlAs heterostructure on InP substrate without QWrs and a GaAs/AlGaAs heterostructure on GaAs substrate with InAs QDs embedded near the heterointerface were investigated.

With self-assembled InAs QWrs embedded nearby the InGaAs/InAlAs heterostructures on InP substrates, the strong electron mobility asymmetry behavior was observed. The electrons prefer to transport along the InAs QWr elongation direction, i.e. $[1\bar{1}0]$ direction. At low temperature, when the InAs QWrs is placed just at the heterostructure, the electron mobility ratio in $[1\bar{1}0]$ direction to $[110]$ direction is the biggest. However, we did not observed the obvious anisotropic carrier transport behavior for the InGaAs/InAlAs heterostructure on InP substrate without InAs QWrs and for the GaAs/AlGaAs heterostructure on GaAs substrate with InAs QDs. The asymmetry in mobility is attributed to the difference in scattering cross-section of the InAs QWrs in these two directions.

6.2 Epitaxy Structures and Hall measurement

The samples with InGaAs/InAlAs heterostructures on InP substrates in this study were grown on normally (100) oriented semi-insulating InP substrates using a Varian Gen II solid source MBE system. Three samples with InGaAs/InAlAs heterostructures were prepared. Their epitaxy structures are shown in Fig.6.1. Except the epitaxy of InAs QWrs, they all had the same epitaxy structure. InGaAs/InAlAs heterostructure, both lattice matched to InP substrates, was grown to form a 2-D electron gas channel. A 40 nm Si-doped InAlAs, with 5E17 cm^{-3} concentration, was epitaxied to supply the carriers to the 2-D channel.

Sample A, without InAs QWrs, was used as a reference. Samples B and C, each had an additional InAs QWrs near or in the 2-D channel, were used for the transport study. The QWrs in samples B and C were formed with 4 ML of InAs. The growth mechanism for the InAs QWrs has been discussed in Chapter.3. The InAs QWrs in Sample B were located 3nm below the InGaAs/InAlAs interface, while in Sample C the InAs QWrs were grown right at the interface.

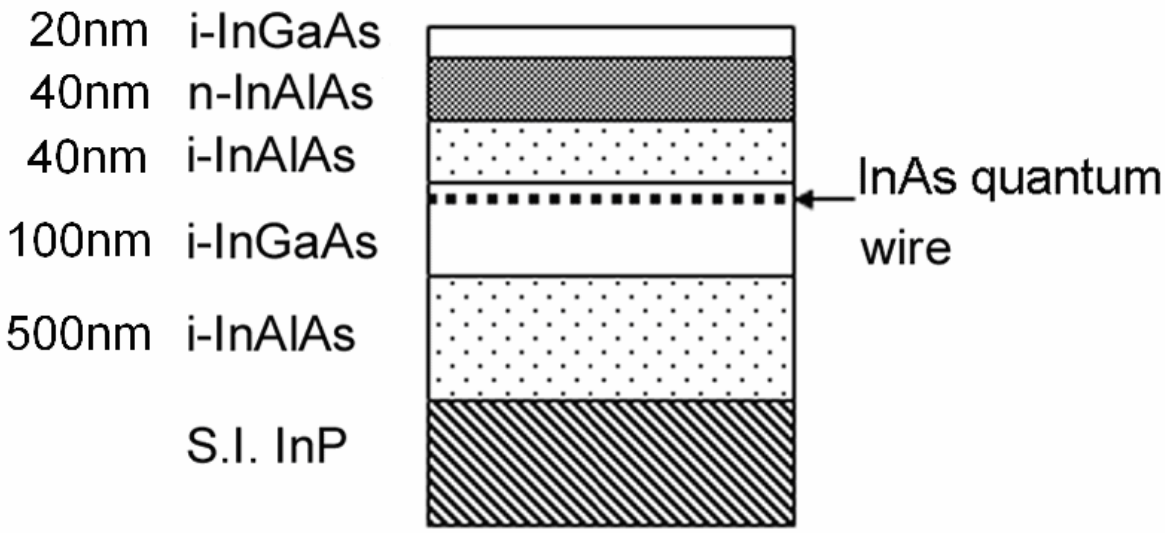

Fig.6.1: The InGaAs/InAlAs heterostructures prepared in this study: Sample A had no InAs QWrs; Sample B had an extra InAs QWrs 3nm below the heterointerface; Sample C had the InAs QWrs right at the interface.

For comparison of the 1-D quantum structure influence with the 0-D quantum structure influence on the 2-D conduction channel, an $Al_{0.3}Ga_{0.7}As$/GaAs heterostructure with InAs QDs grown on the GaAs substrate, Sample D, was also prepared. This sample was grown on the normally (100) oriented semi-insulating GaAs substrate with the same MBE system. The epitaxy structure is shown in Fig.6.2. A 40nm Si-doped $Al_{0.3}Ga_{0.7}As$, with 3E18 cm^{-3} concentration, was used to supply the carriers to the 2-D conduction channel. Additional 2.6ML InAs QDs grown under 520℃ were placed 10nm below the $Al_{0.3}Ga_{0.7}As$/GaAs heterostructure. Finally, InAs QDs with the same growth condition was deposited on the sample surface for AFM measurement.

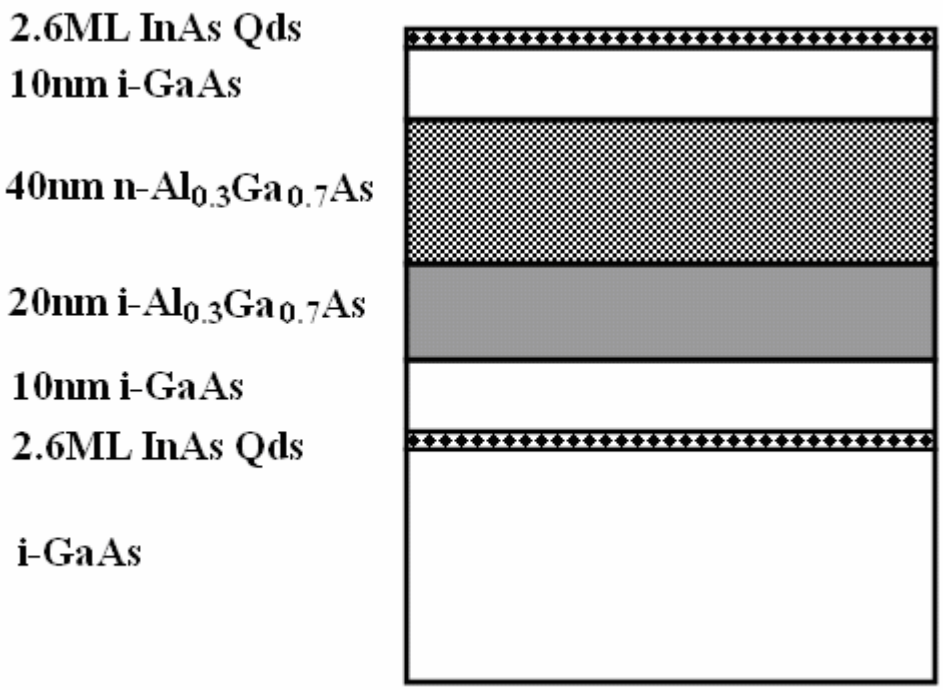

Fig.6.2: The epitaxy structure of Sample D.

After growth, all the samples were sent to High Magnetic Field and Low Temperature Laboratory in National Chung Hsing University for Hall measurement. In order to investigate the dependence of anisotropic electrical transport behavior on the InAs QWr orientation, two sets of 8-contack Hall bars oriented along [110] direction and $[1\bar{1}0]$ direction, were both fabricated on these four samples for Hall measurement. The Hall measurement was carried out from 10K to 300K

6.3 Sheet Carrier Concentration

Fig.6.3 shows the sheet carrier concentration as a function of temperature for Sample A, Sample B, and Sample C. The sheet carrier concentration of Sample D is shown in Fig.6.4. As shown in Fig.6.3, Sample A, Sample B, and Sample C roughly have the same density. There is

small sheet concentration difference between two directions of Sample C. It should be due to the measurement error and the non-uniform epitaxy on the wafer.

The conduction channel of Sample B and Sample C actually consist of a 2-D channel at the InGaAs/InAlAs interface and the InAs QWr layer. The fact that the sheet density does not differ very much for different samples and for different conduction directions indicates that the conduction carriers are mainly due to those in the 2-D channel at the InGaAs/InAlAs interface. Thus, the electrons in the InAs QWrs play only a minor role.

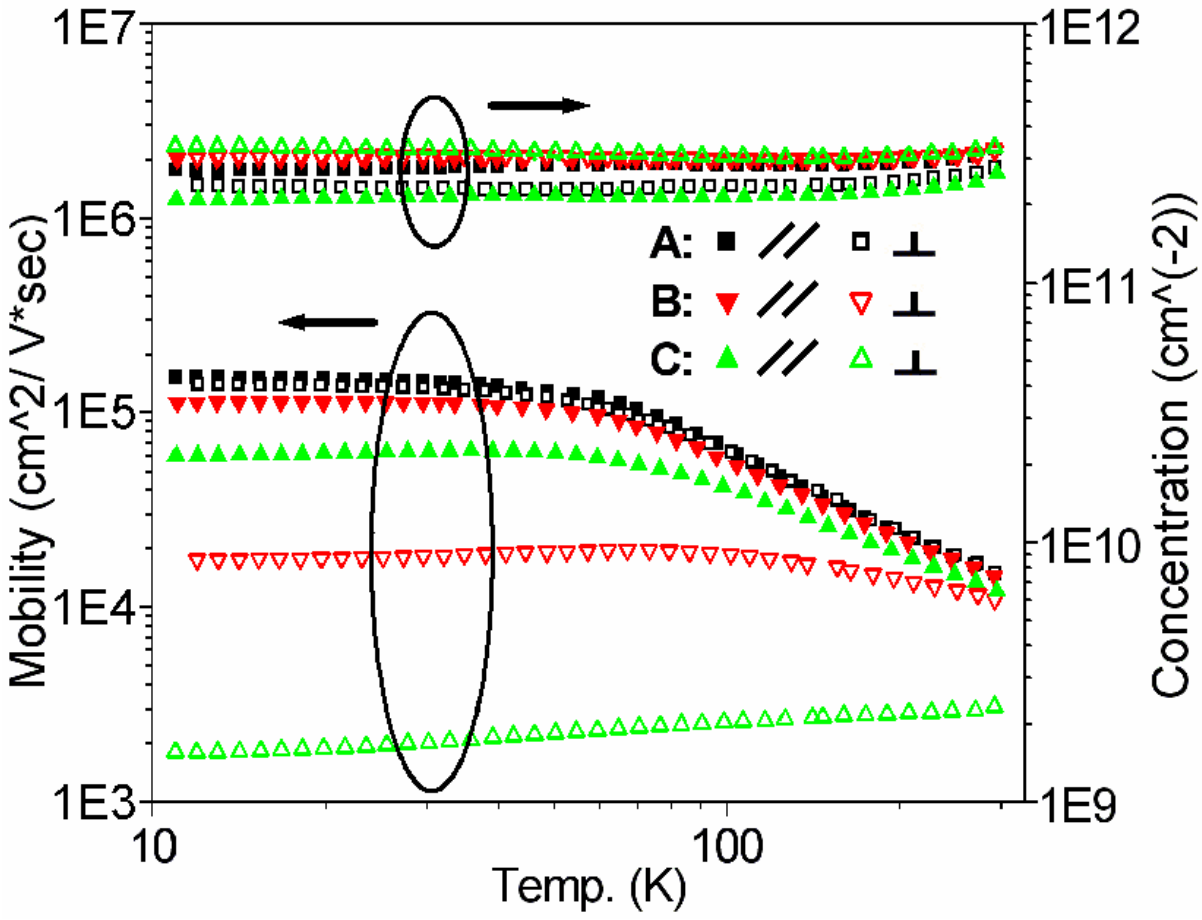

Fig.6.3: The electron mobility and sheet carrier density as functions of temperature for Sample A, Sample B, and Sample C, parallel and perpendicular to the InAs QWrs

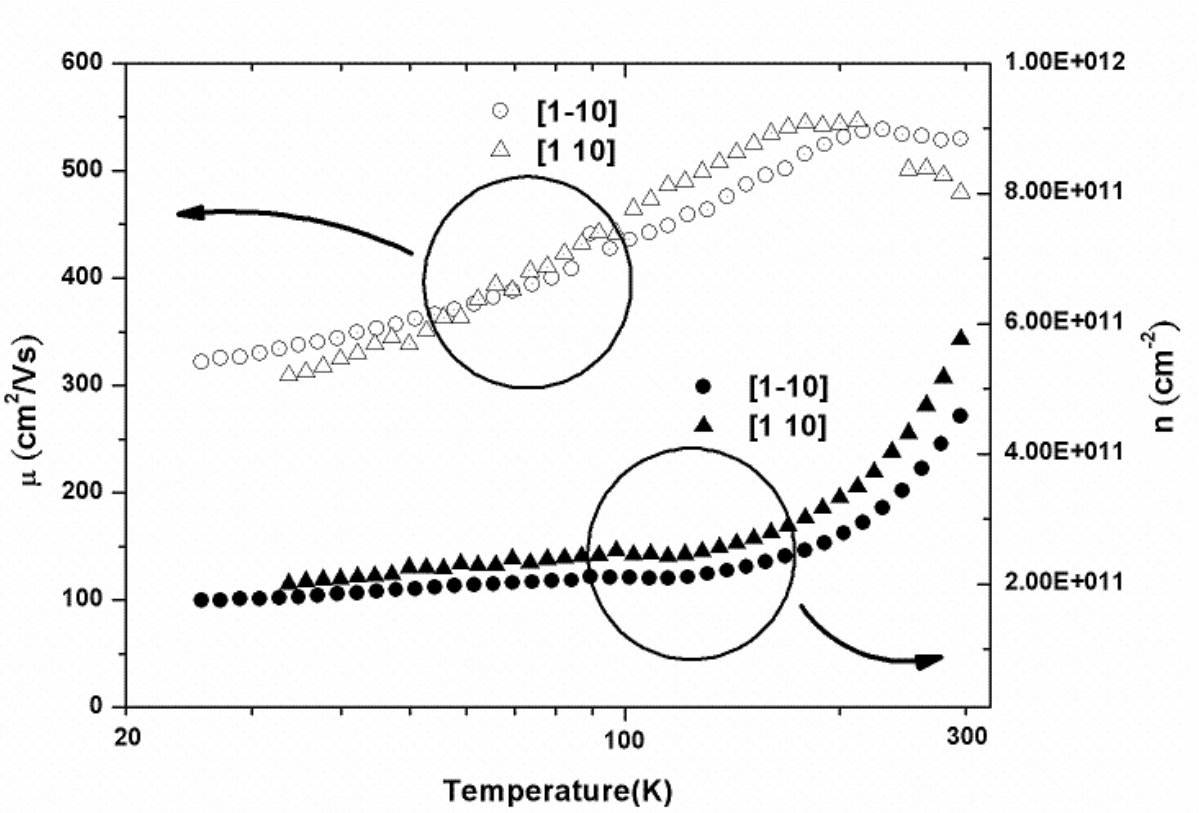

Fig.6.4: The electron mobility and sheet carrier density as functions of temperature for Sample D, with 2.6 InAs QDs, in [110] and [$1\bar{1}0$] directions.

Unlike InAs QDs in GaAs substrates, the electron energy in the InAs QWrs with the elongated structures is quasi continuous above the ground quantized state. Furthermore, because of the smaller barrier in the InAs/InGaAs system on InP substrates (as compared with the conventional InAs/GaAs system on GaAs substrates), the electrons in the wires are weakly confined. The electrons are likely to move around easily and couple together with the 2-D electrons in the InGaAs/InAlAs interface channel. As a result, the InAs QWrs behave more like scattering centers instead of conduction channels.

For Sample D, as shown in Fig.6.4, there is small sheet concentration difference between [110] and [$1\bar{1}0$] directions. This difference could be attributed to the measurement

error and the non-uniformity epitaxy on the wafer. Because the distance between each InAs QDs is about tens nanometer, this QD layer cannot act as a conduction layer. Only the 2-D channel is the conduction channel of Sample D.

With deceasing the temperature under 100K, the sheet concentration is reduced to about two fifth of the value at room temperature. This large reduction should be attributed to the QDs placed 10nm below the 2-D channel, which caused these InAs QDs to trap certain number of the conduction electrons in the 2-D channel at low temperature. Fig.6.5 shows the AFM image of Sample D and presents that the QDs density is about 6E10 cm^{-2}. Some studies reported that each QD could capture about ten electrons[95]. Therefore, a magnitude of the order of ten to the eleventh of electrons is captured by the QDs near the 2D channel at low temperature. Unlike InAs QWrs in InGaAs matrix cases as shown in Fig.6.3, their sheet concentration only reduces about ten percent at low temperature. These different characteristics between InAs QDs in GaAs matrix and InAs QWrs in InGaAs matrix is also the evidence that electrons are weakly confined in InAs QWrs on InGaAs matrix, as discussed in the previous paragraph.

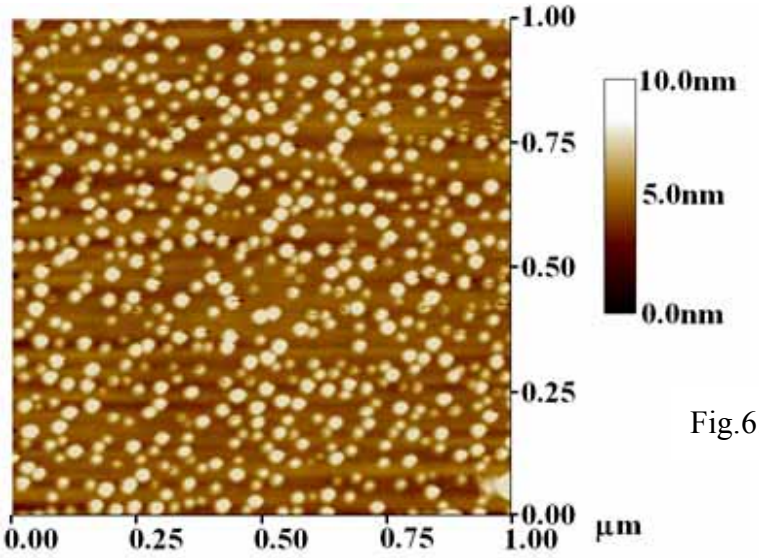

Fig.6.5: The AFM image of Sample D.

6.4 Electron Hall Mobility

Fig.6.3 also shows the electron Hall mobility versus temperature curves for Sample A, Sample B, and Sample C. Each sample has two results from two Hall bar orientations: one is parallel to the InAs QWrs (i.e. $[1\bar{1}0]$ direction) and another is perpendicular to the InAs QWrs (i.e. $[110]$ direction). The electron Hall mobility vs. temperature curves of Sample D in $[110]$ and $[1\bar{1}0]$ directions are also shown in Fig.6.4.

For Sample A, without InAs QWrs, we do not see any orientation dependence for electron mobility. The electron mobility with InAs QDs in GaAs matrix also does not have obvious difference in $[110]$ and $[1\bar{1}0]$ directions. Because of the presence of InAs QDs just 10nm below the 2D channel, those QDs played as scattering centers in the 2D channel. As a result, the Hall mobility in Sample D is less than $600cm^2/VSec$. The almost same electron mobility in two directions means that the scattering cross section of InAs QDs in GaAs are the same in $[110]$ and $[1\bar{1}0]$ directions. This is reasonable because the InAs QDs in GaAs have square pyramid shape[96], of which the scattering cross-section is the same in $[110]$ and $[1\bar{1}0]$ directions.

However, for Sample B and Sample C, the electron Hall mobility shows the strong orientation dependence. The electron mobility is much higher when the transport direction is parallel to the InAs QWrs. The remarkable difference between $[110]$ and $[1\bar{1}0]$ direction is clearly attributed to the presence of the wires. Therefore, the anisotropy in mobility with the presence of InAs QWrs is caused by the difference in scattering cross section of the InAs QWrs with different orientations. Because of the shape of the InAs QWrs, when the electrons move parallel to the InAs QWrs, the scattering cross section is much smaller than that when the electrons move perpendicular to the InAs QWrs. The mobility ratio, $\mu_{//}/\mu_{\perp}$, for sample B at

low temperature is around 6.5 while that for sample C is 33.5. The larger ratio for Sample C is because the InAs QWrs are right at the heterointerface, which is very close to the conduction channel.

Fig.6.6 showed the mobility ratio, $\mu_{//}/\mu_{\perp}$, for Sample B and Sample C as a function of temperature. As the temperature increases, the anisotropy in mobility becomes less. It occurs because the role of scattering centers played by InAs QWrs becomes less important as temperature increased and the orientation independent phonon scattering takes over as the dominant scattering mechanism.

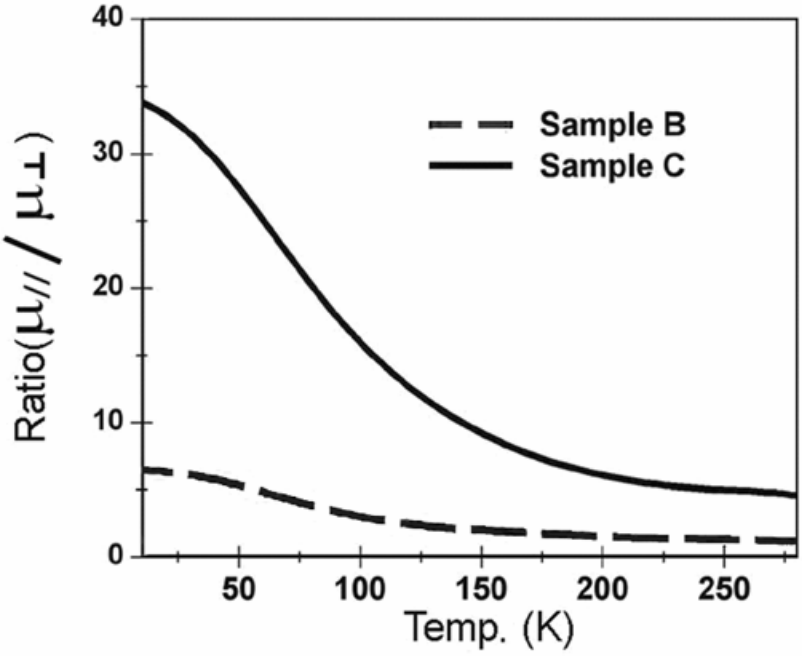

Fig.6.6: The electron mobility ratio as a function of temperature for Sample B and Sample C.

6.5 Summary

In conclusion, we are able to create an anisotropic conduction medium using InAs QWrs.

Self-assembled InAs QWrs in InGaAs/InAlAs heterostructures causes mobility asymmetry for the electron conduction in the 2-D channel. At low temperatures, electron mobility parallel to the InAs QWrs is much higher than that perpendicular to the InAs QWrs. The asymmetry in mobility is attributed to the difference in scattering cross section of the InAs QWrs in these two directions. The square pyramid shape of InAs QDs, however, leads to the same scattering cross section in $[110]$ and $[1\,\bar{1}\,0]$ directions.

In the presence of the InAs QWrs, the mobility of the 2-D channel parallel to the wires can be made nearly as high as the channel without the InAs QWrs. However, at the same time, an order of magnitude lower in mobility exists for conduction perpendicular to the InAs QWrs. This possibility of creating an artificial asymmetric conduction medium should find interesting applications in electronic devices.

Chapter 7

Conclusion and Future Work

7.1 Conclusion of Present Work

Some interesting results about the MBE parameter influence on quantum structure growth, stacking behaviors, optical characteristics, electron transport behaviors, and the laser applications of the wire-like quantum structures on the materials, lattice matched to normally (100) orientated InP substrates were systematically investigated. We first studied the MBE parameter influence on the morphology of wire growth. Then, the stacked wire behaviors were explored by the TEM technique. Based on obtaining well-enough InAs QWrs, their polarization dependence optical behaviors and laser application were explored. Finally, we analyzed the InAs QWr influence on the electron transport behaviors.

With the investigation of InAs quantum structure growth, the dependence of the InAs monolayer number, the substrate temperature, the As_2 BEP, the interruption time between each monolayer deposition, and the In growth rate on InAs quantum structure morphology were studied. The influence of these MBE parameters on InAs wire formation is discussed. The InAs quantum structures have anisotropic shape and are elongated along $[1\bar{1}0]$ direction. The different In adatom diffusion coefficient along $[110]$ and $[1\bar{1}0]$ should be the dominant factor for InAs wire formation. We find the suitable and stable growth conditions to obtain the straight and long InAs QWrs. The length of InAs QWrs is about $1\,\mu m$ under this growth condition while sometime, the length can be longer than $1\,\mu m$.

GaAs quantum structure morphology is also elongated along $[1\bar{1}0]$ direction. In our systematical experiments, the morphology is sensitive to the substrate temperature, the GaAs monolayer number, the interruption time between each monolayer deposition, and the As_2 BEP. A proper growth condition to obtain straight GaAs anti-QWrs is found. From the comparison between the investigation of InAs QWrs and GaAs anti-QWrs, the interruption between each monolayer improves the InAs wire formation, but obstruct the GaAs wire formation. An explanation, based on the anisotropic stress effect, was proposed for the GaAs wire formation.

From the cross-sectional TEM pictures, the stacking behaviors of InAs QWrs and GaAs anti-QWrs in InGaAs matrix lattice to (100) InP substrates are both vertically aligned to form a rectangular lattice. However, the stacking behavior of InAs QWrs in InAlAs matrix lattice to (100) InP substrate is staggered to form a b.c.c. like lattice. Clear composition modulation phenomena are found in the post-grown matrices on the nano wires in all of these three cases. For InAs QWrs and GaAs anti-QWrs in InGaAs matrix cases, the composition modulation is due to the non-uniform strain distribution. As a result, the composition modulation is developed vertically in these two cases. However, the composition modulation for InAs QWrs in InAlAs matrix is needed to consider another factor: the In atom preference of migrating to the valley in the InAlAs matrix to minimize the surface free energy. Adding considering the characteristic of In atom, the composition modulation is developed obliquely for InAs QWrs in InAlAs matrix. Based on the composition modulation distribution, we explain the stacking behaviors of InAs QWrs in InGaAs matrix, GaAs anti-QWrs in InGaAs matrix, and InAs QWrs in InAlAs matrix.

The four monolayers InAs layer was successfully used as the active region material for the laser diode application. The PPL results of these samples show that InAs QWrs have obvious polarization dependence. The lasing wavelength is about 1.6~1.8 μm. Two sets of

laser diodes with different cavity orientations, perpendicular to QWrs and parallel to QWrs, were both fabricated. The apparent polarization dependence behaviors are observed from the comparison of the lasing spectra and L-I curves of these laser diodes between each cavity orientation. Laser diodes with cavity orientation parallel to QWrs have higher threshold currents and are the excited state lasing even at 20K. Laser diodes with cavity orientation perpendicular to QWrs have lower threshold currents. Moreover, the lasing spectra show that there is a transition of the ground state lasing to the excited state lasing at about 140K for the laser cavity perpendicular to QWrs. L-I results of the lasers with the same cavity orientation also show this transition phenomenon. Furthermore, under proper condition, the laser diodes with cavity oriented perpendicular to the QWrs show the simultaneous two-state lasing behavior during 140~160K. The L-I curves and lasing spectra for the lasers cavity oriented parallel and perpendicular to the InAs QWrs agree with polarization preference of the optical transitions in 1-D quantum structures.

Self-assembled InAs QWrs embedded in the InGaAs/InAlAs heterostructure was studied. Because of the anisotropic morphology of InAs QWrs, which are elongated along $[1\bar{1}0]$ direction, the scattering cross section of QWrs is different in $[1\bar{1}0]$ and $[1\bar{1}0]$ direction. This makes the electron conduction mobility in the 2-D conduction channel be asymmetry. As a result, an anisotropic conduction medium is obtained. The mobility magnitude ratio in two directions can be above 30 in our experiment.

In summary, we experimentally studied the wire-like quantum structures on materials lattice matched to normally (100) orientated InP substrates. Some unique wire growth behaviors were observed and explained. With the proper MBE growth parameters, well-enough InAs and GaAs nano wires can be obtained. Moreover, these behaviors and explanations can help us to obtain better nano wires afterward. The interesting stacked wire behaviors were observed and discussed. The optical and electrical behaviors agree with the

anisotropic preference in 1-D quantum structures. For the device application, we successfully demonstrated InAs QWr laser diodes. The lasing behaviors show the 1-D quantum structure characteristics. Furthermore, the interesting simultaneous two-state lasing was observed.

7.2 Future Work

Length of InAs QWrs in this work can be reproducibly made up to 0.75~1μm. Although we have figured out the suitable parameter sets to fabricate InAs QWrs on the (100) InP substrates, some parameters still need to be investigated extensively. For an example, the substrate temperature between 450~500℃ and the extreme low As_2 BEP below 1E-6 torr, are not investigated. In addition, the migration enhanced epitaxy technique[97], i.e. alternative group III source and group V source deposition, can increase the surface migration of group III atoms during epitaxy. The migration enhanced epitaxy technique can be investigated for InAs QWr formation. Then, the stable condition to obtain InAs QWrs with length much longer than 1 μm may be found. How to control the wire density and the wire cross-section size are also fascinating.

Although GaAs anti-QWrs had been systematically investigated in this work, the stable condition to obtain well enough anti-QWrs with length above 1 μm is still not found. As the stable growth is found, the GaAs anti-QWrs can be used a template for some interesting investigations. For example, several monolayer InAs grown on this template with or without spacer may give us extreme long InAs QWrs. Furthermore, vertical QWs may be obtained by utilizing this template and the short period superlattice technique[98].

InAs QWr laser with lasing wavelength about 1.6~1.8μm have be demonstrated in our

experiment. Semiconductor laser diodes with lasing wavelength above 2μm can provide more applications for medical care, gas spectroscopy, and chemical inspection. Currently, our MBE system includes the capability to use Sb source. InAs QWrs doped with Sb is a feasible way to investigate for obtaining the emitting wavelength above 2μm[99].

Because InAs QWrs have two dimension confinements, the normal incident light on the wafer can be absorbed by the QWrs. Furthermore, because of higher coverage of InAs QWrs on InP substrates than GaAs QDs on GaAs substrates, the InAs QWrs on InP substrates is also a material candidate for the infrared photodetector application with compared to the InAs QDs on GaAs substrates. Our laboratory has many experiences of device fabrication and measurement on quantum well and quantum dot infrared photodetectors. Therefore, utilization of InAs QWrs for infrared photodetectors could be a practical research.

Finally, because the large size distribution of self-assembled InAs QWrs gives wide gain spectrum, InAs QWrs in proper InGaAlAs matrix will have gain spectrum around 1.55μm. This spectrum range is for optical communication. As the results, InAs QWrs could be a good material candidate for optical amplifiers for optical network.

We have successful obtained the InGaAs/InAlAs heterostructures on InP substrates with the InAs QWrs embedded near the conduction channel. This structure is similar to the high electron mobility transistor(HEMT) structure. Because self-assembled quantum structures avoid additional defects by the lithography and the etching processes and InAs material has high electron mobility, the InAs QWrs embedded in the InGaAs/InAlAs heterostructure is an interesting topic for the HEMT applications. Because the smooth and straight InAs QWrs with length about 1μm can be obtained in our laboratory, the behaviors of the HEMT with InAs QWrs embedded in the conduction channel and with the gate length shorter than 1μm will be fascinating.

Reference

[1] H. Sakaki, *Jpn. J. Appl. Phys*., **19**, L735 (1980)

[2] Y. Arkawa and H. Sakaki, *Appl. Phys. Lett.*, **40,** 939 (1982)

[3] Mitsuru Sugawara, *Self-Assembled InGaAs/GaAs Quantum Dots,* Academic Press, San Diego, (1999).

[4] Y. Arakawa, H. Sakai, *Appl. Phys.Lett*. **40** 939 (1982)

[5] D. Bimberg, M. Grundmann, N. N. Ledentsov, M. H. Mao, Ch. Ribbat, R. Sellin, V. M. Ustinov, A. E. Zhukov, Zh.I. Alferov, J.A. Lott, *Phys. Stat. Sol. (B)* **224** 787 (2001)

[6] P.G. Eliseev, H. Li, G.T. Liu, A. Stintz, T.C. Newwell, L.F. Lester, K.J. Malloy, *IEEE J. Sel. Top. Quant. Electron.* **7**, 135 (2001)

[7] E. H. C. Parker, *The Technology and Physics of Molecular Beam Epitaxy*, Springer, London, (1985)

[8] Jeffrey Y. Tsao, *Materials Fundamentals of Molecular Beam Epitaxy,* Academic Press, San Diego, (1993)

[9] H. M. Manasevit, *Appl. Phys. Lett*., **12**, 156 (1968)

[10] H. M. Manasevit, *J. Crystal Growth*, **13/14**, 306 (1972)

[11] W. T. Tsang, *Appl. Phys. Lett*. **51**, 917 (1980).

[12] C. J. Nuese and J. I. Pankove, *Light emitting diodes-LEDs* , Springer, Berlin, (1980)

[13] L. C. West and S. J. Eglash, *Appl. Phys. Lett*. **46,** 1156 (1985)

[14] C. P. Lee, D.L. Miller, D. Hou, and R. J. Anderson, *paper IIA-7, at 1983 Device Research Conference*, June 20-22, University of Vermont

[15] B. E. Maile, A. Forchel, R. Germann, J. Straka, L. Korte, and C. Thanner, *Appl. Phys. Lett*. **57,** 807 (1990)

[16] L. Birotheau, A. Izrael, J. Y. Marzin, R. Azoulay, V. Thierry-Mieg, and F. R. Ladan, *Appl. Phys. Lett*. **61,** 3023 (1992)

[17] E. Kapon, D. M. Hwang, and R. Bhat, *Phys. Rev. Lett*. **63**, 430 (1989)

[18] N. H. Karam, A. Mastrovito, V. Haven, K. Ismail, S. Pennycook, and Henry I. Smth, *J, Crystal Growth*, **107**, 591 (1991)

[19] S. Koshiba, H. Noge, H. Akiyama, T. Inoshita, Nakamura, A. Shimizu, Y. Nagamune, M. Tsuchiya, H. Kano, H. Sakaki, and K, Wada, *Appl. Phys. Lett.* **64**, 363 (1994)

[20] S. Koshiba, I. Tanaka, Y. Nakamura, and H. Sakaki, *Appl. Phys. Lett.* **70**, 883 (1997)

[21] M. Tsuchiya, J. M. Gaines, R. H. Yan, R. J. Simes, P. O. Holtz, L. A. Coldren, and P. M. Petroff, *Phys. Rev. Lett.*, **62**, 466 (1989)

[22] M. Tanaka and H. Sakaki, *Appl. Rev. Lett.,* **54**, 1326 (1989)

[23] A. C. Chen, A. M. Moy, P. J. Pearah, K. C. Hsieh, and K. Y. Cheng, Appl.Phys. Lett. **62**, 1359 _1993_.

[24] S. T. Chou, K. Y. Cheng, L. J. Chou, and K. C. Hsieh, Appl. Phys. Lett.**66**, 2220 _1995_.

[25] M. Takeuchi, K. Shiba, K. Sato, H. K. Huang, K. Inoue, and H. Nakashima, *Jpn. J. Appl. Phys., Part 1,* **34**, 4411 (1995)

[26] Y. Nakamura, S. Koshiba, and H. Sakaki, *J. Cryst. Growth*, **175/176**, 1092 (1997)

[27] Y. C. Chang, L. L. Chang, and L. Esaki, *Appl. Phys. Lett.*, **47**, 1324 (1985)

[28] L. Pfeiffer, K. W. West, H. L. Stormer, J. P. Eisentein, K. W. Baldwin, D. Gershoni, and J. Spector, *Appl. Phys. Lett.*, **56**, 1697 (1990)

[29] R. Nötzel, N. N. Ledentsov, L. Däweritz, K. Ploog, and M. Hohenstein, *Phys. Rev. B*, **45**, 3507 (1992)

[30] M. Higashiwaki, M. Yamamoto, T. Higuchi, S. Shimomura, A. Adachi, Y. Okamoto, N. Sano, and S. Hiyamizu, *Jpn. J. Appl. Phys., Part 2*, **35**, L606 (1996)

[31] Zhongzhe Sun, Soon Fatt Yoon, Ju Wu, and Zhanguo Wang, *J. Appl. Phys*., **91** 6021 (2002)

[32] H. R. Gutie´rrez, M. A. Cotta, and M. M. G. de Carvalho, *Appl. Phys. Lett*. **79**, 3854 (2001)

[33] Hanxuan Li, Theda Daniels-Race, and Mohamed-Ali Hasan, *Appl. Phys. Lett*. **80**, 1367 (2002)

[34] Donald L. Smith, *Thin-film Deposition Principles & Practice*, McGraw-Hill Inc. New York

[35] Mukai. K., Ohtsuka. N., Sugawara. M., and Yamazaki. S., *Jpn, J. Appl. Phys*, **33**, L1710 (1994)

[36] S.D. Lin, C.P. Lee, W.H. Hsieh, and Y.W. Suen, *Appl. Phys. Lett.,* **81**, 3007 (2002).

[37] Q. Xie, A. Madhukar, P. Chen, and N.P. Kobayashi, *Pyhs. Rev. Lett*, **75** 2542 (1995)

[38] G.S. Solomon, J.A. Trezza, A.F. Marshall, and J.S. Harris, *Phys. Rev. Lett*., **76** 952 (1996)

[39] M. Strassburg, V. Kutzer, U. W. Pohl, A. Hoffmann, I. Broser, N. N. Ledentsov, D. Bimberg, A. Rosenauer, U. Fischer, D. Gerthsen, I. L. Krestnikov, M. V. Maximov, P. S. Kop'ev, and Zh.I. Alferov, *Appl. Phys. Le*tt., **72**, 942 (1998)

[40] G. Springholz, M. Pinczolits, P. Mayer, V. Holy, G. Bauer, H. H. Kang, and L. Salamanca-Riba, *Phys. Rev. Lett.,* **84**, 4669 (2000).

[41] N. Kirstaedter, N. N. Ledentsov, M. Grundmann, D. Bimberg, V. M. Ustinov, S. S. Ruvimov, M. V. Maximov, P. S. Kopev, Z.I. Alferov, *Appl Phys Lett,* **69**,1226 (1994)

[42] J. Phillips, Pallab Bhattacharya, S.W. Kennerly, D.W. Beekman, and Dutta, *IEEE J. Quantum Electronics*, **35** 936 (1999)

[43] S.Y. Wang, S.D. Lin, H.W. Wu, and C.P. Lee, *Appl Phys. Lett.,* **78**, 1023, (2001)

[44] Fibers and Their Applications: *Conf. Lasers and Materials in Industry and Opto-Contact*

Workshop, (SPIE-Int. Soc.) Vol **3416** (Quebec, Canada) p 2

[45] R.H. Wang, A. Stintz, P.M. Varangis, T.C. Newell, H. Li, K.J. Malloy, and L.F. Lester, *IEEE Photonics Tech. Lett.*, **13**, 767 (2001)

[46] R. Schwertberger, D. Gold, J.P. Reithmaier, and A. Forchel, *IEEE Photonics Technology Lett.*, **14**, 735 (2002)

[47] D. Gold, R. Schwertberger, J.P. Reithmaier, and A. Forchel, *LEOS 2002. 2002 IEEE/LEOS Annual Meeting Conference Proceedings*, Part vol.1, pp.25 (2002)

[48] A. Bilenca, R. Alizon, V. Mikhelashvili, G. Eisenstein, R. Schwertberger, D. Gold, J.P. Reithmaier, and A. Forchel, *Electronics Lett.*, **38**, 1350 (2002)

[49] E. Finkman, S. Maimon, V. Immer, G. Bahir, S. E. Schacham, F. Fossard, F. H. Julien, J. Brault, and M. Gendry, *Phys. Rev. B*, **63**, 045323 (2001)

[50] P. L. Souza, A. J. Lopes, T. Gebhard, K. Unterrainer, M. P. Pires, J. M. Villas-Boas, G. S. Vieira, P. S. S. Guimarães, Nelson Studart, *Appl Phys. Lett.,* **90** 173510 (2007)

[51] A.J. Shields, M.P. O'Sullivan, I. Farrer, D.A. Ritchie, K. Cooper, C.L. Foden, and M. Pepper, *Appl Phys. Lett.*,.**74**, 735 (1999)

[52] Wang. Qin, N. Carlsson, P. Omling, L. Samuelson, W. Seifert, and H.Q. Xu, *Appl Phys. Lett.*,.**76**, 1704 (2000)

[53] T. Kawazu , T. Noda, H. Sakaki, *PhysicaE*, **21**, 536(2004)

[54] H. Sakaki, *Jpn. J. Appl. Phys.* **19**(12), L735 (1980)

[55] O. E. Raichev1, and P. Vasilopoulos, *Phys. Rev. Lett*. **83**(18), 3697 (1999)

[56] V. A. Sablikov and B. S. Shchamkhalova, *Phys. Rev. B,* **58,** 13847 (1998)

[57] C. Walther, W. Hoerstel, H. Niehus, J. Erxmeyer, W.T. Masselink, *J. Cryst. Growth,* **209**, 572-580 (2000)

[58] K. Kern, D. Heitmann, P. Grambow, Y. H. Zhang, and K. Ploog, *Phys. Rev. Lett*, **66**, 1618 (1991)

[59] K. Bollweg, T. Kurth, D. Heitmann, V. Gudmundsson, E. Vasiliadou, P. Grambow, and K. Eberl, *Phys. Rev. Lett.* **76**, 2774 (1996)

[60] G. M. Gusev, P. Basmaji, Z. D. Kvon, L. V. Litvin, Yu. V. Nastaushev, and A. I. Toropov, *Solid State Commun.* **85**, 317 (1993).

[61] D. Huang, G. Gumbs, and N. J. M. Horing, *Phys. Rev. B* **49**, 11463 (1994).

[62] E. H. C. Parker, *The Technology and Physics of Molecular Beam Epitaxy*, Springer, London, (1985)

[63] Donald L. Smith, *Thin-film Deposition Principles & Practice*, McGraw-Hill Inc., New York (1999)

[64] M. A. Herman and H. Sitter, *Molecular Beam Epitaxy Fundamentals and Current Status*, Springer-Verlag, Berlin Heidelberg (1996)

[65] B.A. Joyce, P.J. Dobson, J.H. Neave, K. Woodbridge, J. Zhang, P.K. Larsen, B. Boelger, *Surf. Sci.*, **168**, 413, (1986)

[66] Neil W. Ashcroft and N. David Mermin, *Solid State Physics*, Saunders college, New York (1976)

[67] *D1 system Install, Operation and Maintenance Manual*, Bede Scientific Inc.

[68] S. N. Magonov and M. H. Whangbo, *Surface analysis with STM and AFM*, (1996)

[69] Sidney Perkowitz, *Optical Characterization of Semiconductors: Infrared, Raman, and Photoluminescence Spectroscopy*, Academic Press, New York (1993)

[70] D. E. Wohlert and K. Y. Cheng, *Appl. Phys. Lett.*, **76**, 2247 (2000)

[71] D. B. Williams and C. B. Carter, *Transmission Electron Microscopic*, Plenum Press, New York (1996)

[72] K.T. Moore, E.A. Stach, J.M. Howe, D.C. Elbert, and D.R. Veblen, *Micron*, **33**, 39 (2002).

[73] W.R. Runyan, and T.J. Shaffner, *Semiconductor Measurements and Instrumentation*, McGraw-Hill, New York (1998)

[74] J. Phillips, K. Kamath, and P. Bhattacharya, *Appl. Phys. Lett*. **72**, 2020, (1998)

[75] D. Pan, E. Towe, and S. Kennerly, *Appl. Phys. Lett*. **73**, 1937 (1998)

[76] J. Brault, M. Gendry, G. Grenet, G. Hollinger, Y. Desieres, and T, Benyattou, *Appl. Phys. Lett.*, **73**, 2932 (1998).

[77] A. Stintz, T.J. Rotter, and K.J. Malloy, *J. Cryst. Growth*, **255**, 266 (2003)

[78] M. A. Cotta, R. A. Hamm, T.W. Staley, S.N. Chu, L. R. Harriott, M. B. Panish, and H. Tempkin, *Phys. Rev. Lett*. **70**, 4106 (1993).

[79] Y. Horikoshi, H. Yamaguchi, F. Briones, and M. Kawashima, *J. Cryst. Growth* **105**, 326 (1990).

[80] J.M. Garcia, L. Gonzalez, M.U. Gonzalez, J.P. Silveira, Y. Gonzalez, and F. Briones, *J. Cryst. Growth*, **227-228**, 975, (2001)

[81] Hanxuan Li, Ju Wu, Zhanguo Wang, and Theda Daniels-Race, *Appl. Phys. Lett.*, **75**, 1173 (1999).

[82] K.T. Moore, E.A. Stach, J.M. Howe, D.C. Elbert, and D.R. Veblen, *Micron*, **33**, 39 (2002).

[83] M. Kasu and N. Kobayashi, *Appl. Phys. Lett.*, **62**, 1262 (1993).

[84] G. Grenet and C. Priester, *Phys. Rev. B*, **61**, 16029 (2000).

[85] Mitsuo Fukada, *Optical Semiconductor Device*, John Wiley & Sons, Inc., New York (1999)

[86] P. C. Sercel and K. J. Vahala, *Phys Rev. B*, **44**, 5681, (1991)

[87] D. S. Citrin and Y. C. Chang, *Phys Rev. B*, **43**, 11703, (1991)

[88] K. B. Wong, M. Jaros, and J. P. Hagon, *Phys Rev. B*, **35**, 2463, (1987)

[89] T. Ogawa and Y. Kanemitsu, *Optical properties of Low-Dimensional Materials*, World Scientific, Singapore (1995)

[90] H. Ando, S. Nojima, and H. Kanbe, *J. Appl. Phys.*, **74**, 6383 (1993)

[91] M. Notomi, S. Nojima, M. Okamoto, H. Iwamura, T. Tamamura, J. Hammersberg, and H. Weman, *Phys Rev. B*, **52**, 11073, (1995)

[92] S. L. Chuang, *Physics of Optoelectronic Devices*, John Wiley & Sons, Inc., New York (1995)

[93] M.P. Mikhailova, *Handbook Series on Semiconductor Parameters*, **vol.1**, World Scientific, London, 1996

[94] Goldberg Yu.A. and N.M. Schmidt, *Handbook Series on Semiconductor Parameters*, **vol.2**, World Scientific, London, 1999

[95] H. C. Liu, B. Aslan, M. Korkusinski, S.-J. Cheng, P, Hawrylak, *Infrared Phys. & Tech.*, **44**, 503 (2003)

[96] S. Ruvimov and K. Scheerschmidt, Phys. Status Solidi A **150**, 471 (1995)

[97] Y. Horikoshi, M. Kawashima, and H. Yamaguchi, *Appl. Phys. Lett.*, **50**, 1686 (1987).

[98] K. Y. Cheng, K. C. Hsieh, and J. N. Baillargeon, *Appl. Phys. Lett.*, **60**, 2892 (1992).

[99] F. Dore, C. Cornet, P. Caroff, A. Ballestar, J. Even, N. Bertru, O. Dehaese, I.Alghoraibi, H.Folliot, R. Piron, A. Le Corre, S. Loualiche, *Physica Status Solidi C*, **11**, 3902, (2006)